Production of Antihydrogen via Double Charge Exchange

Dissertation zur Erlangung des Grades
Doktor der Naturwissenschaften
am Fachbereich 08: Physik, Mathematik und Informatik
der Johannes Gutenberg-Universität Mainz

von
Andreas Müllers
geboren in Simmern, Hunsrück

Mainz, Oktober 2012

1st assesor:

2nd assesor:

Date of defense: February 1st, 2013

This work was supported by a PhD scholarship from the Carl Zeiss Foundation.

Abstract

Spectroscopy of the $1S-2S$ transition of antihydrogen confined in a neutral atom trap and comparison with the equivalent spectral line in hydrogen will provide an accurate test of CPT symmetry and the first one in a mixed baryon-lepton system. Also, with neutral antihydrogen atoms, the gravitational interaction between matter and antimatter can be tested unperturbed by the much stronger Coulomb forces. Antihydrogen is regularly produced at CERN's Antiproton Decelerator by three-body-recombination (TBR) of one antiproton and two positrons. The method requires injecting antiprotons into a cloud of positrons, which raises the average temperature of the antihydrogen atoms produced way above the typical 0.5 K trap depths of neutral atom traps. Therefore only very few antihydrogen atoms can be confined at a time. Precision measurements, like laser spectroscopy, will greatly benefit from larger numbers of simultaneously trapped antihydrogen atoms. Therefore, the ATRAP collaboration developed a different production method that has the potential to create much larger numbers of cold, trappable antihydrogen atoms. Positrons and antiprotons are stored and cooled in a Penning trap in close proximity. Laser excited cesium atoms collide with the positrons, forming Rydberg positronium, a bound state of an electron and a positron. The positronium atoms are no longer confined by the electric potentials of the Penning trap and some drift into the neighboring cloud of antiprotons where, in a second charge exchange collision, they form antihydrogen. The antiprotons remain at rest during the entire process, so much larger numbers of trappable antihydrogen atoms can be produced. Laser excitation is necessary to increase the efficiency of the process since the cross sections for charge-exchange collisions scale with the fourth power of the principal quantum number n. This method, named double charge-exchange, was demonstrated by

ATRAP in 2004. Since then, ATRAP constructed a new combined Penning Ioffe trap and a new laser system. The goal of this thesis was to implement the double charge-exchange method in this new apparatus and increase the number of antihydrogen atoms produced. Compared to our previous experiment, we could raise the numbers of positronium and antihydrogen atoms produced by two orders of magnitude. Most of this gain is due to the larger positron and antiproton plasmas available by now, but we could also achieve significant improvements in the efficiencies of the individual steps. We therefore showed that the double charge-exchange can produce comparable numbers of antihydrogen as the TBR method, but the fraction of cold, trappable atoms is expected to be much higher. Therefore this work is an important step towards precision measurements with trapped antihydrogen atoms.

Zusammenfassung

Spektroskopie des $1S-2S$ Übergangs von gespeichertem Antiwasserstoff würde durch Vergleich mit der äquivalenten Linie in Wasserstoff einen präzisen Test der CPT Symmetrie ermöglichen. Dies wäre der erste CPT Test in einem gemischten Baryon-Lepton System. Des weiteren ließe sich mit elektrisch neutralen Antiwasserstoffatomen die Wirkung der Schwerkraft zwischen Materie und Antimaterie untersuchen ohne dass die Messung von der viel stärkeren Coulomb Wechselwirkung gestört wird. Antiwasserstoff wird an CERNs Antiproton Decelerator bereits regelmäßig über Drei-Körper-Rekombination (three-body-recombination, TBR) produziert. Für diesen Prozess werden Antiprotonen über eine Hochfrequenzanregung in eine Wolke aus Positronen getrieben. Dies heizt die Antiprotonen auf so dass die mittlere Temperatur der produzierten Antiwasserstoffatome weit über der typischen Fallentiefe von $0,5\,\mathrm{K}$ einer Neutralatomfalle liegt. Daher können zur Zeit nur wenige Antiwasserstoffatome auf einmal gespeichert werden. Präzisionsmessungen wie Laserspektroskopie würden aber von einer größeren Anzahl an gespeicherten Antiwasserstoffatomen profitieren. Zu diesem Zweck hat die ATRAP Kollaboration eine andere Produktionsmethode entwickelt, den zweifachen Ladungstransfer. Cäsiumatome werden mittels Laserlicht auf Rydbergzustände angeregt und kollidieren mit Positronen. Dabei entsteht Rydberg-Positronium, ein gebundenes System aus einem Elektron und einem Positron. Die Positroniumatome driften wiederum in eine benachbarte Wolke aus Antiprotonen und erzeugen in einer zweiten Ladungstransferreaktion Antiwasserstoff. Die Antiprotonen verbleiben während des ganzen Prozesses in Ruhe, daher ist ein sehr viel höherer Anteil an kalten Antiwasserstoffatomen zu erwarten als bei der Drei-Körper-Rekombination. Die Laseranregung der Cäsiumatome ist nötig da der Wirkungsquerschnitt für die Ladungstrans-

ferreaktionen mit der vierten Potenz der Hauptquantenzahl n ansteigt: $\sigma \propto n^4$. Der zweifache Ladungstransfer wurde 2004 von ATRAP zum ersten Mal getestet. Seitdem wurde eine neue kombinierte Penning-Ioffe-Falle und ein neues Lasersystem konstruiert. Im Rahmen dieser Arbeit wurde der zweifache Ladungstransfer in dieser neuen Falle implementiert. Im Vergleich zu unserem vorherigem Experiment von 2004 konnten wir die Produktion von Positronium und Antiwasserstoff um zwei Größenordnungen steigern. Dies begründet sich hauptsächlich in den größeren Positronen- und Antiprotonenplasmen die uns mittlerweile zur Verfügung stehen, wir konnten aber auch die Effizienz der einzelnen Schritte wesentlich verbessern. Über den zweifachen Ladungstransfer lassen sich also vergleichbare Mengen an Antiwasserstoff herstellen wie mit der etablierten Methode der Drei-Körper-Rekombination, allerdings ist der erwartete Anteil an kalten Antiwasserstoffatomen weitaus höher. Diese Arbeit ist daher ein wichtiger Schritt hin zu Präzisionsmessungen mit gefangenem Antiwasserstoff.

Contents

Chapter 1

Introduction

In 1928, Paul Dirac published the first relativistic theory of the hydrogen atom including the electron spin [40]. However, his equation seemed to suffer from one flaw: It had solutions with positive energy, corresponding to electrons, as well as states with negative energy. To explain these apparently unphysical states, Dirac introduced a hole theory. He suggested that the vacuum is a many-body quantum state with all of the negative energy eigenstates already occupied. If an electron is removed from a negative energy state, the remaining hole would act like a particle with positive charge, much like the hole left by an excited electron in the valence band of a semiconductor. At first, he suggested that the hole-particle could possibly be the proton [42]. Only after this idea had to be rejected [41, 109], Dirac came to the conclusion that the negative energy states must indeed correspond to a new particle, so far unobserved [43].

In fact, traces of these new particles had been observed before [101], but their explicit discovery in 1932 was the achievement of Carl Anderson. At Caltech, Anderson was studying cosmic rays with a cloud chamber. He had placed his chamber

in a strong magnetic field to bend the trajectories of β particles and thus measure their momentum. However, some of his photographs showed traces that curved in the wrong direction. Anderson first attributed these to electrons that did not come from above, but moved from the earth upwards. This view was rejected by his supervisor Robert Millikan who believed they were caused by cosmic protons, despite the fact that the traces' lengths and densities did not match heavy particles.

To resolve their argument, Anderson placed a lead plate inside his cloud chamber. Particles crossing the lead lose energy, so after emerging from the plate, their trajectory is curved at a smaller radius than before. Thus the particle's course through the chamber is known and, together with the direction of the magnetic field, the sign of its charge can be determined.

Surprisingly, the photographs showed traces caused by particles which had positive charge, like the proton, but were much lighter (figure 1.1). Anderson had found a new particle, which he called the positive electron, or positron (e^+) [8,9].

1.1 Antimatter and Symmetry

The discovery of positrons showed that there is a second, previously unknown, type of matter in the universe. The antiproton ($\bar{p}$) and antineutron ($\bar{n}$) were found twenty years later by experiments at the Bevatron accelerator [25, 34]. It soon became clear that every particle has its antimatter twin and when the first quark models were developed to explain the substructure of protons, neutrons and other baryons that had been found in the meantime, antimatter was included right from the beginning [72].

In many ways, antimatter appears to be a mirror image of the particles our world is built of. The first experiments showed complete agreement in the fundamental

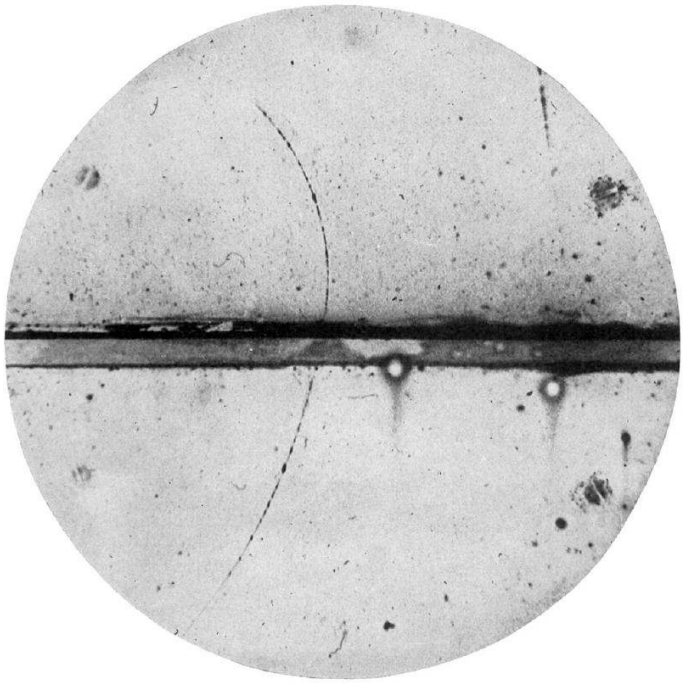

Figure 1.1: Cloud chamber image of the first positron observed by Carl Anderson on August 2, 1932. After crossing the lead plate in the center, the trajectory is curved at a smaller radius. Therefore the particle must have passed the chamber from bottom to top. The magnetic field points into the paper plane, so the particle's charge is positive. A heavy particle like a proton would have caused a thicker and much shorter trace. Picture taken from [9].

properties of particles and their corresponding antiparticles. Therefore it seemed obvious to assume that the universe and the fundamental forces are also completely symmetric in matter and antimatter. In the same way that our galaxy is made of matter, we could construct a mirror galaxy consisting purely of antimatter by replacing each particle with its corresponding antiparticle. This transformation is called charge conjugation (C). It is a discrete symmetry, like time reversal (T) and parity (P). The latter corresponds to a point reflection where each coordinate is inverted: $x_i \mapsto -x_i$.

The picture of a perfect mirror image is very elegant, but it turned out to be not entirely true. In 1956, Tsung-Dao Lee and Chen Ning Yang pointed out that, in contrast to the strong and electromagnetic forces, no experiment performed to date had provided any evidence to either support or refute conservation of parity by the weak interaction [94]. They suggested several measurements, two of which were carried out by Chien-Shiung Wu [137] and Garwin et al. [70] in the following months. Both found proof that the weak interaction does indeed violate parity, or, equally, charge conjugation.

This revealed the first distortion in the mirror image and the next followed shortly after. While the individual symmetries parity and charge conjugation were violated, the combined operation CP was believed to be conserved. However, it took less than ten years for CP violation to be demonstrated experimentally in the decay of K mesons [30]. Now only the combined operation of the three symmetries CPT appears to be a conserved quantity. In combination with CP violation, this implies that time reversal T is also violated.

So we know that the mirror image is slightly distorted, that there are asymmetries between matter and antimatter. While a perfect mirror universe is a fascinating idea, slight asymmetries may be even more interesting. They stir the questions of why the mirror is distorting the way it does? Is there a deeper underlying symmetry that we have not discovered yet? In the last 80 years, our knowledge on antimatter has grown tremendously, but there are fundamental questions we cannot answer yet: Why does our universe seem to consist entirely of matter? Where is all the missing antimatter? The distortions we have found in the mirror so far, C- and CP violation, are too small to explain this asymmetry. Also, we do not know how gravity, one of nature's four fundamental forces, acts on antimatter.

Many researchers around the world are looking for answers to these questions.

The efforts of the low-energy physics community are centered at CERN's Antiproton Decelerator (AD), currently the only place in the world that provides low energy antiprotons ($\bar{p}$) which can be trapped and studied for macroscopic timescales. A new machine named FLAIR (Facility for Low-Energy Antiproton and Ion Research) is planned as part of a major upgrade at the Helmholtz Center for Heavy Ion Research (GSI, Germany). The AD hall houses several experiments which mainly focus on the study of antihydrogen ($\bar{H}$) atoms, the simplest stable atomic system consisting of antimatter.

1.1.1 CPT tests with Antihydrogen

In general, the CPT theorem states that any Lorentz invariant local quantum field theory must conserve the combined operation CPT [97]. This includes the Standard Model (SM). The SM is the most comprehensive picture we have of physics today, containing also violation of C and CP symmetry. However, it is not complete. For one, it does not include gravity. Also, it does not provide explanations to some very fundamental questions, for instance the asymmetry in the occurrence of matter and antimatter.

Answers may be found in physics beyond the Standard Model, possibly by a violation of CPT symmetry. It should be noted that CPT violation requires that Lorentz symmetry is also not conserved, but not vice versa [77]. A theoretical framework to describe violations of Lorentz- and CPT symmetry was developed by Kostelecky and collaborators [16, 32]. The idea is to add all possible CPT- and Lorentz breaking couplings to the SM Lagrangian with scaling parameters, the size of which may be determined by experiment. Thus the name Standard Model Extension (SME). The SME can make no prediction on the size of the coefficients

and in which regime CPT violations are most likely to occur. Therefore a wide search is necessary covering as many areas as possible.

CPT symmetry requires the fundamental properties of particles and antiparticles to either be identical, like mass, or of opposite sign, like charge. Measuring and comparing these properties with high sensitivity is therefore a straightforward test of CPT invariance. This has been done for electrons and positrons e^-/e^+, protons and antiprotons $p/\bar{p}$ and for meson systems like pions $\pi^\pm$ and Kaons $K^0/\bar{K}^0$. An overview over some measurements is shown in figure 1.2. So far, the most precise test in the lepton sector is a comparison of the magnetic moments of the electron and the positron [131]. For baryons, it is the charge-to-mass ratio of protons and antiprotons [63]. In the meson sector, the comparison of the neutral Kaon and Anti-Kaon masses provides the highest fractional precision of $5 \cdot 10^{-18}$ [22]. This system is also important since, in contrast to leptons and baryons, it already violates CP symmetry.

Measurements on atomic systems will open up a new field for CPT tests using mixed baryon and lepton systems including their interactions. Antihydrogen is an ideal candidate [17]. It is the simplest stable atomic system and the properties of hydrogen have been measured with extremely high precision. The $1S - 2S$ transition frequency is now known with a fractional accuracy of $4.2 \cdot 10^{-15}$ [111]. These measurements were done using a cold atomic beam, a technique that is not very attractive for antihydrogen. Due to the low production rate of $\bar{H}$ atoms, spectroscopy in a neutral atom trap is more suitable. This has also been demonstrated for hydrogen [24], however at lower accuracy. A similar measurement could be done with about 1000 trapped antihydrogen atoms [79].

Additionally, a measurement of the $1S - 2S$ transition would also be a direct comparison of the Rydberg constants for H and $\bar{H}$ which are sensitive to the charges

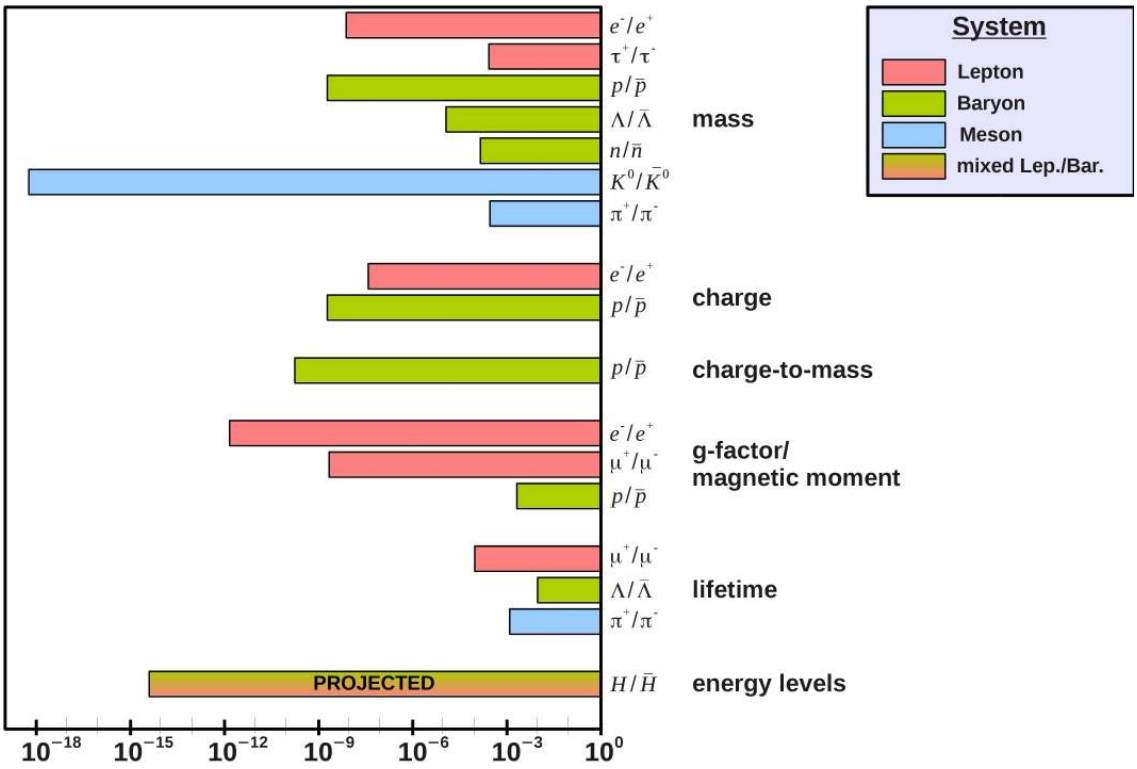

Figure 1.2: Fractional precision of CPT tests performed so far, including a projected value for comparison of the $1S-2S$ transition in hydrogen and antihydrogen using the accuracy achieved to date [111]. Values are taken from the 2012 tables of the Particle Data Group (PDG) [2].

and masses of the leptons and baryons:

$$\frac{R_{\infty(\bar{H})}}{R_{\infty(H)}} = \left(\frac{m_{e^+}}{m_{e^-}}\right)\left(\frac{1+m_{e^+}/m_{\bar{p}}}{1+m_{e^-}/m_p}\right)\left(\frac{q_{e^+}}{q_{e^-}}\right)^2\left(\frac{q_{\bar{p}}}{q_p}\right)^2. \tag{1.1}$$

The ratio of the masses of electron and positron is currently known to $2\cdot10^{-9}$, so a measurement of the $1S-2S$ transition frequency of antihydrogen with higher precision could also improve CPT tests in the lepton and baryon sector.

The (anti)hydrogen atom offers more than one possibility to test fundamen-

tal symmetries. Apart from the $1S-2S$ optical transition, measuring the ground state hyperfine splitting will also provide a CPT test of comparable accuracy [135]. Additionally, a neutral atomic system allows measurements of the gravitational interaction between matter and antimatter undisturbed by the much stronger electromagnetic force [27, 48].

1.2 Overview of this Thesis

This work was prepared as part of the ATRAP collaboration, an international group with members from Harvard University (US), York University Toronto (CA), the Research Center Jülich (GER) and the Johannes Gutenberg University and Helmholtz Institut Mainz (GER). The experiment is located at CERN's Antiproton Decelerator (AD). ATRAP's goals are precision measurements of the $1S-2S$ optical transition and the ground state hyperfine splitting of antihydrogen. Comparison with hydrogen will provide a CPT test with high accuracy and the first one to be conducted on a mixed baryon lepton system. To this aim, antihydrogen atoms are produced [66] and confined [62] in a neutral atom Ioffe trap. Laser cooling of the trapped $\bar{H}$ atoms will significantly increase the measurement's precision [89].

Production of cold antihydrogen was first achieved ten years ago [4, 59] and by now thousands of anti-atoms are regularly made during single experiments. However, confining $\bar{H}$ atoms only succeeded recently [10, 62] and only very few atoms are caught at a time. The averages range from $0.7-5$ atoms per trial, much less than the 1000 $\bar{H}$ atoms suggested for precision spectroscopy [79]. The reason for this rather low trapping rate is that the established production method, the three-body recombination (TBR), relies on driving antiprotons into a cloud of positrons. This adds significant amounts of energy to the $\bar{p}$ so that the antihydrogen atoms

produced are mostly too energetic to be confined in a neutral atom trap.

This thesis investigates a different production method which does not suffer from this drawback, the double charge-exchange: Cesium atoms are laser excited to high-n Rydberg states and interact with positrons in a charge-exchange reaction. This forms positronium, a bound state of an electron and a positron. The positronium atoms then interact with antiprotons and produce antihydrogen. The antiprotons remain at rest during the entire process, which therefore may produce much larger numbers of cold antihydrogen atoms. Laser excitation is essential since the cross sections for charge-exchange collisions scale as $\sigma \propto n^4$, n being the principal quantum number. In 2004, ATRAP showed the feasibility of this method by producing a few antihydrogen atoms [126]. Since then, a new apparatus was constructed. It is a combined Penning-Ioffe trap capable of holding larger plasmas of antiprotons and positrons and with the possibility to trap the antihydrogen atoms produced.

The goal of this work was to implement the double charge-exchange in this new, more complex, apparatus and show that this method is also capable of producing much larger numbers of $\bar{H}$ atoms than previously demonstrated.

This chapter has already introduced the connection between antimatter and fundamental symmetries. Next, the production methods for $\bar{H}$ atoms are reviewed in chapter 2, with a focus on the double charge-exchange.

The Penning-Ioffe trap and the components to produce a stream of cesium atoms within the apparatus are described in chapter 3. This chapter also contains the other components of the ATRAP experiment, including the sources for antimatter particles and the detector system.

The laser system for excitation of cesium atoms to Rydberg states constructed for this work is described separately in chapter 4. It was initially designed during the author's master thesis (German Diplom) [105]. It could be significantly improved

in [18] and during the course of this work [106].

After installation and commissioning of the new components at CERN, our first task was the laser excitation of cesium atoms in the high magnetic fields of our Penning-Ioffe trap. These fields strongly modify the cesium energy levels and so far, no complete analytical solution exists. Therefore we had to find approximate solutions to estimate the energy levels. We used two different methods and compared the results with experimental data obtained during this work. This is the topic of chapter 5.

With Rydberg cesium atoms available in the trap, we investigated the charge-exchange process. The experiments performed for this thesis are described in chapter 6. Positronium atoms were already found in our first trials and we could demonstrate a factor of 500 more Ps^* than previously reported [122]. The verification of $\bar{H}$ production proved more difficult. After a series of unsuccessful trials, we found that the detection method used does not work under our experimental conditions. However, with a newly developed detection scheme we could demonstrate the production of 2000 antihydrogen atoms per trial, an increase by two orders of magnitude compared to the previous experiment in 2004 [126]. This increase is mainly due to the larger particle numbers available by now, but we could also significantly improve the efficiencies of most of the steps involved. Our results and implications for further experiments are discussed in chapter 7.

Appendix A contains details on the laser control- and data acquisition software developed during the course of this work. Sample code for the calculation of Rydberg energy levels in strong magnetic fields using the two methods discussed in chapter 5 is found in appendix B.

Chapter 2

Production Methods for Antihydrogen

The first production of antihydrogen was reported in 1996 from the *PS210* experiment at CERN's Low Energy Antiproton Ring (LEAR) [13]. Antiprotons circling through the ring collided with xenon atoms. These collisions may result in the production of an electron positron pair and a subsequent formation of antihydrogen. The cross section for the in-flight production of antihydrogen scales with the collision energy, so the antiprotons were circulating at 1.2 GeV, close to the maximum of LEAR. Even at these high energies, the production rate is very low. 11 ± 2 $\bar{H}$ atoms were produced by this first experiment. Later, a larger sample of 57 $\bar{H}$ atoms was reported from Fermilab [15].

Precision measurements with antihydrogen require either a cold atomic beam, like it is used for laser spectroscopy of hydrogen [111], or $\bar{H}$ atoms confined in a neutral atom trap. The second approach is better suited to the small numbers of antihydrogen atoms available. It provides macroscopic interaction times and can

thus result in very sensitive measurements. During a collision with a xenon atom, only a small fraction of the initial $\bar{p}$ energy is lost, so the antihydrogen atoms created this way move essentially with the same speed as the antiprotons. Therefore these $\bar{H}$ atoms are much too fast to confine them in a neutral atom trap or shape them into a cold beam. So while the first production of $\bar{H}$ was a very important milestone, the production method used is not suitable to supply $\bar{H}$ atoms for precision measurements.

Cooling of high energy electrically neutral particles is extremely difficult, if possible at all. To obtain cold antihydrogen atoms, it is therefore favorable to produce them from initially cold antiprotons and positrons. This first requires trapping and cooling antiprotons and positrons. The first results were also obtained at LEAR by the TRAP collaboration who confined antiprotons in a Penning trap [60]. They showed that $\bar{p}$ can be stored for macroscopic timescales. TRAP also suggested the nested well potential structure shown in figure 2.1 for simultaneous confinement of antiprotons and positrons in the same Penning trap [68]. This setup is now used for most antihydrogen experiments.

Trapping and storing antiprotons and positrons is just the first step. Several formation methods exist to produce antihydrogen atoms. They are discussed in the remainder of this chapter, more detailed reviews are found in [29, 84]. A suitable method should provide a large production rate to efficiently use the small numbers of antimatter particles available. For precision experiments, the $\bar{H}$ atoms must be produced at very low temperatures. To catch $\bar{H}$ atoms in a neutral atom Ioffe-Pritchard trap [14], their temperatures must be below the typical trap depths of $0.5\,\mathrm{K} \equiv 40\,\mu\mathrm{eV}$.

In all cases, the combination of an antiproton and a positron to a bound state of antihydrogen requires a third particle that carries away excess energy and momen-

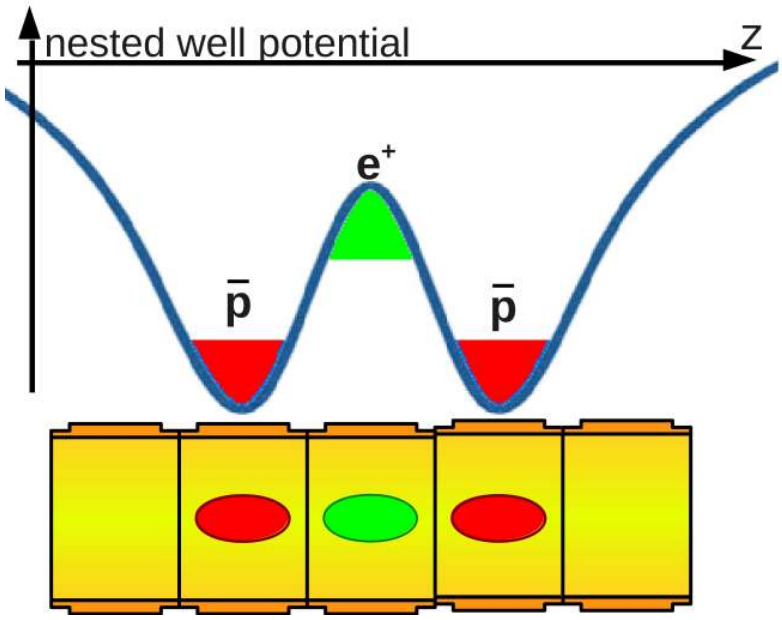

Figure 2.1: Nested well potential for simultaneous confinement of antiprotons and positrons in a Penning trap.

tum. In the simplest case of radiative recombination, the third particle is a photon. This method suffers from a very low cross section and is therefore only briefly introduced in section 2.1. During $\bar{H}$ formation by three-body recombination (TBR), the required third particle is another positron. The process is described in section 2.2. Up to date, most $\bar{H}$ atoms were produced by this method, but so far only very few could be trapped. The process under investigation in this thesis, the double charge-exchange, is described in section 2.3. It has so far only been demonstrated once [126]. While it is more complicated than the TBR method, it has the potential to produce much larger numbers of cold, trappable antihydrogen atoms.

2.1 Spontaneous Radiative Recombination

The simplest process for $\bar{H}$ formation is a direct recombination of an antiproton and a positron. The excess energy is carried away by a photon:

$$\bar{p} + e^+ \Rightarrow \bar{H} + h\nu\,. \tag{2.1}$$

For typical experimental conditions, the collision time is much shorter than the time required to radiate a photon, so the overall production rate per antiproton per second is very low. It is given by [29]:

$$\Gamma_{SRR} = 3 \cdot 10^{-11} \sqrt{\frac{4.2}{T}}\, n_{e^+}\,, \tag{2.2}$$

where T is the positron temperature and n_{e^+} is the positron density in cm^{-3}. Filling in typical values for the ATRAP experiment, $T = 4.2\,\mathrm{K}$, $n_{e^+} = 4 \cdot 10^8\,\mathrm{cm}^{-3}$, leads to a numerical value of $\Gamma_{SRR} = 1.2 \cdot 10^{-2}\,\mathrm{s}^{-1}$. With 1 Million antiprotons we expect a rate of $N_{\bar{p}} \cdot \Gamma_{SRR} = 1.2 \cdot 10^4$ antihydrogen atoms produced per second.

Radiative recombination has the distinct advantage of producing antihydrogen atoms predominantly in the ground state. The two other methods described in this chapter produce $\bar{H}$ atoms in excited Rydberg states. To confine these atoms, they must decay to a trappable ground state before annihilating on the walls of the trap. However, the production rate from radiative recombination is very low compared to the other two methods. Theoretically, the rate could be enhanced by interaction with a laser that stimulates recombination, but so far no experimental evidence for this process was found [6].

2.2 Three-Body Recombination

Within a dense positron plasma, the excess energy and momentum can also be carried away by a second positron:

$$\bar{p} + e^+ + e^+ \Rightarrow \bar{H} + e^+ \,. \tag{2.3}$$

The process is called three-body recombination (TBR). Its matter equivalent is known from plasma physics. Using it for $\bar{H}$ formation was first suggested by Gabrielse et al. [68]. The formation rate is calculated in [125]:

$$\Gamma_{TBR} = 6 \cdot 10^{-12} \left(\frac{4.2}{T} \right)^{9/2} n_{e^+}^2 \,. \tag{2.4}$$

Using the same numerical values as above, this leads to $\Gamma_{TBR} = 9.6 \cdot 10^5\,\mathrm{s}^{-1}$ and an expected production rate of $N_{\bar{p}} \cdot \Gamma_{TBR} = 9.6 \cdot 10^{11}$ antihydrogen atoms per second. In a magnetic field, this production rate is decreased by a factor of 10 [76]. Still, this rate is seven orders of magnitude higher than Γ_{SRR}, so under typical experimental conditions, antihydrogen atoms will most likely form by three-body recombination.

The positron is predominantly captured in very high n states [110] and then cascades to the ground state via several processes like de-excitation collisions with other positrons and replacement collisions. In the latter, a second positron crosses the antihydrogen atom and becomes bound at a lower n state while the initial e^+ is freed again. For high n states, these processes have a much shorter time constant than emission of dipole radiation. So de-excitation by spontaneous emission of photons only has a negligible contribution.

The first antihydrogen atoms produced at low energies were reported in 2002 by the ATHENA [4] and ATRAP collaborations [59]. Positrons from a ^{22}Na source and antiprotons provided by CERN's Antiproton Decelerator were loaded in a nested

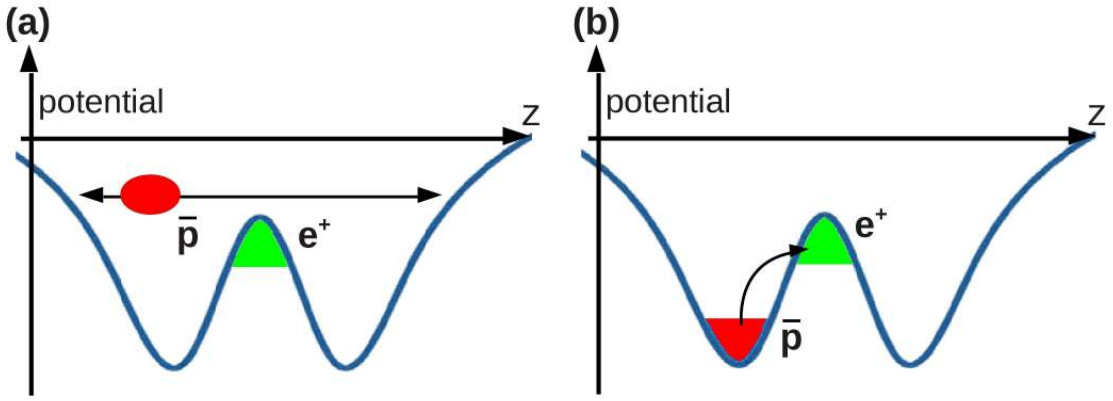

Figure 2.2: Production of antihydrogen in a Penning trap: (a) Energetic $\bar{p}$ oscillate through the e^+ forming hot antihydrogen. (b) If the $\bar{p}$ are cold, they must be driven into the e^+ plasma.

well Penning trap and antihydrogen was formed while energetic $\bar{p}$ oscillated through the e^+. The process is shown in figure 2.2(a). The formation rates and positron temperatures suggest that these $\bar{H}$ atoms were formed by three-body recombination, although a later study showed that the temperature scaling of the formation rate was not consistent with the $\propto T^{-9/2}$ behavior expected from equation (2.4) [5]. The observed temperature dependence fits closer to the radiative recombination process, but the measured production rate is much higher than expected for radiative recombination. The answer is most likely a combination of both processes and some possibly unconsidered factors like the magnetic field or the finite transit time of the antiprotons through the positron plasma [5]. The $\bar{p}$ were launched into the potential structure with several eV of energy, which corresponds to a temperature of more than 10 000 K. Therefore these experiments created antihydrogen atoms that were far too hot to be trapped. In later studies, the antiprotons were instead cooled to a few K into one of the side-wells of the potential structure and then driven into the positron cloud, figure 2.2(b). This technique allowed trapping of single antihydrogen

atoms for the first time by the ALPHA collaboration [10] and then in slightly larger numbers by ATRAP [62].

Trying to produce trappable antihydrogen atoms by three-body recombination suffers from an intrinsic drawback: While they are still hot, the antiprotons oscillate through the large outer well in figure 2.2(a). They can easily interact with the positrons, but the resulting antihydrogen atoms are too energetic to be trapped. On the other hand, the antiprotons can be adiabatically cooled to temperatures as low as 3.5 K [64], but then they are restricted to the bottom of one of the side wells and separated from the positrons by the potential barrier. Overcoming this barrier requires the addition of energy and thus heating the particles up again. Although a lot of progress has been made on driving techniques [11], the fundamental problem and the low trapping rates remain.

2.3 Charge-Exchange

The difficulty of overcoming the potential barrier can be circumvented by sending the positrons into the antiprotons in an electrically neutral bound state. Positronium (Ps), a system of an electron and a positron, is an ideal candidate. While bound to an electron, the positrons can enter the antiproton trapping region unaffected by the electrostatic potential of the Penning trap. Once inside the $\bar{p}$ cloud, collisions with the antiprotons occur, some of which result in a charge-exchange reaction where the positron is captured by the antiproton, producing antihydrogen and a free electron. The reaction can be written as:

$$\bar{p} + Ps \Rightarrow \bar{H} + e^{-} . \tag{2.5}$$

The main advantage is that during the entire process, the antiprotons remain

at rest so that $\bar{p}$ cooling methods [64] can be used to their full potential. Since the kinetic energy, or temperature, of the antihydrogen atoms created mainly depends on the initial energy of the antiprotons, this production method offers the possibility to generate large numbers of cold, trappable antihydrogen atoms. Making $\bar{H}$ via a charge-exchange reaction from positronium was first proposed by Deutch [39]. The charge conjugate reaction, the production of hydrogen from proton impact on positronium, was demonstrated by Merrison et al. [102]. They found cross sections on the order of $10^{-16}\,\mathrm{cm}^2$, which is 100 times higher than for spontaneous radiative recombination, but still much lower than for the three-body process. Additionally, positronium, even in the long-living triplet state, has a lifetime of only $\tau_{Ps} = 142\,\mathrm{ns}$. Both problems can be solved by using highly excited states of positronium [28]. The cross section for charge-exchange collisions scales with the geometric size of the atom, $\sigma_{CE} \propto r^2 \propto n^4$, n being the principal quantum number. The larger spatial separation of the e^- and the e^+ in highly excited states also causes much longer lifetimes [26].

Laser excitation of ground state positronium is possible but poses some technical challenges due to the short Ps lifetime. Also, the low mass of the Ps atoms causes large Doppler broadenings. Even at temperatures of 4 K, transitions from the ground state have linewidths broadened to several tens of GHz. Instead, it is favorable to first laser excite cesium atoms (Cs) and then use two consecutive charge-exchange reactions to make antihydrogen, as suggested by Hessels [82].

$$Cs + h\nu \Rightarrow Cs^* \tag{2.6a}$$

$$Cs^* + e^+ \Rightarrow Ps^* + Cs^+ \tag{2.6b}$$

$$Ps^* + \bar{p} \Rightarrow \bar{H}^* + e^- \tag{2.6c}$$

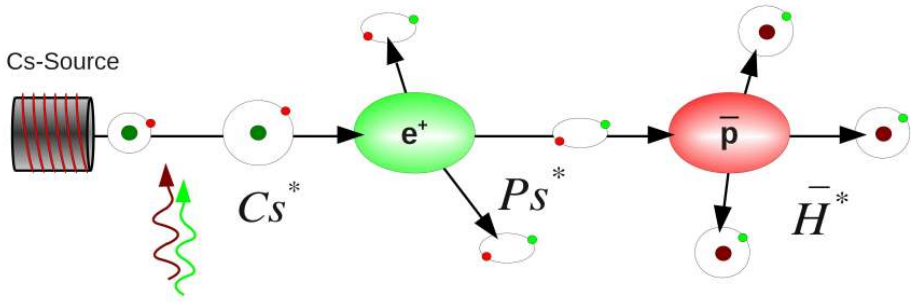

Figure 2.3: Antihydrogen production by two stage Rydberg charge-exchange: Cesium atoms are laser excited to high n states and interact with positrons, forming Rydberg positronium (Ps^*). Some of these positronium atoms then drift into a neighboring cloud of antiprotons where, in a second charge-exchange collision, they form antihydrogen ($\bar{H}^*$).

The process is illustrated in figure 2.3. Cesium or other alkali metals are suitable because of their single electron in the outer shell which allows efficient laser excitation. Also, they are easily available from commercial sources.

The cross sections for double charge-exchange production of antihydrogen were determined by classical trajectory Monte Carlo simulations in [82]. They scale with n^4 and for a cesium state of $n = 40$, they are as high as $10^{-9}\,\mathrm{cm}^2$, seven orders of magnitude larger than in the ground state. The binding energy of the cesium atom is transfered during the charge-exchange collisions, so positronium is created in Rydberg states with long lifetimes and losses from self-annihilation are negligible. The $\bar{H}$ atoms are also created in a high-n state well defined by the initial laser excitation of the cesium atoms. In contrast, three-body recombination populates a wide range of n states which are way above the levels considered for charge-exchange experiments. The deeper bound antihydrogen atoms created by Rydberg charge-exchange therefore have a higher chance of surviving stray electric fields and will

decay to a trappable ground state on a faster timescale. Both factors also help towards the trapping of larger $\bar{H}$ numbers.

Charge-exchange collisions feature large cross sections if the relative speed of the particles v is smaller than the classical orbital speed of the light particle in the bound system v_o, for instance the Rydberg electron in the cesium atom. The electron in the $n = 40$ state of cesium has a classical velocity of $v_o = \alpha c/n \simeq 55000\,\mathrm{m/s}$. Cesium atoms emitted from heated alkali metal dispensers have velocities on the order of 250 m/s while positrons with a thermal distribution of 4.2 K move with a speed of 11000 m/s. The criterion $v/v_o < 1$ is therefore fulfilled as long as the e^+ temperature remains below 100 K.

Excited states feature long lifetimes, especially for high values of the orbital angular momentum quantum number l. The $40D$ state of cesium has a lifetime of 40 μs [55]. Strong magnetic fields, as are required for the experiments described here, mix m and l states (see chapter 5), which further increases the lifetime of the resulting state. An $n = 40$ level that consists of an equal mixture of all l and m states has a lifetime of more than 1 ms [26], so the atom can travel for almost 1 m before decaying. Therefore laser excitation can happen at some distance away from the region where Cs^* atoms interact with the positrons. This reduces the experimental complexity compared to direct laser excitation of Ps atoms.

Laser excitation of positronium is planned as a variation of the charge-exchange production scheme suggested by the AE$\bar{g}$IS collaboration. The aim of this group is to study the gravitational acceleration of antihydrogen atoms [46]. While they also want to make antihydrogen by Rydberg charge-exchange, the Ps is produced in a different way. In recent years, it was found that certain porous materials can act as efficient positronium converters and their properties have been studied extensively [75]. If positrons are implanted into a porous target, they can acquire an electron

from the material and form positronium. Large pores open to the surface allow these *Ps* atoms to emerge from the material before annihilating. Some converters show high efficiencies of more than 40 % [99], but they produce the positronium atoms in their ground state. The *Ps* must then be laser excited before it decays [31]. The overall efficiency will depend on several factors like the temperature of the target material within a cryogenic apparatus and how well the *Ps* thermalize. If they are too cold, they will be too slow to emerge from the target before annihilating [46]. These are mostly technical issues, but small variations may have a drastic effect on the efficiency. In principle, this process promises to be an interesting alternative to obtain Rydberg positronium, but since the experiment is just being set up at CERN, there is no data yet that would allow a direct comparison of the two methods.

In 2004, ATRAP demonstrated the double charge-exchange production of $\bar{H}$ as suggested by Hessels [82]. Cesium atoms were laser excited and positronium [122] and antihydrogen [126] was produced by two consecutive charge-exchange reactions. Cesium and a two stage laser excitation scheme was chosen due to an available laser system. The first excitation step from the ground state of cesium $6S_{1/2}$ to $6P_{3/2}$ requires laser-light with a wavelength of 852 nm. This was provided by a diode laser. The transition energy from this intermediate level to the closely spaced Rydberg states corresponds to a wavelength of 511 nm. For this step, a commercial copper vapor laser was used. The experiments were performed with $1.4{\cdot}10^6\, e^+$ and $2.4{\cdot}10^5\, \bar{p}$ each and resulted in an average of about 17 antihydrogen atoms produced per trial.

Since this first demonstration, ATRAP has developed a new apparatus capable of loading and manipulating much larger particle clouds. Also, a new laser system for excitation of cesium atoms to Rydberg states was constructed. The new components are described next. Chapter 3 contains an overview of ATRAP's Penning-Ioffe trap while the laser system is described in chapter 4.

Chapter 3

The ATRAP Experiment

This chapter describes the components of the ATRAP apparatus and CERN's Antiproton Decelerator (AD) where the experiment is located. The AD, treated in section 3.1.1, is a unique decelerator ring providing low energy antiprotons. Right now, it is the only facility in the world where $\bar{p}$ are slowed down enough to be trapped and confined for macroscopic time scales. Figure 3.1 shows a cross section of the ATRAP experimental zone in the AD hall. Bunches of $\bar{p}$ emitted from the AD are guided to the ATRAP zone through a beam line. Bending magnets direct the antiprotons into a combined Penning-Ioffe trap (section 3.3) from underneath. The ATRAP positron system, treated in section 3.1.2, accumulates e^+ from a ^{22}Na source. The e^+ bunches are sent through a 6 m long transfer line and enter the trap from the top. The positrons are transfered with 63 eV of energy and are thus easily stopped by a potential barrier within the trap.

In contrast, the energy of the $\bar{p}$ bunches delivered from the AD is 5.3 MeV, which is too high to stop them with a DC voltage barrier. Therefore the antiprotons are sent through a gas filled energy tuning cell and a thin beryllium foil at the bottom

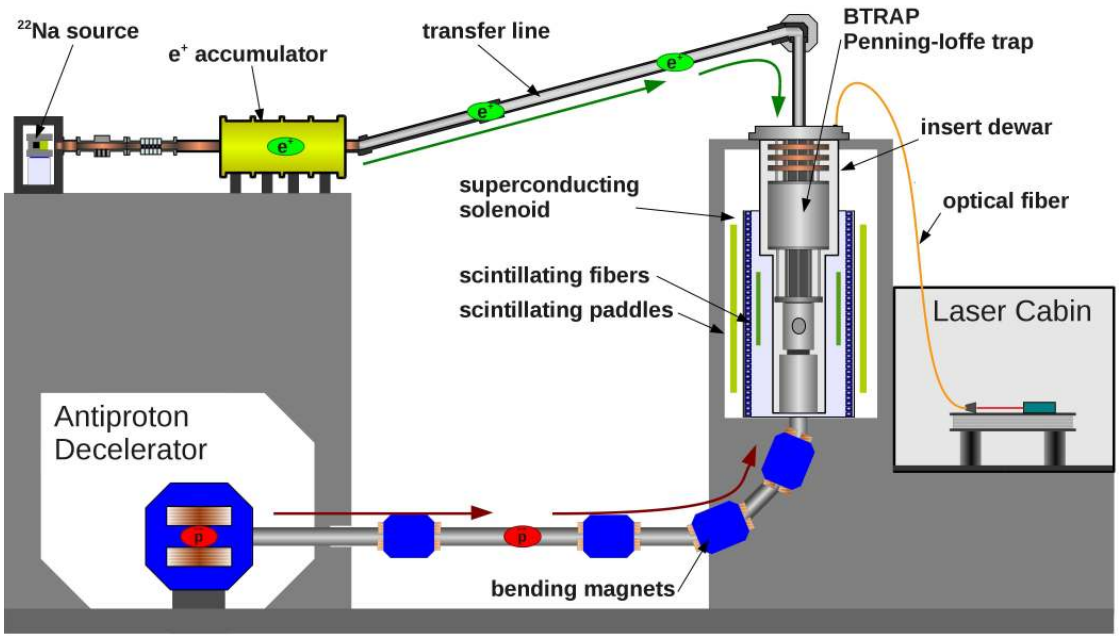

Figure 3.1: Overview of the ATRAP experiment at CERN's Antiproton Decelerator. Antiprotons from the AD and positrons from ATRAP's positron accumulator are transfered into a combined Penning-Ioffe trap for antihydrogen experiments. The trap is shown in more detail in figure 3.8. For thermal isolation, the trap is suspended from the top only and is placed in a thermal insulation container (insert dewar). A superconducting solenoid produces a field of 1 T for radial confinement of the $\bar{p}$ and e^+ in the Penning trap. Laser light for charge-exchange production of antihydrogen is guided from a separate Faraday cage (laser cabin) to the experiment by an optical fiber. Four layers of scintillating fibers and two rings of scintillating paddles are used to detect antimatter particles via their annihilation signatures.

of the electrode stack. This degrader foil reduces the $\bar{p}$ energy by three orders of magnitude, unfortunately at high losses. From the 10^7 $\bar{p}$ emitted per AD shot, about 10^5 are caught in the trap.

The following section starts with our antimatter sources, CERN's Antiproton Decelerator and ATRAP's positron accumulator. Large numbers of e^+ and $\bar{p}$ are

loaded and cooled in a cryogenic Penning trap. Understanding the behavior of the antimatter particles in this trap is an important prerequisite for antihydrogen formation. Therefore, the behavior of charged particles in Penning traps is briefly reviewed in section 3.2. The overview covers the essential properties of single particles as well as the large plasmas required for this work. References to further reading is given.

Section 3.3 attends to the description of the central ATRAP apparatus itself. The heart of the experiment is the cryogenic Penning trap (section 3.3.1). It is located within a large superconducting solenoid that constrains the charged particles radially. It can generate magnetic fields of up to 3 T, but is typically operated at a lower field of 1 T. Cold antihydrogen atoms are confined by a quadrupole Ioffe trap that surrounds part of the Penning trap's electrode stack (section 3.3.2). An alkali metal dispenser (AMD) emits a beam of cesium for charge-exchange production of $\bar{H}$. The Cs atoms are laser excited before crossing the electrode stack in right angle through a pair of small holes in one of the electrodes. This system is described in detail in section 3.3.3. The lasers, treated separately in chapter 4, are located in a Faraday cage next to the experimental zone. The laser light is guided to the excitation region within the apparatus through an optical fiber.

The annihilation signatures of antimatter particles are an essential diagnostic for our experiments. They are recorded by a two-component detector system consisting of four layers of scintillating fibers within the bore of the solenoid and two layers of scintillating paddles around the magnet. The system is described in section 3.4. The analysis of the detector data is covered later in section 6.4.2.

3.1 Particle Sources

3.1.1 The Antiproton Decelerator

Antiprotons have to be generated artificially by pair production. This process requires energies at least equal to the rest mass of the particles. For p-$\bar{p}$ pairs, this corresponds to $E \geq 1.88\,\mathrm{GeV}$. However, the cross section for pair production with the minimum energy is very low. It significantly increases at higher energies which are available at accelerator facilities. The antiproton production at CERN happens on impact of a proton beam with an energy of 25 GeV onto an iridium target. The antiprotons produced retain a significant fraction of the proton's initial kinetic energy, in case of the CERN facility 3.6 GeV. To store them in a Penning trap for atomic physics experiments, their energy has to be reduced by six orders of magnitude. Once trapped, the antiprotons must be cooled by another seven orders of magnitude to make antihydrogen atoms cold enough to be confined in a neutral atom trap. The deceleration in the AD ring can be done in part with the same radio frequency cavities that are usually used to accelerate charged particles. By changing the phase matching between the radio-frequency (RF) field and the particle bunch, the antiprotons lose energy instead of gaining it. Liouville's theorem states that, for a conservative force, the phase space volume is conserved. Therefore reducing the energy of a particle bunch will increase its spatial extent. To avoid particle loss, the phase space volume of the beam must be compressed by a non-conservative force. Two methods applied in storage rings are stochastic cooling [103] and electron cooling [21]. In this context, cooling refers to a reduction of the phase space volume only while deceleration means the reduction of longitudinal kinetic energy.

The Antiproton Decelerator is a user facility that provides antiprotons with

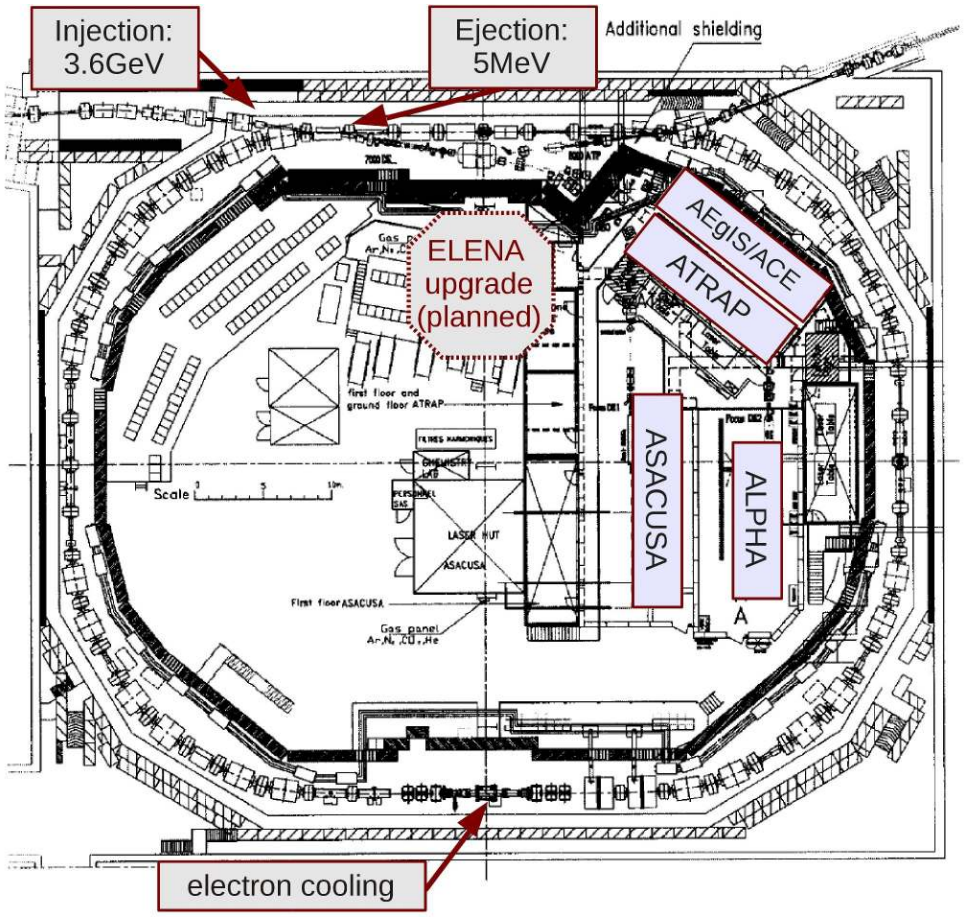

Figure 3.2: Overview of the AD hall. The antiprotons are produced just outside the top left of the figure. They are injected into the ring with an energy of 3.6 GeV and circulate clockwise while being cooled to 5.3 MeV. From the ejection point, the beam is distributed to four experimental areas occupied by various experiments.

energies of 5.3 MeV for several experiments located within the AD hall. A floor plan is shown in figure 3.2. The AD ring with a circumference of 188 m is located behind concrete shielding blocks at the outer edge of the hall while the experiments are placed inside the ring. The research program includes, among other topics, CPT tests with antiprotons and antihydrogen (ATRAP [62,64], ALPHA [3,10]), the study

of exotic atoms (ASACUSA [57, 85]), the interaction of antiprotons with organic matter (ACE [88, 119]) and, currently being set up, the gravitational interaction between matter and antimatter (AE$\bar{g}$IS [48], gBAR [27]).

The AD started operation in 2000. It is the successor of CERN's earlier antiproton complex which consisted of three rings. The Antiproton Accumulator (AA) and the Antiproton Collector (AC) were built to provide high density bunches of antiprotons for p-$\bar{p}$ collisions in the storage rings ISR and SPS and for experiments at the Low Energy Antiproton Ring (LEAR). LEAR enabled the first measurements with low energy antiprotons confined in a Penning trap [60] and the first production of antihydrogen atoms [13]. The latter resulted in a sudden and unprecedented public interest in CERN and its research program. CERN's antiproton complex was decommissioned in 1996 to free resources for the Large Hadron Collider (LHC), but due to the important breakthroughs and the high demand for low energy antiprotons for further experiments, CERN decided to upgrade the AC to a facility that integrated $\bar{p}$ accumulation, cooling and distribution in a single machine, named the Antiproton Decelerator.

Antiproton production takes place just before the AD hall. Bunches of 10^{13} protons with energies of 25 GeV from CERN's Proton Synchrotron (PS) hit an iridium target. In this process, about $5 \cdot 10^7$ antiprotons are produced with an energy of 3.6 GeV. The $\bar{p}$ are guided into the AD ring where they are cooled in several stages. Each deceleration step is followed by stochastic or electron cooling to reduce the particles phase space volume. The $\bar{p}$ bunch is decelerated to an energy of 5.3 MeV within $90 - 100$ s. More than 80 % of the initial antiprotons are retained during the process. Typically, a bunch of about $3 \cdot 10^7$ antiprotons is delivered to one of the experiments every 100 s for a shift of eight hours. Since an energy of 5.3 MeV is still too high to directly trap the antiprotons, most experiments further slow the $\bar{p}$

bunches by sending them through a degrader foil. Unfortunately, up to 99 % of the $\bar{p}$ are lost during this process. Since antiprotons are an expensive resource, this high loss is not satisfactory. To improve the situation, CERN approved the installation of an additional small deceleration ring in the AD hall (figure 3.2). The Extra Low Energy Antiproton Ring (ELENA) will further decrease the energy of the $\bar{p}$ bunches down to 100 keV [108]. At this lower energy, thinner degrader foils suffice to stop the antiprotons, which reduces the losses. An increase in catching efficiency of at least an order of magnitude is expected. The AD-ELENA facility will also be able to supply antiprotons to four experiments simultaneously. The procedure for loading antiprotons into our apparatus is described in section 6.1.3.

3.1.2 The Positron Source

Positrons can also be obtained from pair production, similar to the method described for antiprotons. The necessary energies can be achieved with even small electron linear accelerators (LINAC) [112]. Some nuclear research reactors, like FRM II near Munich (GER), can provide positrons at high rates, but they require experiments to be located on site. Additionally, radioisotopes that undergo β^+ decay are a natural source of positrons. Common isotopes are for instance ^{58}Co and ^{22}Na.

Due to the relatively low emission energy of 300 keV, ^{22}Na is preferably used for obtaining positrons for cold precision experiments. ATRAP's positron accumulator is depicted in figure 3.3. While the AD is a CERN facility that supplies antiprotons to several experiments, the positron source is part of the ATRAP experiment. Collaboration members from York University (Toronto, CA) designed, constructed and maintain the system. It consists of several components starting with the actual radioactive ^{22}Na source, a solid neon moderator to reduce the kinetic energy of the

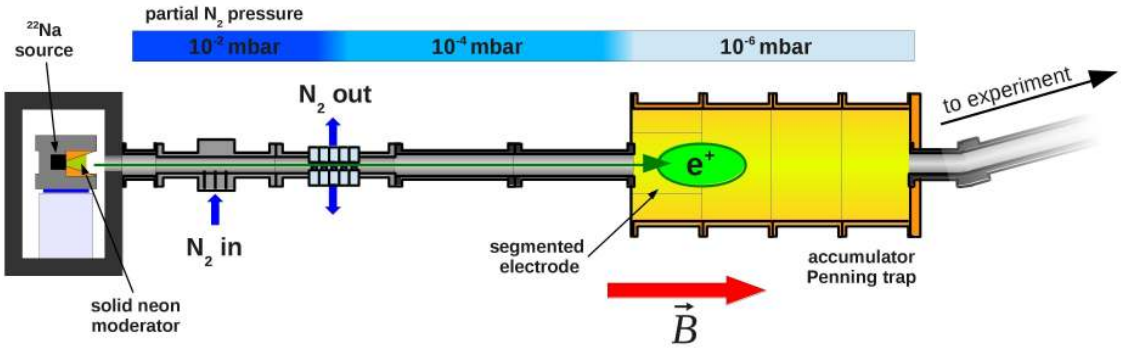

Figure 3.3: Schematic overview of the ATRAP positron accumulator: e^+ emitted from a ^{22}Na source are slowed by a solid neon moderator and a N_2 gas pressure gradient before being caught and bunched in a room temperature Penning trap. From this Surko-type accumulator, they are transfered into the central apparatus once every $\simeq 30\,\mathrm{s}$.

positrons emitted, a Penning trap for accumulation and bunching and a transfer line to guide the e^+ clouds into the experimental apparatus. Due to spatial constraints in the AD hall, the positron source is located several meters away from the actual experiment (figure 3.1), thus the necessity for the long transfer line.

The ^{22}Na emitter is a commercial source (*IThema Laboratories*) containing ^{22}Na salt with an activity of 52.6 mCi (Oct. 2006, half-life: 2.6 years). The back side of the housing is made of tantalum, which serves as a positron reflector while the front facet consists of a 5 μm thin titanium foil through which the e^+ can pass. The surrounding is shielded with lead blocks to reduce the ambient radioactive dosage.

After passing the titanium foil, the positrons are slowed in a solid neon moderator. Since neon has a melting point of 24.5 K, this part of the apparatus is cooled to 3 K with mechanical refrigerators. To prevent the positrons from stopping and annihilating within the neon, a bias of 11.7 V is applied that ejects them from the moderator. A magnetic field of $10 - 20\,\mathrm{mT}$ guides the particles into a Surko-

type positron accumulator [107]. The accumulator combines a room-temperature Penning trap for confinement of charged particles (see section 3.2) with an N_2 gas pressure gradient. The positrons enter in a high pressure region and rapidly loose energy by collisions with the N_2 molecules. When their energy is sufficiently low, they are confined in an electrostatic potential minimum in the Penning trap. To reduce annihilation losses, the gas pressure in the trap is several orders of magnitude lower than in the collision region. A segmented electrode applies a constant rotating wall drive to compress the particle cloud (see section 3.2.3). Typically, positrons are accumulated for 30 s so that for each antiproton pulse from the AD, three bunches of positrons are sent into the experiment. The positrons are guided up a 15° bend, along a 6 m transfer line, around a 105° bend and through a 1.5 mm diameter pumping restriction of 20 mm length (figure 3.1). The pumping restriction separates the vacuum space of the positron accumulator from that of the trap. In total, the positrons have to travel a distance of 10 m from the accumulator to the cryogenic Penning trap. A 63 V pulse accelerates the particles out of the accumulator. They are guided by numerous room temperature coils along the transfer line. Once the particles reach the 105° bend, they are mostly guided down by the fringing field of the large superconducting solenoid. Despite the challenging path from the accumulator to the trap, the transfer efficiency into the trap is almost unity. The positron transfer line is described in detail in [33]. In contrast to the 5.3 MeV $\bar{p}$, the e^+ arrive with much lower energies of 63 eV. They are slow enough to directly catch them in an electrostatic potential well without the necessity of a degrader foil. This is described in section 6.1.2. A publication of the positron system is under preparation [56].

3.2 Charged Particles in Penning Traps

ATRAP produces antihydrogen from trapped antiprotons and positrons, which first requires catching and storing the charged antimatter particles. From Gauss' law it follows that charged particles cannot be completely confined with electrostatic fields alone since no three dimensional electrostatic field minimum exists. In a Penning trap, charged particles are stored by superimposing an electrostatic quadrupole potential for axial confinement and a homogeneous magnetic field to constrain the particles radially. Quadrupole potentials are used because the motion of a charged particle in such a potential can be treated as three decoupled harmonic oscillators (see section 3.2.1). A quadrupole potential can be generated by three hyperbolic electrodes: two end caps and a ring, as shown in figure 3.4(a). The potential is described in cylindrical coordinates by

$$\Phi(r,z) = \frac{V_0}{2d^2}\left(z^2 - \frac{1}{2}r^2\right), \tag{3.1}$$

with the trap's characteristic length scale $d^2 = \frac{1}{2}\left(z_0^2 - \frac{1}{2}r_0^2\right)$ [20]. The two lengths r_0 and z_0 are the trap's inner radius and its axial half-length, respectively. V_0 is the voltage applied between the end caps and the ring electrode.

Penning traps with hyperbolic electrodes are difficult to machine with high precision. Furthermore, they do not allow easy access for particle loading. A good approximation to a quadrupole potential can also be generated by a stack of cylindrical electrodes [67], as depicted in figure 3.4(b). Such a cylindrical trap can consist of a large number of electrodes which allows simultaneous confinement of two particle species of opposite charge like $\bar{p}$ and e^+ in a nested well potential (see figure 2.1). The potential in a stack of ring electrodes can be written as a series expansion

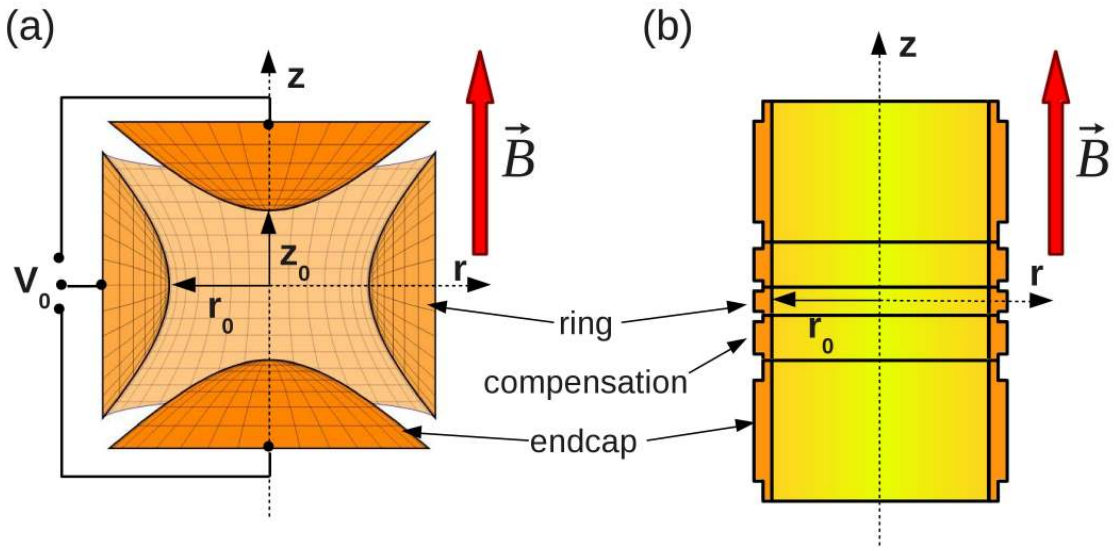

Figure 3.4: Two types of Penning traps: Traps with hyperboloid electrodes (a) produce very clean quadrupole potentials but are difficult to machine and only offer limited access for particle loading. A stack of ring electrodes (b) can also produce a very good quadrupole potential but doesn't suffer from these drawbacks. Also, a cylindrical electrode stack can generate various potential structures for trapping and manipulating antiprotons and positrons in the same apparatus. For examples, see chapter 6.

in Legendre polynomials $P_k(cos\theta)$ in spherical coordinates

$$\Phi(r,\theta) = \frac{1}{2}V_0 \sum_{k=0}^{\infty} C_k \left(\frac{r}{d}\right)^k P_k(cos\theta)\,, \tag{3.2}$$

with the coefficients C_k. C_0 is an unobservable offset [58]. For a trap symmetric along the $\hat{z}$ axis, the odd coefficients vanish. C_2 describes the quadrupole part of the potential while the higher order coefficients quantify deviations from an ideal harmonic trap. Large anharmonic contributions to the potentials can cause unwanted behavior like dependence of the particles' eigenfrequencies on their motional amplitude, coupling of the three eigenmotions (section 3.2.1) and expansion of plasmas (section 3.2.2). Deviations from the ideal quadrupole potential are dominated by the

coefficients C_4 and C_6. When constructing a cylindrical Penning trap, these anharmonic contributions can be minimized by choosing appropriate electrode lengths, for instance a five electrode stack with a center ring electrode and two compensation- and endcap electrodes to either side [67]. This geometry is depicted in figure 3.4(b). A trap where both C_4 and C_6 are zero is called "compensated". Antihydrogen experiments at ATRAP take place in large stack of identical electrodes (section 3.3.1). In such a trap, complete compensation is typically not possible, but the anharmonic contributions can be greatly reduced by an appropriate choice of the voltages applied to each electrode.

The total potential at any point in a stack of cylindrical electrodes can be calculated as a superposition of the potentials generated from each electrode:

$$\Phi(r,z) = \sum_{j=1}^{N} \Phi_j(r,z) V_j \,. \tag{3.3}$$

The sum runs along the stack, adding the contribution from each electrode. $\Phi_j(r,z)$ is the potential generated from electrode j at the point (r,z). It can be determined for instance by numerical calculations. These are typically computed for a fixed voltage of 1 V, so they have to be scaled by the actual voltage applied to the electrode V_j. The potential structures shown in chapter 6 are calculated with this method.

3.2.1 Single Particle Motion

This section provides an overview over the motion of a single particle in a Penning trap. Antihydrogen experiments use large clouds, or plasmas, which are the subject of the following section. However, to understand the properties of these plasmas, it is useful to first review the behavior of single particles. For a more detailed

treatment see for instance [20].

In a homogeneous magnetic field along the $\hat{z}$ axis, $\vec{B} = B\hat{z}$, a charged particle circulates around the field lines with the cyclotron frequency

$$\omega_c = \frac{q}{m} B \,, \tag{3.4}$$

where q is the particle's charge and m its mass. Adding the electrostatic quadrupole potential (3.1) alters the particle's trajectory. The equations of motion in cylindrical coordinates are given by:

$$m\ddot{z} = qE_z = -q\frac{V_0}{d^2} z \,, \tag{3.5}$$

$$m\ddot{\vec{\rho}} = q\left(\vec{E}_\rho + \dot{\vec{\rho}} \times \vec{B}\right) = q\left(\frac{V_0}{2d^2}\,\vec{\rho} + \dot{\vec{\rho}} \times \vec{B}\right) . \tag{3.6}$$

The motion along the trap axis $\hat{z}$ parallel to $\vec{B}$, equation (3.5), is only governed by the electric field. It is a harmonic oscillation with the axial frequency

$$\omega_z = \sqrt{\frac{qV_0}{md^2}} \,. \tag{3.7}$$

The motion in the radial plane is determined by both the electrostatic and the magnetic field. The solution of equation (3.6) can be found for instance in [20] or [98]. It is a superposition of two harmonic oscillators with the frequencies

$$\omega_\pm = \frac{\omega_c}{2} \pm \sqrt{\frac{\omega_c^2}{4} - \frac{\omega_z^2}{2}} \,. \tag{3.8}$$

The sum frequency ω_+ is called the reduced or modified cyclotron frequency. It is a fast rotation around the magnetic field lines, similar to the cyclotron motion in a purely magnetic field. The difference frequency ω_- corresponds to a slow rotation at large radii, named the magnetron motion. It is an $\vec{E} \times \vec{B}$ drift velocity independent

of particle mass. The complete trajectory of a charged particle in a Penning trap is shown in figure 3.5. It is a superposition of the three harmonic oscillations described above.

The reduced cyclotron energy is purely kinetic, the axial energy oscillates between potential and kinetic energy. In both cases a reduction of the total energy will lead to a decrease of the amplitudes and the motions are stable. This is not the case for the magnetron motion. A decrease of magnetron energy will increase the magnetron radius, causing the particle to eventually hit the wall of the trap. Fortunately, the dampening of this motion has a very large time constant so it is metastable and confinement times of weeks and months are possible.

From equation (3.8) follows the stability condition

$$\omega_c > \sqrt{(2)}\omega_z \,. \tag{3.9}$$

In typical cases $\omega_c \gg \omega_z$ so that the reduced cyclotron frequency ω_+ is only slightly smaller than the free particle cyclotron frequency ω_c.

In general, the three eigenfrequencies in a Penning trap obey the relationship:

$$\omega_+ \gg \omega_z \gg \omega_- \,. \tag{3.10}$$

For an electron or a positron these, frequencies typically differ by three orders of magnitude while for heavier particles like protons or ions, relation (3.10) is less pronounced.

Penning traps find numerous applications for precision experiments. For instance, the most stringent tests of quantum electrodynamics were achieved by measuring g-factors in Penning traps [78, 127]. The g-factor can be determined from the ratio of the cyclotron frequency (3.4) and the Larmor frequency, the precession

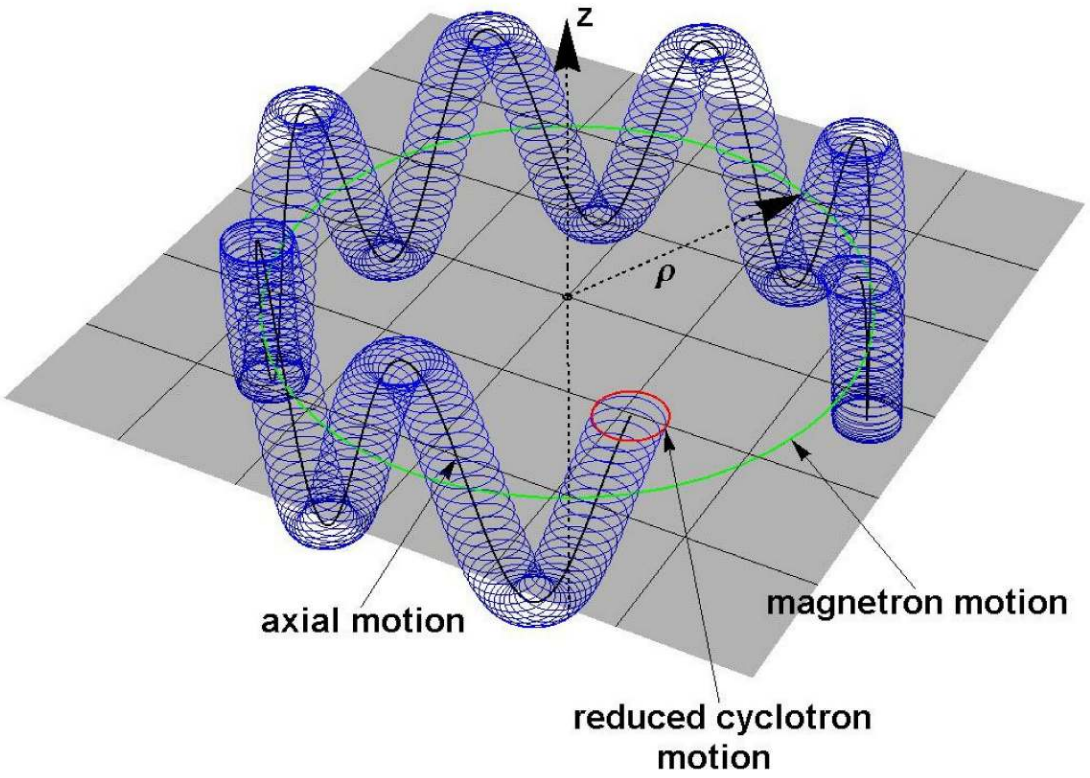

Figure 3.5: Complete trajectory of a charged particle in a Penning trap. The path is a superposition of three harmonic oscillations: An axial oscillation with the frequency ω_z, a fast rotation around the magnetic field lines with the reduced cyclotron frequency ω_+ and the slow magnetron motion with the frequency ω_-.

frequency of the particle's spin around an external magnetic field:

$$\omega_L = \frac{g}{2}\frac{q}{m}B = \frac{g}{2}\omega_c\,, \tag{3.11}$$

$$\Rightarrow g = 2\frac{\omega_L}{\omega_c}\,. \tag{3.12}$$

These experiments need to measure ω_c, which is not directly accessible in a Penning trap since it is not one of the three eigenfrequencies. Fortunately, a relation exists

that links these eigenfrequencies to ω_c [20]:

$$\omega_c^2 = \omega_+^2 + \omega_z^2 + \omega_-^2 \,. \tag{3.13}$$

The cyclotron frequency ω_c can therefore be determined by measuring the three eigenfrequencies in the Penning trap.

3.2.2 Plasmas

Our antihydrogen experiments use large numbers of several 10^6 antiprotons and 10^8 positrons. Although these clouds of charged particles are confined by the same electric and magnetic fields, their behavior differs from that of single particles. Since the clouds used here mostly consist of a single particle species and therefore have a net charge, they are referred to as non-neutral plasmas. The key properties of non-neutral plasmas required for this work are reviewed here, for further reading see for instance [50] and [37].

Within the cloud, the particles rearrange and shield out electric fields over the scale of the Debye length

$$\lambda_D = \sqrt{\frac{\epsilon_0 k_B T}{n q^2}} \,, \tag{3.14}$$

where q is the charge of a single particle, n is the density of the cloud and T its temperature. In general, one refers to a particle cloud as a plasma if its spatial extent is much larger than the Debye length. This is the case for our clouds with dimensions of mm to cm while $\lambda_D \simeq 10 - 100\,\mu$m.

The accumulated charge of all particles generates an electric potential, the space charge or self-potential. It can reach magnitudes of several V. To keep the particles confined, the external potential of the Penning trap must be larger than the space

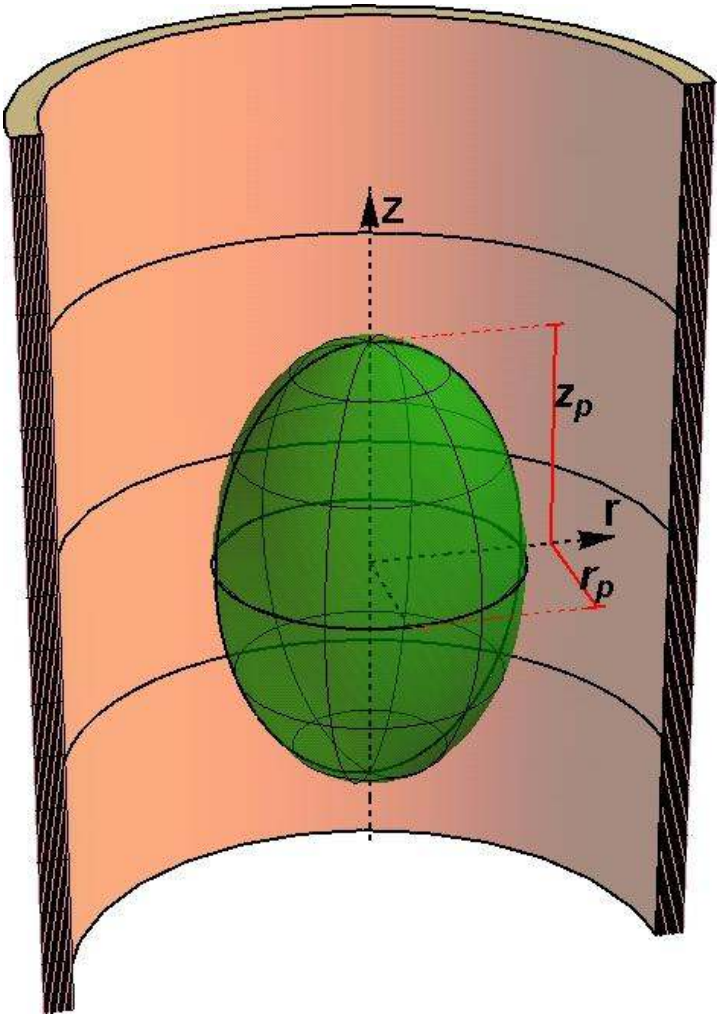

Figure 3.6: A non-neutral plasma confined by a harmonic potential in a Penning trap. The plasma takes the form of a spheroid with radius r_P and axial half-length z_P.

charge potential. The particles affect each other by Coulomb interaction. At thermal equilibrium, they rearrange their distribution to a constant particle density n. Typical values for our plasmas are $n = 10^{12} - 10^{14}\,\mathrm{m}^{-3}$. Due to the constant density, the potential within the plasma is also constant. Outside its boundaries, it falls to zero within several Debye lengths λ_D.

Within the electrostatic quadrupole potential of a Penning trap, a plasma takes the shape of a spheroid with radius r_P and axial half-length z_P (figure 3.6). The aspect ratio

$$\alpha = \frac{z_P}{r_P} \tag{3.15}$$

is used to characterize its shape. If $\alpha > 1$, the plasma has an oblong shape ("cigar-shape") and for $\alpha < 1$ it is flattened ("pancake shape").

The N particles of a plasma act like coupled harmonic oscillators showing N collective modes. The modes are characterized by a set of integers (l, m) with $l > 0$ and $|m| < l$. Modes with $m = 0$ are cylindrically symmetric. In a cylindrical trap, asymmetric modes with $m \neq 0$ are therefore suppressed. The plasma frequencies are calculated for $T \to 0$ in [49]. For higher temperatures, numerical corrections can be applied [128]. The fundamental mode $(1, 0)$ describes an oscillation of the plasma's center of mass along the trap axis. In an ideal Penning trap, its frequency equals the axial frequency of a single particle. The $(2, 0)$ mode, or quadrupole mode, corresponds to an oscillation of the aspect ratio α. The first two modes $(1, 0)$ and $(2, 0)$ are of special interest. From a measurement of their frequencies, together with the particle number N, all other plasma properties like aspect ratio α and particle density n can be determined [50]. This is used at ATRAP to characterize the plasmas for our experiments.

The trap and the confining potential are rotationally symmetric, therefore the canonical angular momentum is conserved

$$P_\theta = \sum_{i=1}^{N} \left(m\, v_{\theta,i}\, p_i + \frac{q}{2} B\, r_i^2 \right) . \tag{3.16}$$

The first part in (3.16) describes the mechanical angular momentum. Typically, it is several orders of magnitude smaller than the second part, the angular momentum

induced by the magnetic field. It can therefore be neglected so that

$$P_\theta \simeq \frac{q}{2} B \langle r^2 \rangle \,. \tag{3.17}$$

This implies a conservation of the mean square radius if no torque is applied, which is only the case in an ideal trap. Slight asymmetries and imperfections in real traps generate a drag on the plasma which causes expansion over a long timescale. Eventually, the particles will hit the wall of the trap and are lost. In practice, confinement times on the order of hours are easily achieved. Still, a continuous expansion of the plasmas is disadvantageous when similar starting conditions for each experiment are desired. Therefore we use the so-called rotating wall technique to control the plasma radius.

3.2.3 Shaping a Plasma

Control of the plasma shape is important to prepare equal starting conditions for antihydrogen experiments and to counteract the expansion caused by trap imperfections. Compression of the plasma can be achieved by increasing the magnetic field. For the simple case of a single particle this can be seen by equation (3.4). Since this is reversible, the plasma will revert to its original shape if the magnetic field is lowered again.

The mean plasma radius can also be changed by applying a torque that affects the plasmas angular momentum. For a cloud of charged particles, this is possible by means of an azimuthally asymmetric rotating electric field with frequency $\frac{\omega_{RW}}{2\pi}$ [86]. In a Penning trap, such a field can be generated by a ring electrode that is separated into four segments, as shown in figure 3.7. A voltage of the form

$$V = V_0 \, cos \left(\omega_{RW} \, t - \frac{\pi}{2} \, k \right) \,. \tag{3.18}$$

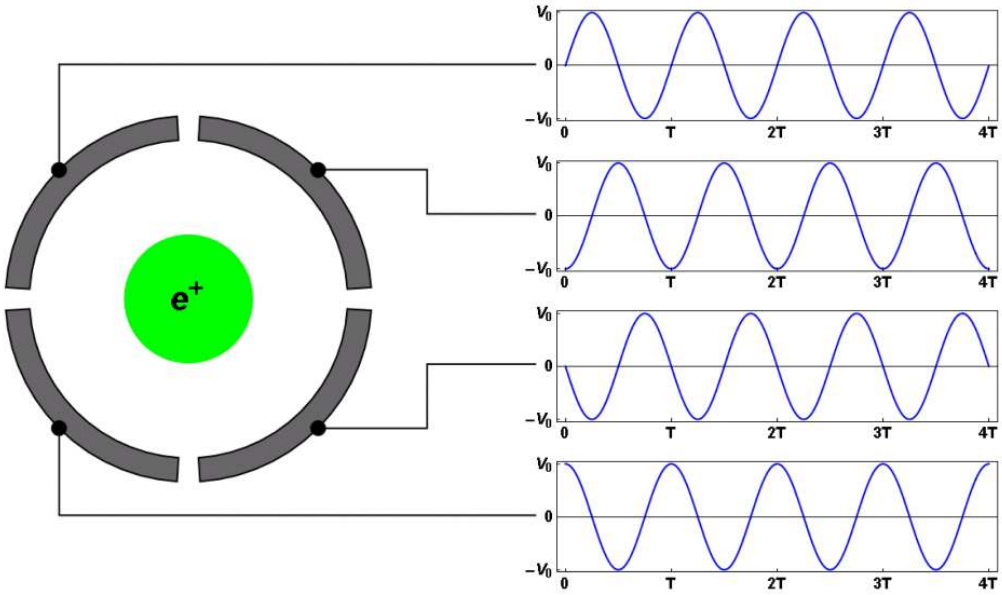

Figure 3.7: Segmented electrode used to apply a rotating wall drive to compress a plasma. An oscillating voltage is sent to each segment with phase shifts of $\pi/2$ to the neighboring segments. This generates a rotating electric field which excites azimuthally asymmetric plasma modes. These modes carry angular momentum which is transfered to the plasma. Thus, the plasmas total angular momentum and therefore the mean plasma radius can be changed.

with $k = 0, 1, 2, 3$ is applied to each electrode segment so that the field oscillates with a phase shift of $\pi/2$ between two neighboring segments. If ω_{RW} is tuned to the right frequency, the rotating electric field excites a plasma mode with $m \neq 0$. These modes are not azimuthally symmetric, they have an angular momentum which is transfered to the plasma. Thus the plasma's total angular momentum can be increased, leading to a reduction of the the mean square radius. The plasma is "spun up". In the same manner, the angular momentum can be decreased on which the plasma expands.

Recently, a different rotating wall regime was found for strong drives and plasmas

with high aspect ratios in large magnetic fields [35,36]. In this so called strong-drive regime, compression of the plasma is achieved without tuning to any plasma modes. The theoretical foundations of this regime are not fully understood yet, but the strong drive regime has been used to compress positron plasmas down to a radius of 2 mm in the ATRAP apparatus.

The rotating wall technique is essential to load the large plasmas for our experiments. While accumulating antiprotons from the AD, the magnetic field around the catching region is increased locally to 3.7 T (section 3.3). When the field is lowered again to 1 T, the $\bar{p}$ cloud expands. To prevent losses from particles hitting the wall of the electrodes, the plasma is spun up to a small radius before lowering the magnetic field. Using this method, the rate and total number of antiprotons accumulated could be significantly increased. For details see section 6.1.3.

3.3 The BTRAP Penning-Ioffe Trap

Figure 3.8 shows a cross section of the ATRAP apparatus, a cylindrical combined Penning-Ioffe trap with a height of 2.2 m. It sits inside a three layer thermal isolation stage called the insert dewar, which is shown in figure 3.1. For maintenance, the trap can be lifted out separately or with the insert dewar. In principle, this allows fast exchange with another trap that has been pre-cooled in a second insert dewar. For thermal isolation, the trap is suspended from the top only. This requires all connections, electrical, optical and mechanical to be fed through the top plate, called the "hat". Beneath the hat are three copper plates covered with aluminized mylar foil that also serve thermal isolation, followed by a liquid helium dewar with a capacity of 40 l. This is enough to ensure cold operation for more than a day before the dewar must be refilled.

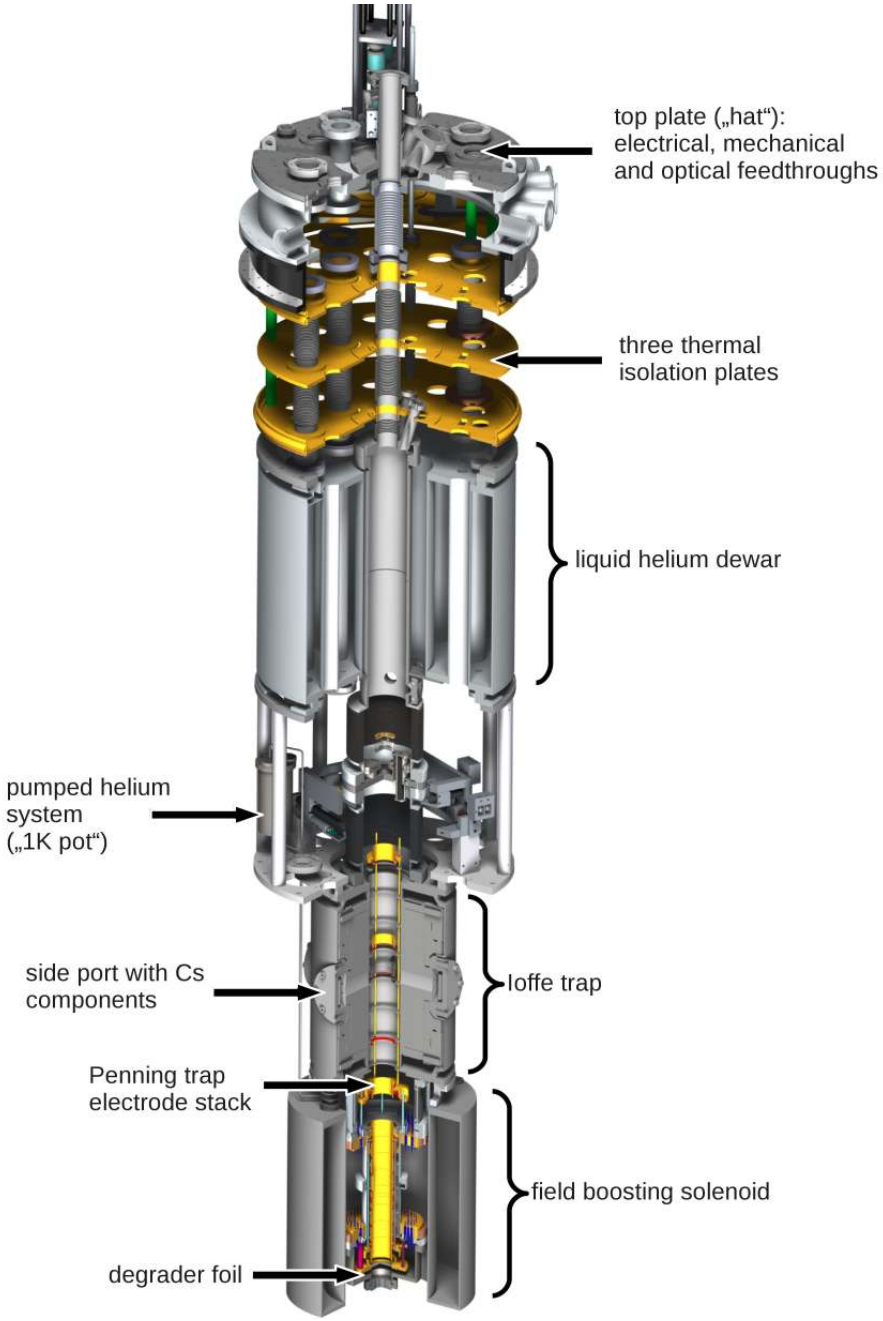

Figure 3.8: The BTRAP combined Penning-Ioffe trap. For details see text.

Previous experiments at ATRAP used a much smaller trap [126]. During the CERN shutdown of 2005, two copies of a new and much larger apparatus were built by ATRAP collaborators from Harvard. The inner diameter of the Penning trap electrodes increased from 12 mm to 36 mm to enable loading and manipulation of much larger particle clouds. The two new traps are internally referred to as ATRAP and BTRAP. The difference is that several additional components, like the quadrupole Ioffe trap, the field-boosting solenoid for antiproton loading and the cesium components, which are described in the following sections, were only built once and are mounted to BTRAP. All experiments for this work were carried out with the BTRAP apparatus. A new apparatus, named CTRAP, with an improved Ioffe trap is currently under construction. Details are found in [90, 116].

The trap and the insert dewar are located within the bore of a large superconducting solenoid for radial confinement of charged particles in the Penning trap. It can generate a uniform magnetic field of up to 3 T. Since its homogeneous field lowers the trapping potential of the Ioffe trap (section 3.3.2), the magnet is operated at a lower field of 1 T. The $\bar{p}$ catching efficiency is higher in stronger magnetic fields since the incoming $\bar{p}$ bunches are compressed to a tighter radius. To compensate for the reduced field, an additional solenoid is installed to boost the magnetic field in the $\bar{p}$ trapping region to 3.7 T. It is only energized during $\bar{p}$ loading and ramped down again before an experiment takes place.

3.3.1 The Penning Trap

To form antihydrogen, positrons and antiprotons must be caught, cooled, and manipulated. This requires a trap with the possibility to generate various potential structures for each specific purpose. To meet these requirements, a large Penning

trap consisting of 39 gold-plated copper electrodes was designed. The entire electrode stack is depicted in figure 3.9. The electrodes are separated by macor spacers. The stack is divided into two parts: The antiproton catching region, or lower stack, and the upper stack which is used for positron loading and most of our experiments. The inner diameter of all electrodes is 36 mm, but different lengths exist. Most electrodes in the upper stack, named *UTRx*, are radius length. A number of electrodes are designed for specific purposes. For instance, the lengths of the two ring electrodes *URING* and *LRING* together with their neighboring compensation electrodes are matched to generate an especially harmonic potential. They have mainly been used for single particle studies [93]. There are two segmented electrodes to apply rotating wall drives for plasma compression (see section 3.2.3). *LTRW* in the lower stack is used to compress the antiprotons during particle loading and *UTRW* in the upper stack fulfills the same task for positrons. The *CS* electrode has two holes on opposite sides that allow a beam of cesium atoms for charge-exchange experiments to cross the electrode stack.

The voltages on each electrode can be set individually which allows complex potential structures like the ones needed for particle loading and antihydrogen production (see chapter 6). Most electrodes are designed for voltages up to $\pm 1\,\mathrm{kV}$, but two electrodes can be biased to $-5\,\mathrm{kV}$ for antiproton catching. These are the *HV* assembly and the beryllium degrader *DEG*, the thin foil that slows antiprotons coming from the AD down to a few keV of energy. All electrodes are also capacitively coupled to micro-coax lines to apply fast voltage pulses to any electrode. This is for instance used to rapidly change potential barriers during particle loading (see sections 6.1.1 to 6.1.3).

The electrode stack is contained in a titanium vacuum enclosure. It is cooled to 1.3 K by a pumped helium system [136] fed from the 40 l liquid helium dewar.

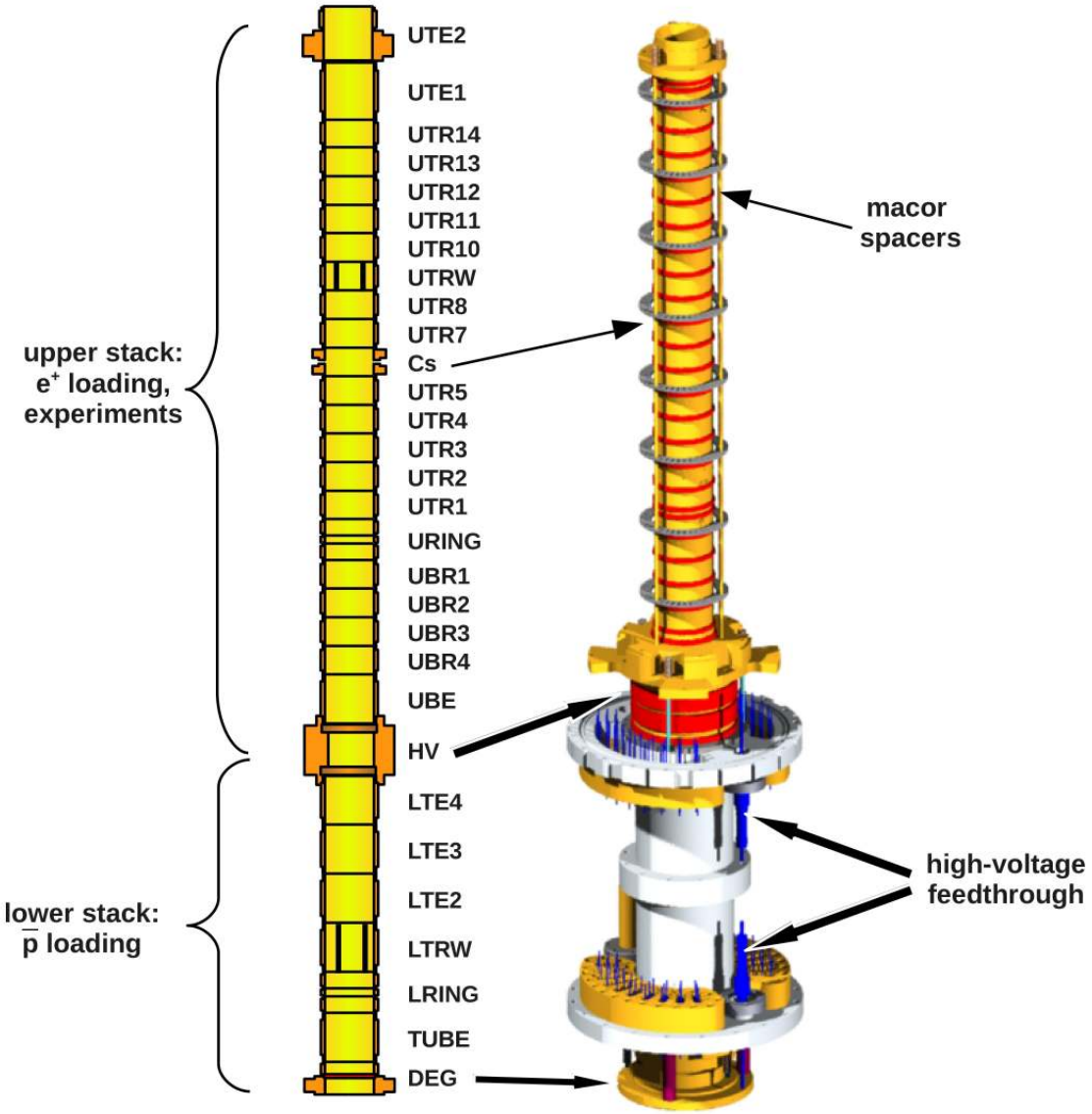

Figure 3.9: The electrode stack of the BTRAP Penning trap shown as a schematic overview (left) and as a technical drawing (right). The stack consists of 39 electrodes with 36 mm inner diameter. The cesium electrode (CS) in the upper stack has two holes to allow a beam of cesium atoms for charge-exchange experiments to cross the stack.

3.3.2 The Ioffe trap

For precision measurements over long timescales, antihydrogen atoms can be confined in a magnetic gradient Ioffe-Pritchard trap [14]. The atomic energy structure of antihydrogen is modified in a magnetic field. Chapter 5 treats the analogous case for cesium atoms in strong magnetic fields. Since cesium is a hydrogen-like atom, the results are very similar. In fact, the calculations for cesium are largely based on the slightly simpler case of hydrogen.

The magnetic interaction produces two additional terms in the Hamiltonian (section 5.1.2). For ground state antihydrogen in a field of several tesla, only one, the paramagnetic shift, has to be considered:

$$H_B = -\vec{\mu} \cdot \vec{B} \,. \tag{3.19}$$

In the $S_{1/2}$ ground state of antihydrogen, the orbital angular momentum is zero ($L = 0$) and only the electron spin ($S = \frac{1}{2}$) contributes which gives

$$H_B = \mu_B \frac{g_S}{\hbar} \vec{S} \cdot \vec{B} \,, \tag{3.20}$$

with the Bohr magneton μ_B and the electron g-factor g_S. If the electron spin is antiparallel to the magnetic field, H_B decreases if the atom travels towards a region of lower magnetic field. Atoms in these so-called low-field-seeking states can therefore be confined in a three-dimensional magnetic field minimum.

Such a field geometry can be generated by three magnets. Two solenoids increase the axial magnetic field at the upper and lower end of the trap and therefore restrict the particle motion in the $\hat{z}$ axis. For radial confinement, a higher order multipole is required. Both quadrupole and octopole coils have been used.

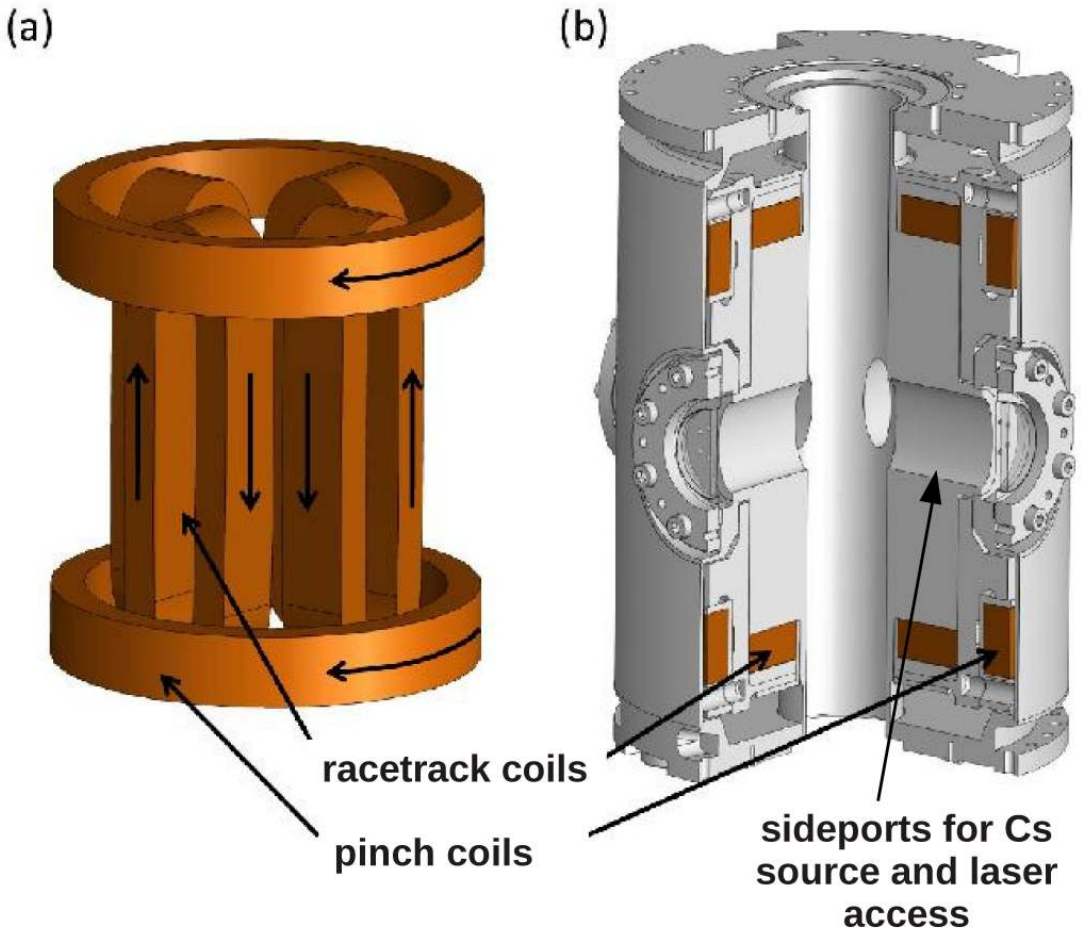

Figure 3.10: The ATRAP Ioffe trap. Figure (a) displays the layout of the superconducting coils that produce the fields for axial (pinch-coils) and radial confinement (racetrack coils). In (b), the full assembly is shown. The four elliptical side ports allow laser access to the electrode stack located in the center of the Ioffe trap (not shown in the figure). Two of the ports contain the components for producing a stream of Rydberg cesium atoms for charge-exchange experiments (see section 3.3.3). Figure taken from [116].

The energy shifts induced by the magnetic gradient fields are very small. Typical trap depths are on the order of $40\,\mu\text{eV} \equiv 0.5\,\text{K}$. This is the reason why antihydrogen atoms must be produced at very low temperatures.

Our Ioffe trap is shown in figure 3.10. It is composed of two solenoids, also called pinch coils, and a quadrupole coil. Due to their shape, the quadrupole windings are also referred to as racetrack coils. The coils are wound from superconducting niobium-titanium (NbTi) wire while the trap's body is made of titanium. The Ioffe trap is cooled to 4 K with liquid helium from the 40 l helium dewar. At maximum current, it generates a potential well with a depth of 650 mK. Including the 1 T field required for the Penning trap, this is reduced to 375 mK. Operating the large solenoid at its full field of 3 T would again half the trap depth.

Four elliptical side ports with dimensions 19 mm × 51 mm allow laser access for future experiments including laser cooling and spectroscopy of antihydrogen. Two of these ports are also used for charge-exchange experiments. One contains the cesium source and the laser excitation region, the other one a field ionization detector. These components are designed to leave sufficient space for laser access. For details see section 3.3.3.

3.3.3 Cs Source

Figure 3.11 shows the setup for generating a beam of Rydberg cesium atoms for charge-exchange experiments. The components are located within two opposite side ports of the Ioffe trap which poses strict constraints on their dimensions. Most of the parts are mounted to a $4\frac{1}{2}$ inch flange that covers one of the side ports.

The cesium atoms are excited to Rydberg states in two steps: A diode laser with a wavelength of 852 nm excites the atoms from the ground state $6S_{1/2}$ to the $6P_{3/2}$

state. The second step to high-n states uses green laser light with a wavelength of 511 nm from a frequency-doubled semiconductor laser. The lasers are described in chapter 4 and excitation of the cesium atoms to Rydberg states is treated in chapter 5. The magnetic field of the large solenoid strongly modifies the atomic energy levels. Additionally, the Ioffe trap generates an inhomogeneous magnetic field which further complicates the determination of the cesium energy levels. The components were designed so that the laser excitation region lies at a maximum of the quadrupole field, thus minimizing the magnetic gradient. The laser light is guided down into the apparatus by a multimode fiber with 62.5 μm inner diameter. The standard FC/PC connector was replaced with a custom non-magnetic holder that connects to the outside of the flange. The light is collimated with a 10 mm diameter ball lens and enters the inner vacuum space through a 1/4 inch window. A mirror redirects the light to meet the beam of cesium atoms. Additional lenses between the flange and the mirror collimate the beam to a diameter of approximately 1.5 mm at the laser excitation region. This rather large spot size ensures that thermal contraction during cool down of the apparatus will not cause the laser beam to miss the cesium atoms. After the excitation region, the laser beams illuminate a silicon photodiode. Its signal is used to monitor the laser power. Also, a misalignment of the laser beams would be detectable with this diode. The laser light crosses the beam of cesium atoms in right angle. The fluorescence from the relaxation of the $6P_{3/2}$ state is recorded with an indium-gallium-arsenide (InGaAs) photodiode. At room temperature, the peak sensitivity of InGaAs is at a wavelength above 1 μm, but at cryogenic temperatures it shifts towards shorter wavelengths. With the signal from this photodiode, the 852 nm laser is tuned to resonance by maximizing the fluorescence signal. To detect excitation to Rydberg states, a field ionization setup is used. An electric field strong enough to ionize high-n states is generated by a

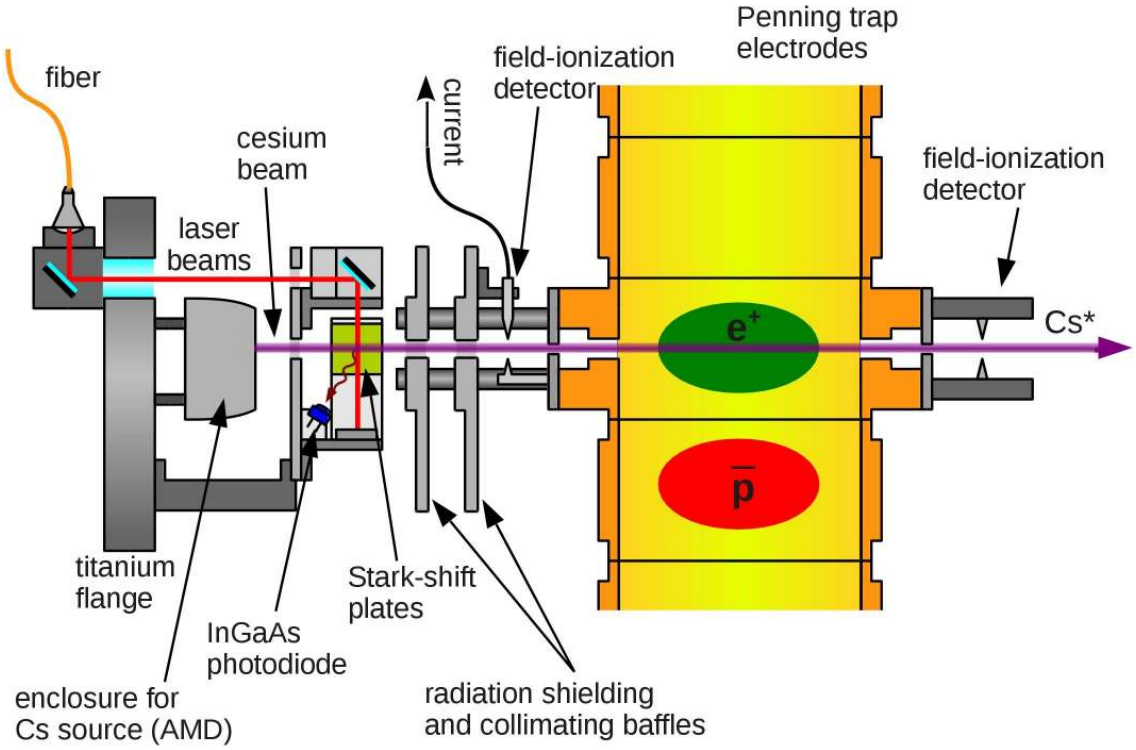

Figure 3.11: Schematic drawing of the components for producing a beam of Rydberg cesium atoms in the ATRAP apparatus. Cesium atoms from an alkali metal dispenser (AMD) are collimated to a thin beam and laser excited before entering the Penning trap through a small hole in one of the electrodes. The 852 nm laser is tuned to resonance by maximizing the fluorescence light recorded with an InGaAs photodiode. The excitation to Rydberg states is detected and maximized with a field ionization detector. Several radiation shield ensure that the electrode stack keeps cold while the cesium oven is operated at 600 K.

voltage on one of two conducting plates and the resulting current onto the other plate is measured. A second field ionization setup is located at the far side of the electrode stack. It detects Rydberg cesium atoms that leave the electrode and thus verifies that *Cs* atoms are crossing through the positron cloud.

The previous experiment used a copper vapor laser which operates at a fixed frequency [126]. The energy levels of the cesium atoms were tuned to resonance with the laser by a pair of Stark shift plates. The copper vapor laser was kept as a backup device, so the current system also includes a pair of Stark shift plates. They are located around the laser excitation region, parallel to the paper plane. Due to reliable performance of the new laser system (see chapter 4) the Stark shift plates were not needed. Still, they could potentially be used for lifetime enhancement of the Rydberg states by modifying their level structure in crossed electric and magnetic fields [87].

Cesium atoms are emitted from a commercial alkali-metal-dispenser (*ALVATEC AS-3-Cs-150-V*). It contains cesium in a bi-metallic compound (Bi_2Cs) surrounded by a non magnetic stainless steel housing. The source releases cesium when it is heated to approximately 600 K by a current of 4 to 5 A through the housing. Operating this source only a few centimeters away from the cryogenic electrode stack requires careful thermal shielding. The cesium source is installed in an aluminum box that is held by ceramic rods with low thermal conductivity. Several additional radiation shields are installed between the source and the electrode stack. Apart from a thin constantan wire to measure the field ionization current, no direct mechanical connection exists between the cesium oven and the electrode stack. The components to the left in figure 3.11, including the cesium oven and the laser optics, are mounted to the flange covering the Ioffe trap side port while the radiation shields and the field ionization detector mount off the electrode stack. These measures lead to a very good thermal decoupling. The heat load on the cryogenic system is on the order of a few W, but even during long experiments with the cesium source running for over an hour, the electrode stack only heats up by about 0.5 K (see figure 3.12). When the oven is turned off, the stack slowly returns to its base temperature.

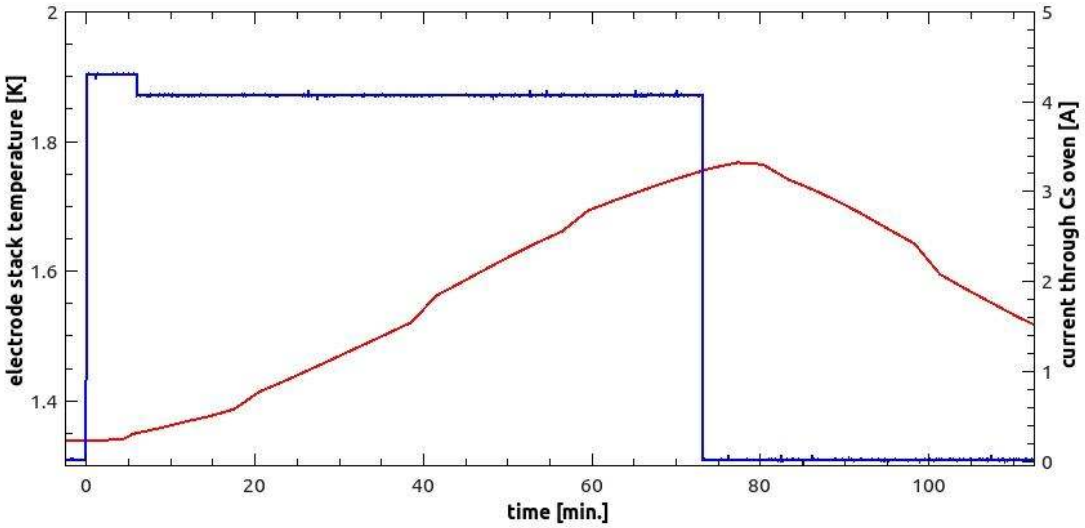

Figure 3.12: Warm up of the electrode stack while the cesium oven is operated at 600 K during a long experiment. The oven is pre-heated to accelerate its warm up to an equilibrium temperature (see text). After 6 minutes, the current is reduced by 0.25 A. The stack warms up to 1.7 K from its base temperature of about 1.3 K. After the oven is turned off, it slowly cools down again.

A number of collimating holes in the radiation baffles ensure that all cesium atoms that enter the electrode stack through a 0.8 mm diameter hole will leave again through a second hole of 2.5 mm diameter on the opposite side. This prevents the buildup of cesium inside the electrode stack which could short two electrodes together or disturb the electric potentials.

The bimetallic compound (Bi_2Cs) in the cesium source reacts with oxygen from the atmosphere. Therefore the housing of the source is filled with argon and the opening is covered with an indium seal. Since indium has a low melting point, the seal liquefies when the source is turned on for the first time. We found that in some cases, the indium would not fully retract, even during several heating cycles.

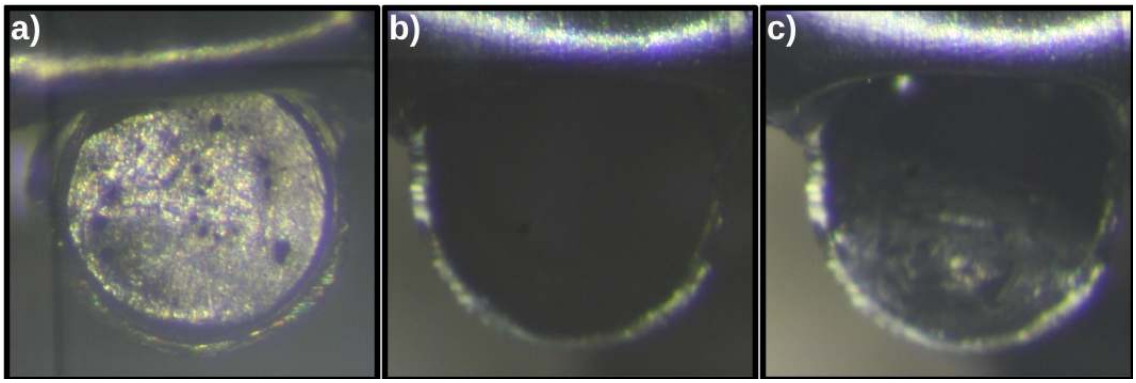

Figure 3.13: Front view onto three cesium ovens showing a new source with an intact indium seal (a), a fully open source (b) and a typical case where the indium only retracted partially (c). Since the remaining indium may prevent cesium atoms from reaching the electrode stack, the seals are removed manually under nitrogen atmosphere during installation.

Figure 3.13 shows the front view onto a new cesium oven with an intact indium seal (a), a fully open source (b) and a typical case where some indium remained (c). The remaining indium may block the emission of cesium atoms on axis and, due to the strict collimation, prevent atoms from reaching the electrode stack. Therefore we manually remove the indium seal before installation. To prevent oxidation, a glove-bag is fitted to the side of the trap and the whole system is filled with nitrogen slightly above atmospheric pressure. The indium seal is then removed within the glove bag. After installation of the source and assembly of the remaining components, the trap is sealed with the *Cs* flange and the glove bag removed. Afterwards, the trap is pumped out and lowered into the insert dewar. This procedure requires that the installation of the cesium oven is the last step before the trap is sealed and readied for a beam run.

3.4 Detector System

The annihilation of an antimatter particle with its matter twin generates a typical signature of secondary particles which can be used to identify even small amounts of antimatter, down to single particles. An electron positron pair produces two 511 keV γ quants while a p-$\bar{p}$ annihilation creates an average of three charged and two neutral pions [7]. Other decay channels exist, but most of them with very low branching ratios. To detect antihydrogen, one would ideally look for a p-$\bar{p}$ annihilation in coincidence with 511 keV photons. Unfortunately, the decay or energy deposition from the pions leads to production and annihilation of e^--e^+ pairs, which generate the same signature as the positron from an antihydrogen atom. Therefore one has to rely on the detection of $\bar{p}$ annihilations and find other methods to discriminate between antiprotons and antihydrogen atoms. This analysis is the subject of chapter 6.4.2.

The ATRAP detector system, built by collaboration members from the Jülich research center, consists of two cylindrical modules coaxial with the Penning trap. A schematic view is shown in figure 3.14. The inner component is a ring of 784 scintillating fibers placed within the large solenoid. Outside of the magnet, two rings of scintillating paddles are located. The pions are minimum ionizing particles, which means that they deposit only small amounts of energy while passing through the surrounding material. Therefore the detection efficiency is the chief concern for choosing the scintillating material. For the fibers, BICRON BCF-12 was selected and the paddles consist of BC404. Although the system is optimized to detect $\bar{p}$ annihilations, the 511 keV gamma quants from e^--e^+ pairs are also observable with the fibers. The efficiency of $\simeq 0.5\,\%$ is rather low, but since we typically use positrons in large numbers of several 10^7 to 10^8, we still get a very clear signal.

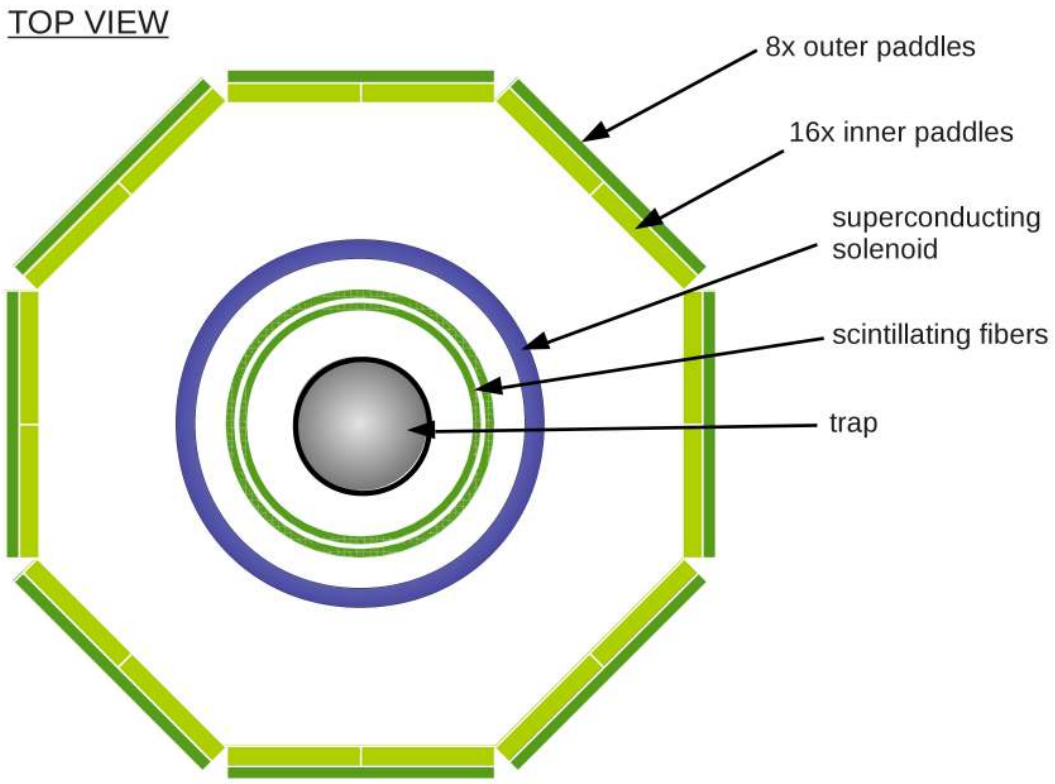

Figure 3.14: Top view showing a cross section of the ATRAP detector system. Four layers of scintillating fibers are installed within the large superconducting solenoid, just around the trap. Additionally, two layers of scintillating paddles are located outside of the solenoid.

3.4.1 Fiber Detector

The fibers are arranged in four layers, each glued to a black Plexiglas tube with grooves milled into their surfaces for mechanical stability. Two layers consists of 224 straight fibers each and the other two layers are each comprised of 168 helical fibers covering an arc of 153°. Each fiber is glued to a separate light guide connected to its own channel of a multi-anode photomultiplier (*Hamamatsu H6568*). Every photomultiplier reads out up to 16 fibers. The fiber ring has an inner diameter of

388 mm and a height of 523 mm. The Plexiglas tubes extend a bit further to support the light guides. The fiber diameter is 3.8 mm. The system was originally designed and built with a total of ten layers of scintillating fibers grouped in three rings, but in order to make space for he Ioffe trap, the two inner rings had to be removed.

3.4.2 Scintillating Paddles

The scintillating paddles are arranged in two octagonal rings. An inner ring of 16 small paddles is surrounded by an outer ring of eight larger paddles. They are arranged so that each of the large paddles is covered by two of the smaller ones (figure 3.14). All paddles are enclosed in light tight packages and each is coupled to a light guide that connects to a *Hammamatsu R2238* photomultiplier tube. The paddles are operated in coincidence mode. An event is only registered when a signal from an inner paddle and the corresponding outer paddle is received within a 40 ns time window.

3.4.3 Data Acquisition System

For each paddle event, the signal, time and amplitude are recorded. For the fibers, only a logic signal is registered for each individual one. The sum of all amplitudes, a multiplicity and a timing signal is taken for each of the 16-fold photomultipliers. The data acquisition system can record events with a rate of up to 1000 Hz with a dead time of less than 20 %. In addition to the full event readout, twelve signal combinations like the multiplicities in individual fiber layers or several coincidence events (triggers) are available via an online readout. This allows immediate diagnostic during an experiment to notice for instance particle losses. The trigger most commonly used for online readout is referred to as "Trigger 1". The condition is a

fiber multiplicity of two or greater and at least one paddle coincidence event. Applying this condition reduces the background rate from several hundred Hz to about 40 Hz while still detecting $\bar{p}$ annihilations with an efficiency of 54 %.

The full system with all three fiber rings installed would also allow vertex reconstruction which could further decrease the background. The single ring only allows determination of intersection points which is still sufficient to divide the events into classes and discard those that most likely originated from cosmic background. Cosmic particles typically travel on a straight line while the pions generated from antiproton annihilations will follow randomly distributed tracks. The analysis of the detector data is treated in section 6.4.2.

Chapter 4

The Laser System

Due to the n^4 dependence of the cross section [82], laser excitation of the cesium atoms is essential to increase the efficiency of the charge-exchange process. A Rydberg state around $n \simeq 40$ is favorable (see section 6.2) and several possibilities exist to excite to this state.

A few excitation schemes were reviewed in [81]. A direct excitation to Rydberg states requires a UV laser operating at 320 nm. Due to the low oscillator strengths, a high power laser is required. With a frequency doubled pulsed dye laser, a mean excitation efficiency of only 1.5 % was estimated [81]. Exciting the atom in several steps increases the efficiency, but additional lasers also add to the technical complexity of the experiment.

For ATRAP's first charge-exchange experiment, the two stage excitation scheme depicted in figure 4.1 was chosen due to an available copper vapor laser [126]. Copper vapor lasers emit light at two wavelengths, 578 nm and 511 nm. The latter corresponds to the energy difference between the excited $6P_{3/2}$ state of cesium and the $37D$ Rydberg state. For the first transition from the ground state of cesium $6S_{1/2}$

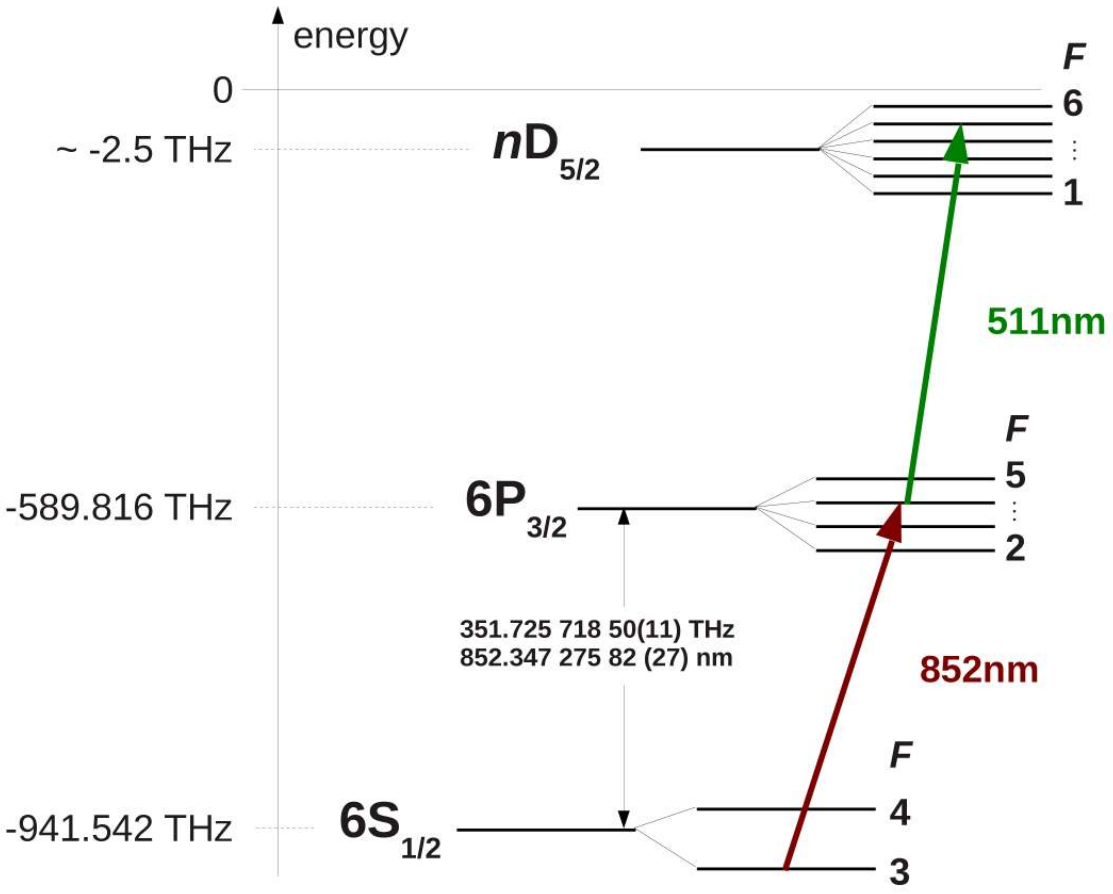

Figure 4.1: Atomic energy levels of cesium and excitation scheme used.

to the $6P_{3/2}$ level, a diode laser with a wavelength of 852 nm was built. Details on this laser system can be found in [81, 113, 121]. The cesium energy levels shown in figure 4.1 are strongly modified by the magnetic fields required for our experiment. The calculation of these modified energy levels is the subject of chapter 5, for the considerations made here, the level scheme in figure 4.1 is sufficient.

All factors considered, the two stage scheme chosen previously is a good compromise. The first transition can be driven by diode lasers which are readily available with wavelengths of 852 nm and typically provide reliable operation while requiring

little maintenance. For the experiments described in this work, we therefore decided to hold on to the excitation scheme previously used.

The copper vapor laser proved to be a useful tool, but also has some limitations: Due to its pulsed operation (20 ns duration every 50 μs), it saturates the transition for a brief time while no excitation happens between pulses. Laser excitation has to take place within the apparatus, close to the positrons. To limit the heat load on the cryogenic trap, the pulse energy had to be limited to 0.025 mJ in [126], about 15 % of the laser's maximum value. The laser light crosses a collimated beam of cesium atoms in right angle (figure 3.11). The atoms have to travel several centimeters from their source to the laser excitation region and on to the positrons. Only atoms with low transversal velocities will pass through the series of collimating apertures on this path. The Doppler-width for atoms that reach the inside of the electrode stack is approximately 12 MHz. Since the copper vapor laser has a spectral width of 6 GHz, only a small fraction of the available laser power actually excites cesium atoms which are usable for charge-exchange experiments. Most of the light sent into the apparatus only contributes to the heat load on the cryogenic system. Furthermore, the laser is not tunable, so only a single Rydberg state ($37D$) is accessible. Higher n-states have a much larger cross section for charge-exchange collisions and longer lifetimes which increases the number of positronium and antihydrogen produced. On the other hand, the excitation efficiency decreases with increasing n and the Rydberg atoms are Stark ionized by weaker electric fields. Due to their space charge, this limits the number of positrons that can be used per experiment. Evaluating these factors to determine which state to use is subject of chapter 6.2. This section shows that the ability to choose an optimum Rydberg state with a tunable laser is a great advantage.

We therefore decided to replace the copper vapor laser with a tunable, narrow-

linewidth continuous-wave (cw) laser system. For operation at an accelerator facility, a compact, reliable, low-maintenance system is especially important. Therefore we chose a frequency-doubled semiconductor master-oscillator power-amplifier (MOPA) laser system. It was initially designed and constructed in [105]. Several improvements were implemented in [18] and during the course of this work [106].

There is extensive literature on semiconductor lasers, so a review is omitted here. For information on diode lasers see for instance [138]. An introduction to tapered amplifiers is found in [133]. The technique of second harmonic generation is also described in literature, see for instance [19].

Section 4.1 starts with a description of the 852 nm diode laser for excitation of the first transition. The laser built in [81] was replaced with a new setup. The frequency doubled MOPA system that replaces the copper vapor laser for excitation of the second transition is treated in section 4.2. Both lasers are stabilized to a wavemeter by a control software developed during this work. This is the subject of section 4.3.

4.1 The 852 nm laser system

The laser system used to excite the first transition is based on an external cavity diode laser (ECDL), similar to [115]. The setup is shown in figure 4.2. The laser diode is a *Frankfurt Laser Company FIDL-200S-850X* with a center wavelength of 850 nm. When heated to a few degrees above room temperature, the center wavelengths shifts towards the 852 nm needed. The maximum output power is 200 mW. The light is collimated with an aspheric lens of short focal length ($f = 4.5$ mm). The emitted laser light illuminates a diffraction grating in Littrow configuration. It is aligned so that the light refracted in first order is sent back into the laser

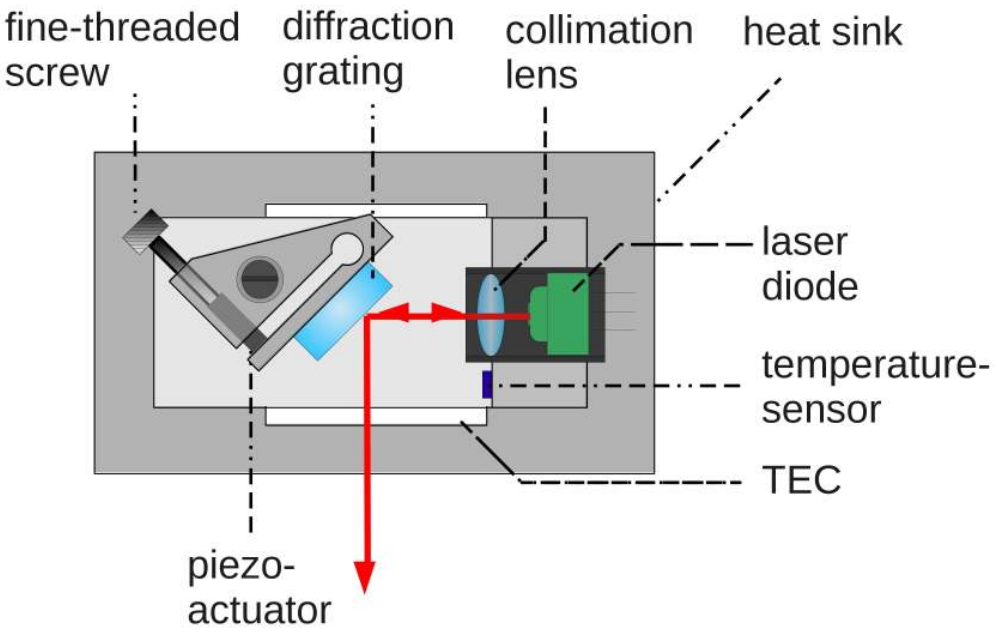

Figure 4.2: Setup of an external cavity diode laser (ECDL). The light emitted from the laser diode is collimated and illuminates a diffraction grating in Littrow configuration. It reflects about $20 - 30\,\%$ of the light back into the laser diode, forming an external resonator. The wavelength is controlled by the grating angle which can be tuned manually by a fine threaded screw or electronically by a piezo actuator. The laser's temperature is stabilized by an external hardware controller (not shown). It reads an *AD590* temperature sensor mounted close to the laser diode and supplies a current to a thermoelectric cooler (TEC) located between the mounting block for the laser components and a copper heat sink.

diode to provide optical feedback. This forms an external cavity with the resonant wavelength

$$\lambda = 2d/k \, \sin\alpha \,, \tag{4.1}$$

where k is the refractive order, d is the groove spacing (inverse grating constant) and α is the angle between the grating normal and the incident light. If the feedback

is strong enough - typically $20-30\%$ of the incident light needs to be reflected back into the diode - the wavelength of the laser can be controlled by the grating angle. Coarse tuning is done with a fine threaded screw that bends the grating's mount. For fine tuning and frequency stabilization, a piezo actuator mounted in the same bore as the screw is used (see figure 4.2). The voltage applied to the piezo is also fed into a modulation input of the laser diode's current driver (feed-forward). With this setup, a mode-jump free tunability of up to 50 GHz is achieved. The grating feedback reduces the available power of the laser, in this case to about 160 mW. Since the $6S_{1/2} - 6P_{3/2}$ transition is easily saturated, this is still far more than needed.

An electronic controller stabilizes the temperature of the laser. It reads a temperature sensor (*AD590*) and applies a current through a thermoelectric cooler (TEC) to either heat or cool the laser.

The entire laser system is depicted in figure 4.3. The beam emitted from the ECDL passes a two stage Faraday isolator with 60 dB attenuation to prevent back reflections into the laser diode. Two beam samplers split off small fractions of the laser light. The first sampled beam is divided between a photodiode that monitors the laser power and a fiber coupler. The light coupled into this fiber is sent to a wavemeter (*HighFinesse WS7*) to monitor the laser frequency (see section 4.3).

The second sampled beam is sent into a setup for Doppler-free saturation spectroscopy of the $6S_{1/2} - 6P_{3/2}$ transition (Cs D_2 line) in a cesium vapor cell. The method is well described in literature, see for instance [38]. Instead of a chopper-wheel and a lock-in amplifier, we use a second probe-beam and a differential photodiode to subtract the Doppler-broadened background. This assembly requires less hardware. The cesium energy levels and transition frequencies have been measured with accuracies much higher than the resolution of the wavemeter [74, 129]. There-

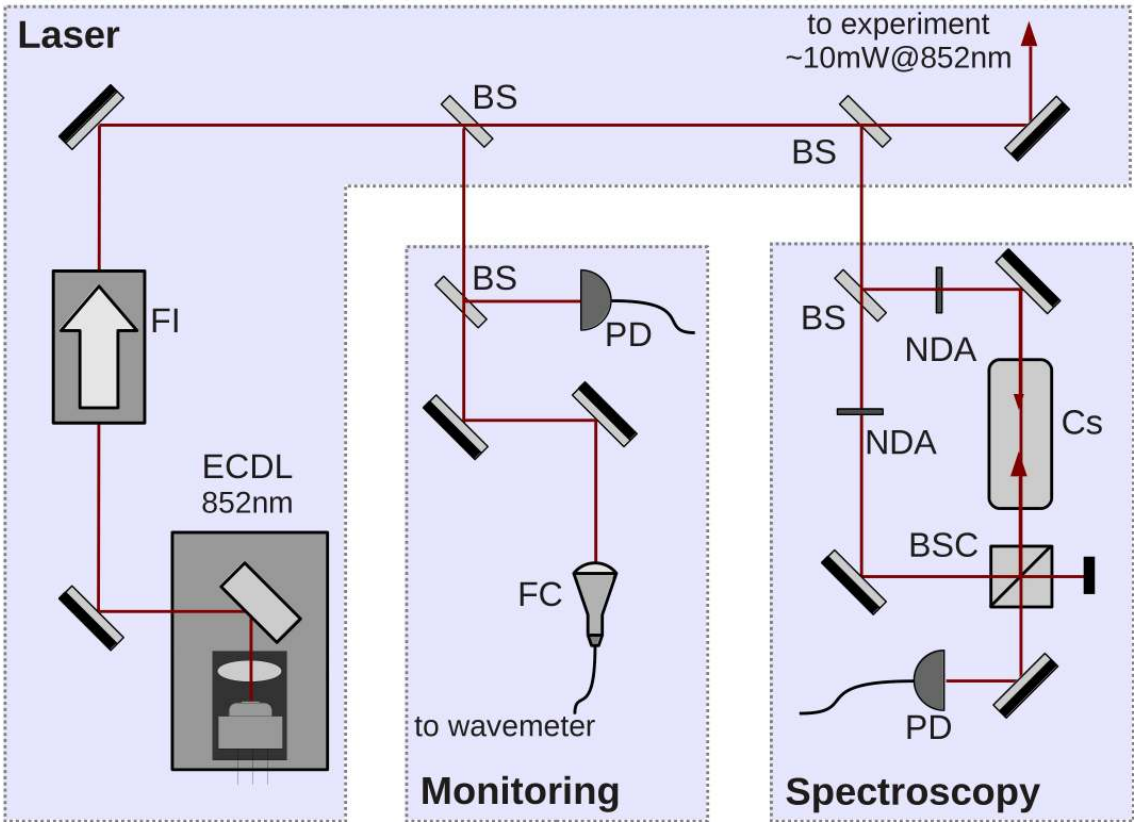

Figure 4.3: The 852 nm laser system for the first excitation step of cesium from the ground state $6S_{1/2}$ to the $6P_{3/2}$ state. **ECDL:** external cavity diode laser, **FI:** Faraday isolator, **BS:** beam splitter, **PD:** photodiode, **FC:** fiber coupler, **NDA:** neutral-density attenuator, **Cs:** cesium vapor cell, **BSC:** non-polarizing beam splitter cube.

fore our spectroscopy setup is suitable as a frequency reference for the wavemeter.

Cesium in its ground state has a single electron in an s-orbital: $S = \frac{1}{2}$, $L = 0$ and $J = \frac{1}{2}$. The nuclear angular momentum of cesium is $I_{Cs} = \frac{7}{2}$ so that $F = 3$ or 4. In the $6P_{3/2}$ state, the electron is elevated to a p-orbital which increments L and J by 1. Therefore $F = 2 \ldots 5$. The spectrum of the cesium D_2 line consists of two groups of three hyperfine transitions each, which correspond to the transitions from

the ground states with $F = 3$ and $F = 4$ with $\Delta F = 0, \pm 1$ (see figure 4.1). The spectrum recorded from the vapor cell is shown in figure 4.4. The peaks labeled with two numbers are artifacts that originate from the spectroscopic method used. They appear in the center between two real resonances. The downward peaks are explained in [118].

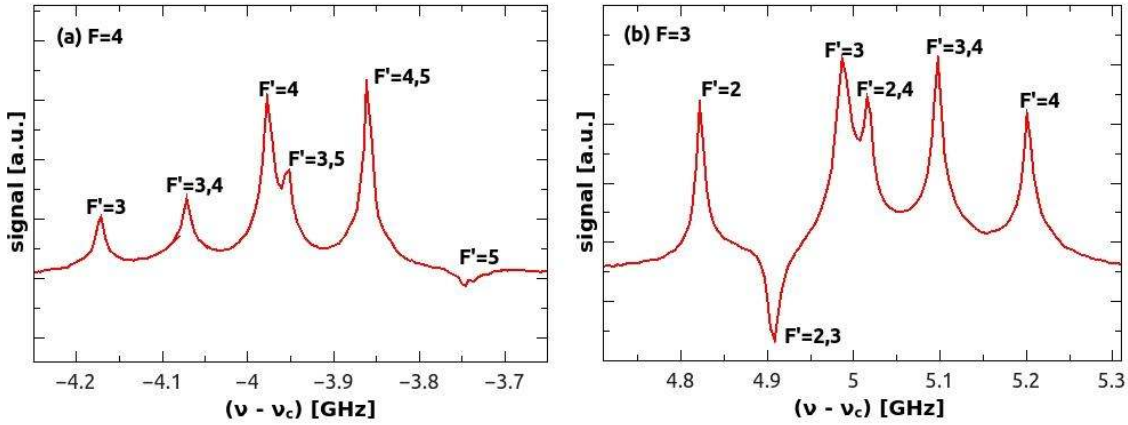

Figure 4.4: The two hyperfine groups of the cesium D_2 line recorded with the setup in figure 4.3. The x-axis shows the frequency relative to the line centroid $\nu_c = 351.72571850(11)\,\mathrm{THz}$ [129]. The FWHM of the individual peaks is on the order of 30 MHz. These spectra are recorded regularly as frequency references for the wavemeter.

4.2 The 511 nm laser system

For the second transition from the $6P_{3/2}$ level to Rydberg states, we replaced the pulsed copper vapor laser with a tunable continuous-wave laser. We designed a master-oscillator power-amplifier system based on semiconductor lasers operating at a wavelength of 1022 nm and a frequency-doubling resonator to convert this light to the required wavelength of 511 nm. The system is depicted in figure 4.5. The

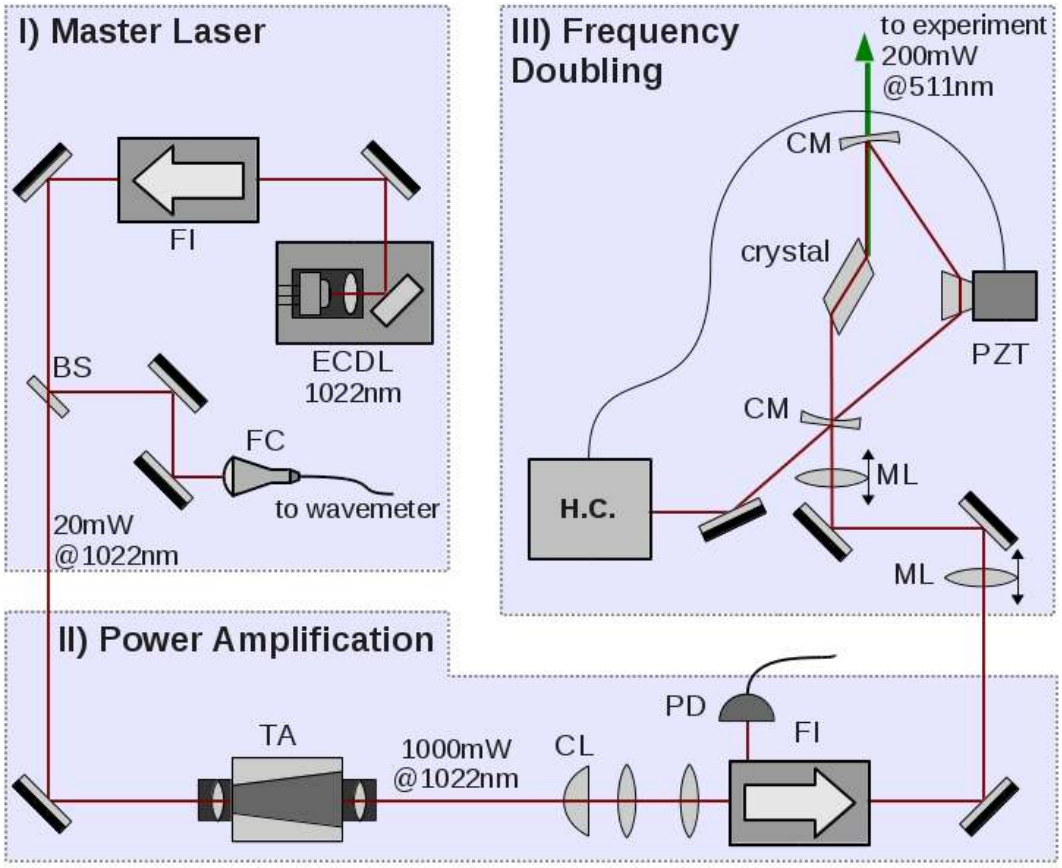

Figure 4.5: The 511 nm laser system for the second excitation step from the $6P_{3/2}$ intermediate level to Rydberg states. **ECDL:** external cavity diode laser, **FI:** Faraday isolator, **BS** beam splitter, **FC:** fiber coupler, **TA:** tapered amplifier, **CL:** cylindrical lens, **PD:** photodiode, **ML:** movable lens, **CM:** cavity mirror, **PZT:** piezo actuator, **H.C.:** components for Hänsch Couilleaud lock.

first component is again an ECDL in Littrow configuration. The laser diode used is an *Eagleyard EYP-RWE-1060* with a maximum output power of 100 mW. With grating feedback, about 75 mW remain. The diode's front facet is antireflection coated which increases the stability of the laser modes and provides better tunability. The diode's center wavelength is 1060 nm, but it can be operated between 980 nm

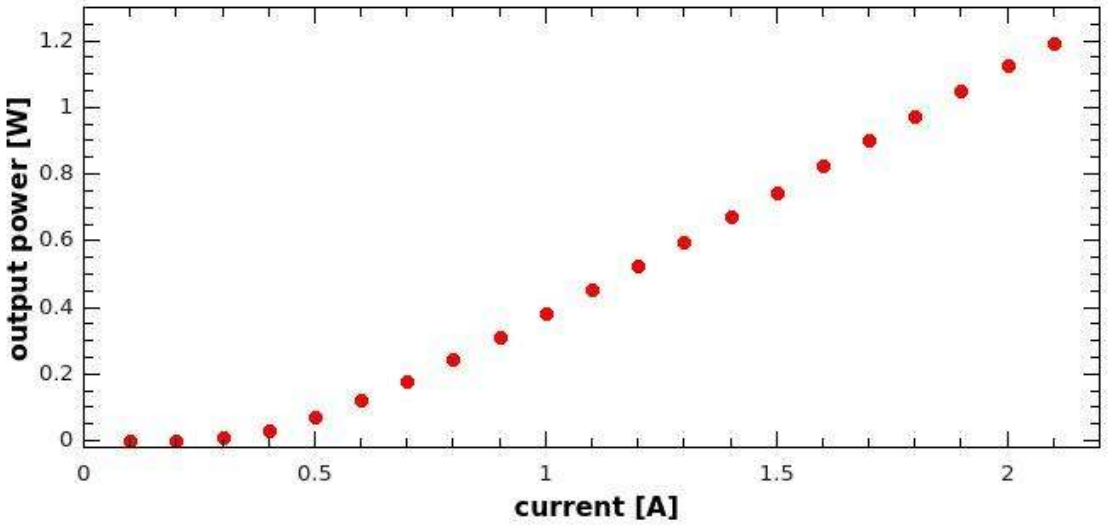

Figure 4.6: Output power of the tapered amplifier in dependence of the current through the chip. The TA surpasses its specified value of 1 W at a current of 2.3 A.

and 1080 nm. A two stage Faraday isolator with 60 dB attenuation (*Linos FI-1060-TI*) protects the diode against back reflections. Part of the beam is split off to monitor the wavelength. About 20 mW of laser power is used to seed a tapered amplifier (*m2k TA-1030-1000*). Its output power is specified to 1 W at an operating current of 2.3 A. As can be seen from figure 4.6, the TA surpasses these specifications. More power is of course beneficial for frequency doubling, however we decided not to run the TA chip above its specified output power. Therefore it is typically operated at a current between 1.9 A and 2 A. In- and outcoupling of the beam is done with two $f = 3.7$ mm lenses mounted on three-axis translation stages (Newport M-DS-25-XYZ). A cylindrical lens corrects the astigmatism of the amplifier's output beam and an additional telescope reduces the beam diameter to increase transmission through a second Faraday isolator (same type as above). This

isolator is especially important since stray light that is reflected back into the chip is amplified too while propagating towards the narrow cross section area of the taper. This can result in a power density high enough to destroy the amplifier's input facet. The light reflected from this isolator's input polarization filter is recorded with a photodiode. This setup allows monitoring of the TA power without deliberately splitting off a fraction of the main beam.

Two lenses on translation stages match the beam's focus size and divergence to a compact resonator for frequency-doubling. It consists of two curved 1/2 inch mirrors ($r = 38\,\mathrm{mm}$) for in- and outcoupling, a nonlinear crystal and a prism [139]. The prism replaces two of the mirrors in the common bow-tie resonator design. This triangular geometry allows a short round trip path length of only 16 cm. Short distances between optical elements reduce beam-pointing from vibrations and other distortions and therefore increase the resonator's stability.

The prism is mounted on a piezo actuator which is used to stabilize the cavity length to be resonant with the wavelength of the fundamental beam. We use a Hänsch-Couilleaud type lock [80]. About 60% of the fundamental light is coupled into the cavity. This value is limited by the tapered amplifier's beam quality. The resonator can only enhance the part of the laser beam that propagates in the fundamental TEM_{00} or Gaussian mode. Due to its rectangular cross section, the beam profile of a tapered amplifier deviates from this ideal shape (see figure 4.7). Quantitatively, this is given by the M^2 value which is a measure for the beam quality in relation to an ideal Gaussian beam ($M^2 = 1$). The manufacturer of the TA chip lists a value of $M^2 < 1.7$ in the datasheet, but a measurement using the knife-edge technique [120] resulted in a value of $M^2 = 2.9$. The cause for this large value is not clear. A possible reason is insufficient alignment of the seed laser beam, but since the TA exceeds its specified output power, this is unlikely. Further investigations

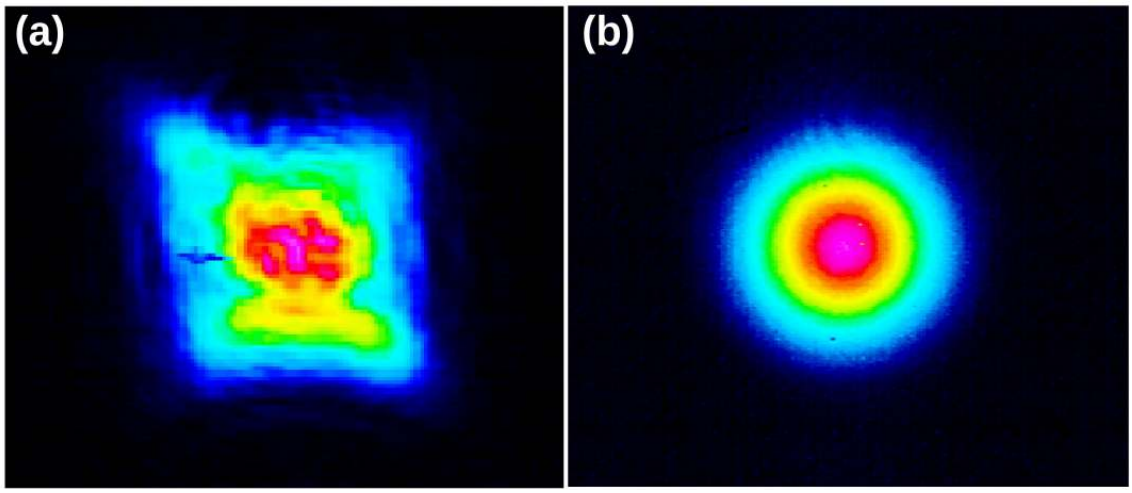

Figure 4.7: Beam profile of the tapered amplifier recorded with a CCD camera (a). The image is color coded, blue corresponds to low, pink to high intensities. The shape of the beam is determined by the rectangular cross section of the chip which significantly deviates from an ideal Gaussian beam. For comparison, (b) shows the beam profile of a helium neon laser.

would require the laser to be disassembled and the TA chip returned to the manufacturer, but since the overall performance is very good, we chose to keep the laser operational.

The nonlinear crystal is cut at Brewster's angle for type I critical phase matching. It is heated to $T = 40°\mathrm{C}$ to prevent deposition of atmospheric water vapor on its surfaces. For the nonlinear medium, we compared lithium triborate (LBO) and bismuth boron oxide (BiBo). BiBo has a four times higher nonlinear coefficient than LBO but also suffers from a larger walk-off angle. In birefringent crystals, the Poynting vector $\vec{S}$ and the wave vector $\vec{k}$ may diverge at the angle ρ [19]. For frequency doubling, this has the negative effect that the spatial overlap of the fundamental and the harmonic beam decreases while they propagate through the crystal.

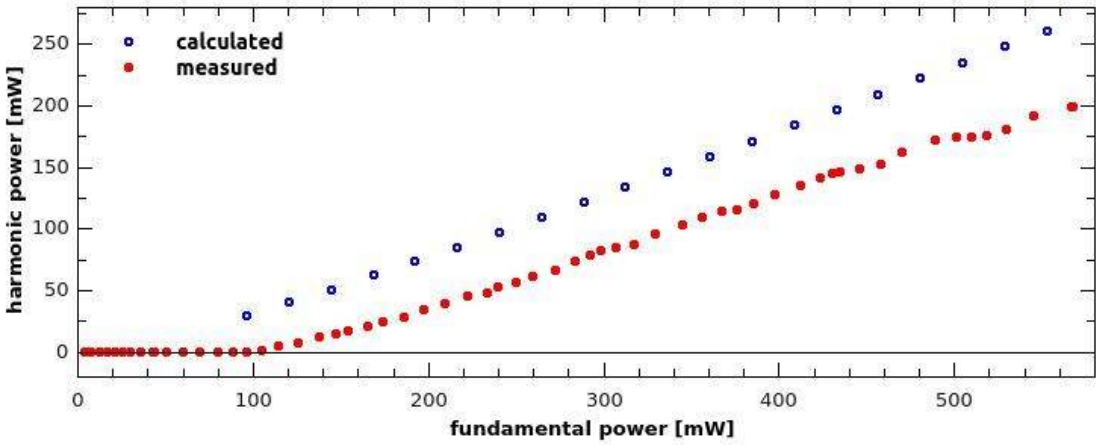

Figure 4.8: Green power generated with the BiBo crystal as a function of the fundamental power (full circles) compared to a theoretical calculation (open circles). We achieve about 75 % of the theoretically predicted value. The x-axis shows the fundamental power corrected for the incoupling efficiency. For comparison, the maximum power reached with the LBO crystal is about 50 mW.

With an LBO crystal of 10 mm length, we generated about 50 mW of output power at a wavelength of 511 nm. Installing an 8 mm BiBo crystal instead increased the output power to 200 mW. This corresponds to a conversion efficiency of 39%, incoupling efficiency included. The harmonic power generated with the BiBo crystal as a function of the fundamental power is plotted in figure 4.8. The output power comes close to a theoretical curve, about 75 % of the calculated value is reached.

We achieve a mode-jump free tunability of more than 20 GHz at a wavelength of 511 nm. The overall tuning range is limited by the tapered amplifier's gain region from 1000 nm to 1040 nm. This allows us to access all cesium states from $n = 20$ (520 nm) up to the ionization limit ($\simeq$ 508 nm).

4.3 Frequency Stabilization

Without stabilization, a diode laser's frequency drifts. This is caused for instance by thermal contraction or expansion of the semiconductor chip which are too small to be compensated by the temperature stabilization. To counteract these drifts, an external feedback loop is applied. The laser's frequency primarily depends on the current running through the chip. Also, the temperature has an effect since thermal expansion or contraction changes the length of the resonator. The two factors are connected since a higher current will also heat the diode. The grating feedback provides a third way to modify the laser frequency. The current and the grating angle can be changed much faster than the temperature, so we use these two to stabilize the laser's frequency. We apply a feedback signal to both simultaneously (*feed forward*).

The laser excitation region lies within strong magnetic fields that influence the atomic energy levels (see section 5.1). Since such strong fields are not available on our laser table, we cannot use a cesium vapor cell as a frequency reference for laser excitation within the apparatus. Instead, we lock both lasers directly to a wavemeter (*HighFinesse WS7*) using a control software (see section 4.4). An optical switcher connected to the wavemeter allows both lasers to be locked simultaneously.

When first measuring cesium resonances, we observed day-to-day fluctuations of the frequencies of 100 MHz and above, part of which seemed to be due to changes of the room temperature. To quantify this effect, we recorded a number of spectra using the Doppler-free spectroscopy of the cesium D_2 line (figure 4.4) at different ambient temperatures measured with the internal temperature sensor of the wavemeter. The data was compared with the values from literature [129]. The results are shown in figure 4.9. The points were taken over several days, so there is some fluctuation due

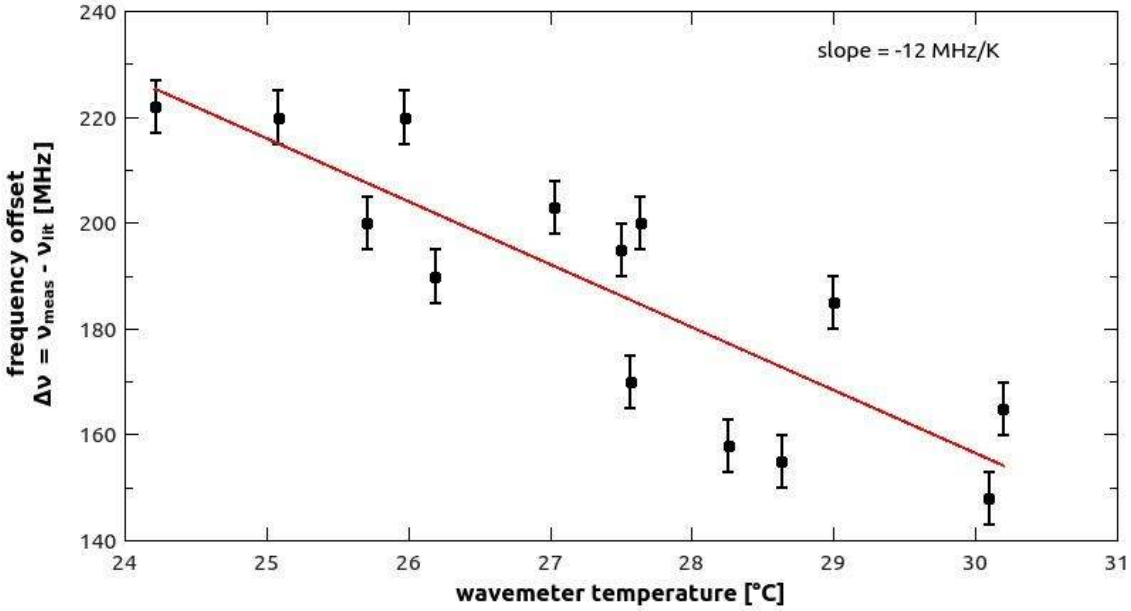

Figure 4.9: Temperature dependence of the measured frequency of the wavemeter. For each point, a spectrum is recorded from the cesium vapor cell (figure 4.4) and compared with literature [129]. The plot shows the difference $\Delta\nu = \nu_{meas} - \nu_{lit}$. The error bars are given by the accuracy of the comparison. The much larger spread of the points originates from the wavemeter's accuracy. The offset from $\Delta\nu = 0$ can be compensated by recalibrating the device with a frequency-stabilized laser. A dependence of the measured frequency on the temperature recorded with the wavemeter's internal temperature sensor of $-12\,\mathrm{MHz/K}$ is observed.

to the limited absolute accuracy of 60 MHz of the wavemeter, but a temperature dependence is observable. The correlation coefficient between T and $\Delta\nu$ is $\rho = -0.85$ and a linear fit results in a slope of $-12\,\mathrm{MHz/K}$. The offset from $\Delta\nu = 0$ can be compensated by recalibrating the wavemeter with a frequency stabilized laser.

Figure 4.10(a) shows the temperature drift of the wavemeter during a day recorded with the device's internal temperature sensor. The laser cabin at the

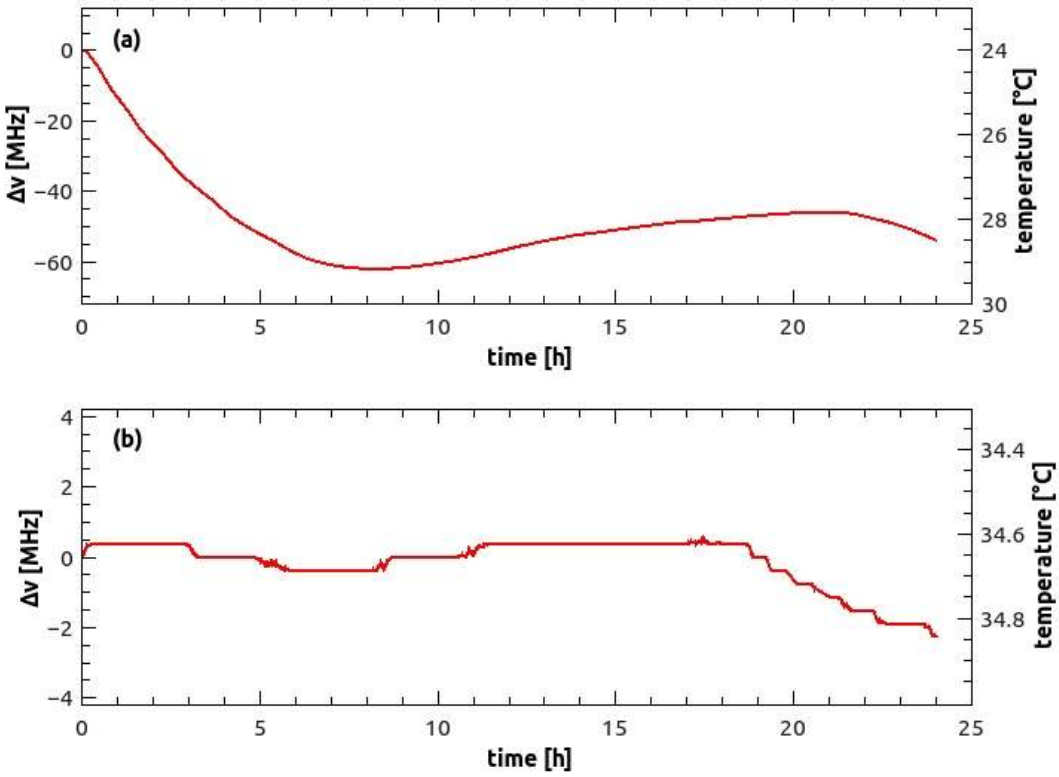

Figure 4.10: (a) Temperature drift of the wavemeter during a day without temperature stabilization. The measured frequency varies over a range of several tens of Hz within a couple of hours. (b) When the device is placed into a temperature stabilized housing, the drift is reduced by a factor of 25 to below 0.2 K. This corresponds to a frequency drift of 2.4 MHz.

ATRAP experiment is not temperature stabilized and the wavemeter experiences differences of up to 5 K during a day. This corresponds to a frequency error of 60 MHz. The Doppler-width for cesium atoms that make it into the center of the trap is about 12 MHz and the time between a frequency calibration and an actual charge-exchange experiment can span a couple of hours, so the laser frequencies can

easily drift off resonance in the meantime. To counteract this problem, we placed the wavemeter into a temperature stabilized box. The housing is made of 1 cm thick aluminum plates and contains four heating resistors. The temperature of the housing is measured with a *PT100* sensor and the current through the resistors is set by a hardware controller. The box is stabilized to a few degrees above room temperature. The stabilization reduces the wavemeter's temperature drift from 5 K to below 0.2 K (figure 4.10(b)). This corresponds to a frequency uncertainty of 2.4 MHz, only about twice the laser linewidth.

We still observe a day to day variation of the cesium transition frequencies on the order of $10 - 20$ MHz. This may be caused either by the residual inaccuracy of the wavemeter or by hysteresis effects from the magnetic fields. Although great care was taken not to include any magnetic materials in the construction of the apparatus, some hysteresis effects appear when ramping the magnets. Some of our magnets, like the field-boosting solenoid (section 3.3) and the quadrupole Ioffe trap (section 3.3.2), may be ramped up and down several times per beam shift. This means we still have to tune the lasers to the cesium resonances before each charge-exchange experiment, but once this is done, they reliably remain on resonance for hours.

4.4 Control Software

Due to the varying magnetic fields present at the laser excitation region, we must be able to lock both lasers to any point within a frequency range of several THz. Using a wavemeter as a frequency reference and a controller loop implemented in software offers the highest flexibility. A prototype program was written in [105]. For this work, the final software was implemented in object oriented Visual C++.

The program is constructed of self-consistent modules. The architecture is de-

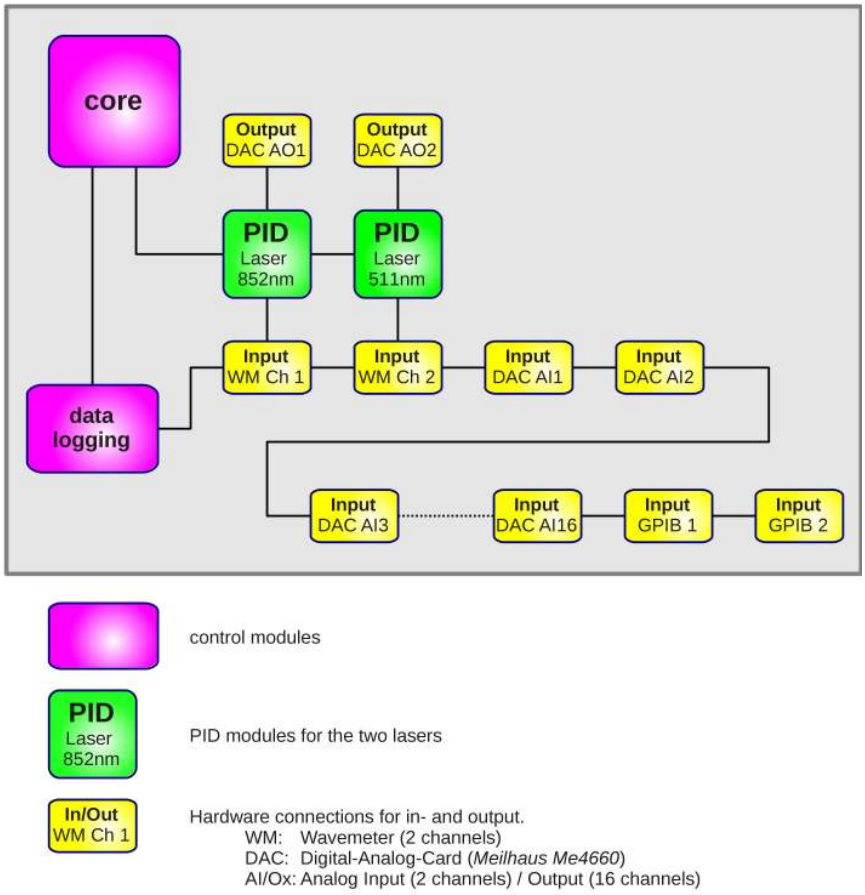

Figure 4.11: Structure of the software written to stabilize the laser frequencies and for data acquisition. For details see text.

picted in figure 4.11. A core module controls the main functions of the software like the start-up behavior and timing. The heart of the software are proportional (P), integral (I), derivative (D) controller loops. The PID controllers are separate objects. Each contains the information for a specific controller loop, like target value and gain settings. They only require external triggering which is provided by a timer from the core module. Currently, two PID modules exist, one for each laser, but the software can easily be extended. The hardware connections are again encap-

sulated in separate modules linked to the PID objects. Several different hardware components are connected to the PC. Apart from the wavemeter, a multipurpose measurement card (*Meilhaus Me4660* two analog outputs, 16 analog inputs) is used to supply the control signals to the lasers and to log information like the laser powers. Additionally, two different tabletop multimeters are connected to the PC via GPIB[1]. These are used to record data from the InGaAs photodiode and the field ionization detector (section 3.3.3). Also, TCP/IP network streams to and from the computer are implemented. All of these external connections are organized using two template classes, *input* and *output*. A template, depending on the programming language also named interface or abstract class, defines the functionality an object has to provide, independent of the actual hardware. The advantage of using templates is that the hardware connections become easily interchangeable. Each PID object requires one *input*-object, whether it receives its data from the wavemeter directly, via a network stream or any other device does not matter. The same holds true for the *output* modules. This design makes it very easy to connect new hardware, to extend the system or to use it for a different purpose.

All PID modules are set up as a linked list of objects (figure 4.11). The core module runs along this list at a set interval and triggers one control step for each PID object that is set active. The triggered PID controllers then read a datapoint from their *input* module, calculate a new error signal and send it to their *output* module. To extend the number of control loops, additional PID objects only have to be set up and appended to this list. Provided that the required hardware is connected, only a single constant has to be changed in the source code.

For data-logging, the input channels are also linked in a similar manner. At a

[1]General Purpose Interface Bus, IEEE-488

configurable interval, the software runs along the list of input modules and reads data from each active channel. This is controlled by a separate module. It can also be run on its own without the core application as a stand alone data acquisition system. The acquired data is immediately written to the computer's hard drive, so in case of a power failure only the very last data points are lost. A time stamp for each data file is automatically generated. The data logging module can perform locked scans using one of the PID controllers. For instance, it can ramp the laser frequency between two given points and record data for spectroscopy. The full functionality of the program is described in appendix A.

Chapter 5

Laser Excitation of Cesium in Magnetic fields

The laser excitation scheme used for this work is shown in figure 5.1. To tune the lasers to the right frequencies, the atomic energy levels must be known. The low lying states of cesium, $6S_{1/2}$ and $6P_{3/2}$, are well documented [129, 130] and the high n-states can be calculated from quantum defect theory [96, 134] with uncertainties of a few MHz or below.

However, the large magnetic fields of our trap strongly modify the atomic energy levels. Antiprotons and positrons are radially confined by the 1 T field of the large superconducting solenoid. To catch $\bar{H}$ atoms produced, the Ioffe trap must be energized in addition. At full current, it raises the field to 3.6 T, including inhomogenic contributions from the quadrupole and the pinch coil gradients. The first half of this chapter therefore provides a brief review of the theoretical basis of the energy levels of atoms in strong magnetic fields.

The fundamental problem for a theoretical treatment is that the radial symme-

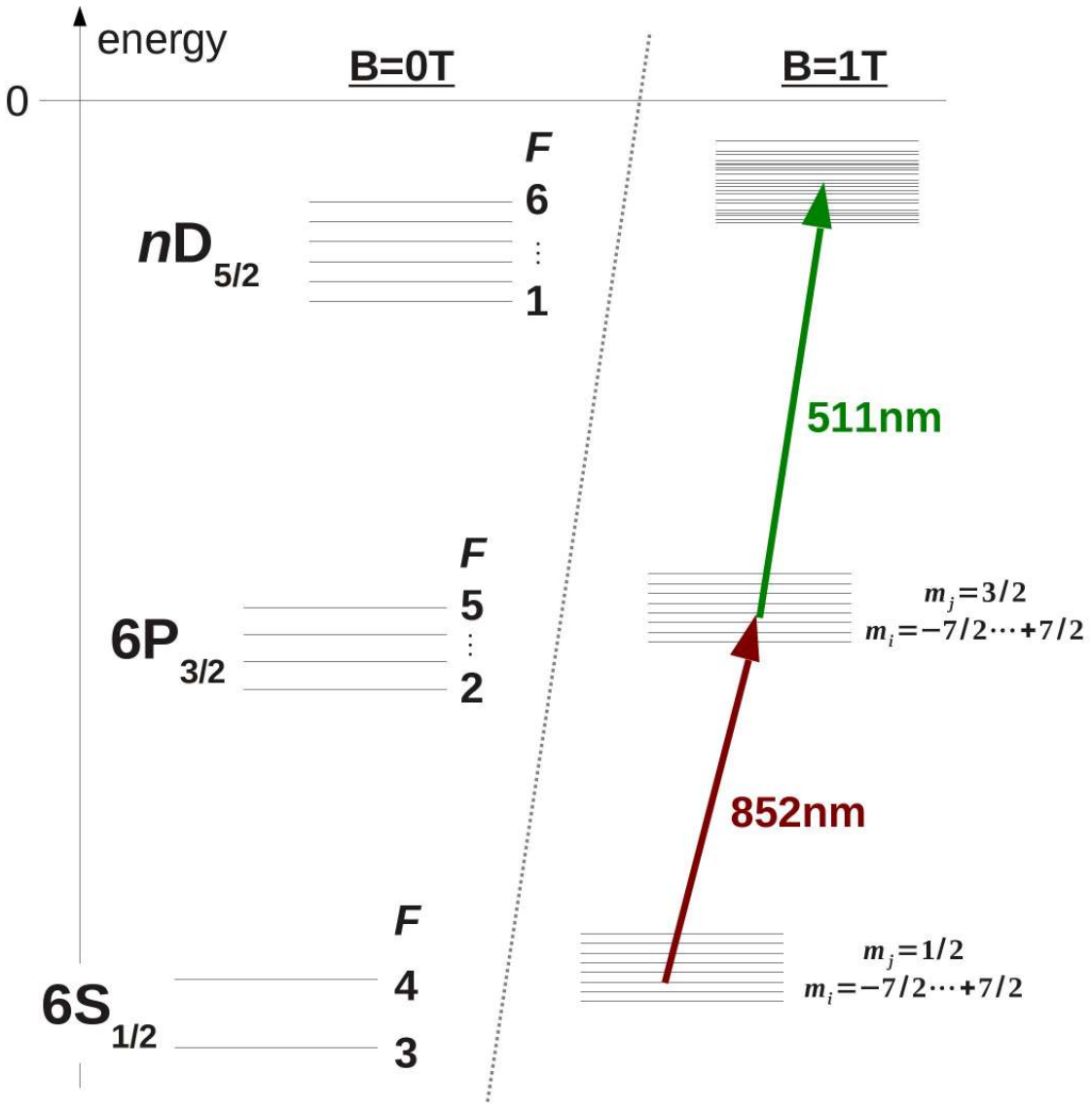

Figure 5.1: Cesium energy levels at zero field (left) and in a magnetic field of 1 T (right).

try of the atomic Coulomb potential is superimposed by a cylindrically symmetric magnetic field. The related case of atoms in electric fields can be solved analytically. When transformed to parabolic coordinates, the Hamiltonian is separable. The solution is found for instance in [69]. However, the magnetic Hamiltonian shows a

different coordinate dependence and an analogous treatment does not result in a separation of the variables. In fact, the magnetic field Hamiltonian is not separable and up to now, no complete theoretical treatment exists that provides a solution for all energy levels at arbitrary magnetic fields, not even for hydrogen.

The Hamiltonian, introduced in section 5.1.2, contains two additional terms: The paramagnetic- and the diamagnetic term. For atoms in low-lying states and typical laboratory fields, the diamagnetic term can be neglected. This regime is described in section 5.1.3. The magnetic interaction is small compared to the atomic Coulomb term and the energy levels can be calculated from perturbation theory. If the nuclear angular momentum I is zero or neglected, the result is the well known Zeeman- or, for stronger fields, Paschen-Back effect. For the case of $I \neq 0$, analytical expressions like the Breit-Rabi formula provide good estimates.

In high-n Rydberg states, the diamagnetic term must be included. It introduces off-diagonal elements in the Hamiltonian. The magnetic interaction is comparable to the energy spacing between two n-states. Perturbation theory is therefore not applicable any more. Two methods to estimate Rydberg energy levels in this regime are discussed in section 5.1.4.

These approximate solutions only consider homogeneous magnetic fields. The Ioffe trap requires a strong magnetic gradient to confine antihydrogen atoms. Our apparatus is designed to place the laser excitation region at a maximum of the quadrupole Ioffe field, thus minimizing the gradient. We assume the gradient to be small and approximate the Ioffe trap field as homogeneous.

Section 5.1.5 briefly mentions the case where the atom is dominated by the magnetic interaction. This is the case for n-states even higher than the ones considered for charge-exchange production of $\bar{H}$. The spectrum shows a series of almost equally spaced resonances that extends above the zero field ionization limit.

The second part of this chapter describes the results from two stage laser excitation of cesium atoms to various Rydberg states from $n = 37$ to $n = 50$ in magnetic fields ranging from 1 T to 3.6 T. Our calculations are in good agreement with measured frequencies, in the Penning trap field as well as in the inhomogeneous Ioffe trap field. We do, however, observe a significant broadening of each transition line as a result of the Ioffe trap's field gradient.

5.1 Theory

The topic of atoms in strong magnetic fields is of great interest in its own right. Depending on the relative strength of the field, different spectra are found ranging from small shifts of the energy levels like the Zeeman effect up to a regime where the atom is dominated by the magnetic interaction. The diamagnetic term is especially interesting. It scales with n^4B^2, n being the principal quantum number. For ground state atoms in typical laboratory fields, it can be completely neglected, but it becomes the dominant term if the atom is excited to high n-states close to the continuum. To observe the same effect in low lying states requires extremely strong magnetic fields on the order of 10^5 T. Such fields are not available in the laboratory but exist in stellar objects like neutron stars. See for instance [51, 91]. Also, the motion of electrons in solids can often be described by replacing their mass m_e by an effective mass $m'_e \ll m_e$. This increases the relative strength of the magnetic interaction compared to the Coulomb force. The spectra under such conditions can be examined using Rydberg atoms.

5.1.1 Atomic Units

For the following sections, the use of atomic units is most convenient. A summary is listed in table 5.1. Atomic units are defined by setting the electron's mass m_e, its charge e and the reduced Planck constant $\hbar$ to unity. Also, the Coulomb constant $k_e = \frac{1}{4\pi\epsilon_0} \equiv 1$. Lengths are measured in units of the Bohr radius a_0. For energy scales, the ground state energy of the hydrogen atom is used as a reference. It is equal to 1 Rydberg or $\frac{1}{2}$ Hartree. The fine-structure constant α is unitless and therefore unchanged, which then defines the speed of light to

$$c = \frac{e^2}{4\pi\,\epsilon_0\,\hbar\,\alpha} = \frac{1}{\alpha} \simeq 137\,\text{a.u}\,. \tag{5.1}$$

For the magnetic field, two conventions exist. One derived from S.I. units where the unit of the magnetic field is $2.35 \cdot 10^5$ T and one based on Gaussian units where it is $1.72 \cdot 10^3$ T. They differ by a factor of α. The same is true for quantities like the Bohr magneton which evaluates to $\mu_B = \frac{1}{2}$ if derived from S.I. units or to $\mu_B = \frac{\alpha}{2}$ if Gaussian units are used as a basis. In this work, we apply the units derived from S.I. conventions.

5.1.2 Hamiltonian

If we assume a uniform magnetic field along the $\hat{z}$-axis, $\vec{B} = B\hat{z}$, and use the Coulomb Gauge, $\vec{\nabla} \times \vec{A} = 0$, the Hamiltonian takes the form:

$$\begin{aligned} H = H_0 + \overbrace{\zeta(r)\vec{L}\cdot\vec{S}}^{H_{\text{FS}}} + \overbrace{a\left(\vec{I}\cdot\vec{J}\right)}^{H_{\text{HFS}}} \\ + \underbrace{\frac{1}{2}\alpha\left(\vec{L} + g_e\vec{S} + g_I\vec{I}\right)\cdot\vec{B}}_{H_{\text{para}}} + \underbrace{\frac{1}{8}\alpha^2\, r^2 sin^2\theta\, B^2}_{H_{\text{dia}}}\,. \end{aligned} \tag{5.2}$$

Constants		
reduced Planck constant	$\hbar$	1
electron mass	m_e	1
elementary charge	e	1
Coulomb constant	k_e	1
dielectric constant	ϵ_0	$1/4\pi$
speed of light	c	$1/\alpha = 137.035999074(44)$
Bohr magneton	μ_B	$\frac{1}{2}$ (derived from S.I.)
Units		
lengths	[L]	$1\,a_0 = 0.52917721092(17) \cdot 10^{-10}\,\mathrm{m}$
energy	[E]	$1\,\mathrm{Hartree} = 2\,\mathrm{Rydberg} = 27.21138505(60)\,\mathrm{eV}$
magnetic field	[B]	$2.350517464(52) \cdot 10^5\,\mathrm{T}$ (derived from S.I.)

Table 5.1: Fundamental constants and units relevant to this work in atomic units. The values are taken from the CODATA tables [104].

H_0 is the Hamiltonian for the free atom while H_{FS} describes the fine-structure or spin orbit coupling. The function $\zeta(r)$ encapsulates the radial dependence. H_{HFS} contains the hyperfine interaction with the hyperfine constant a. The magnetic interaction is described by two terms, the paramagnetic H_{para}, linear in B, and the diamagnetic term H_{dia}. It scales as r^2B^2 or, since the classical electron radius is proportional to n^2, $H_{\mathrm{dia}} \propto r^2B^2 \propto n^4B^2$. When evaluated between spherical harmonics, the $sin^2\theta$ term in H_{dia} introduces off-diagonal terms in the Hamiltonian with $\Delta l = \pm 2$. The magnetic field cancels the radial symmetry of the Coulomb potential and a separation Ansatz is not applicable.

Since no complete theoretical treatment exists, approximate solutions must be

used which are only correct in certain regimes. Depending on the field strengths and the state of the atom, one first has to determine which terms have a significant contribution and which can be safely neglected. The electron spin S for instance distinguishes between the normal and anomalous Zeeman regime in weak magnetic fields. At slightly larger fields however, the magnetic interaction exceeds the spin-orbit coupling and $\vec{J} = \vec{L} + \vec{S}$ is decoupled. For a calculation of the transition frequencies, the spin can now be neglected since laser light cannot change the spin state. Whether the diamagnetic term has to be considered can be estimated by taking the ratio of the magnetic terms

$$\frac{H_{\text{para}}}{H_{\text{dia}}} \propto n^4 B\,. \tag{5.3}$$

In the ground state of hydrogen, a field of $2.35 \cdot 10^5$ T is required for the diamagnetic contribution to equal the paramagnetic term. Such strong fields are not available in the laboratory, but can be found in stellar objects like neutron stars. Due to the strong n dependence, the critical field is much lower for higher states. In a 1 T field, for instance, both terms are equal at $n = 22$.

The following sections describe the theoretical treatment of atoms in magnetic fields in three different regimes. For low field strengths treated in section 5.1.3, the diamagnetic interaction can be safely neglected. The interaction of the linear magnetic term H_{para} with the orbital and nuclear angular momentum L (or J) and I results in the well known Zeeman-, Paschen-Back- and Breit-Rabi-regimes. The latter contains the first two states $6S_{1/2}$ and $6P_{3/2}$ relevant for our laser excitation scheme.

The final Rydberg states lie in a regime where the diamagnetic term must be considered and the magnetic interaction is of the same magnitude as the energy spacing between two n-states. Two approximate solutions for this regime are discussed in

section 5.1.4.

For sake of completeness, section 5.1.5 briefly mentions the case of extremely strong fields where the atom is dominated by the magnetic interaction.

5.1.3 Low Fields

In the case of weak magnetic fields well below 1 T, the diamagnetic term H_{dia} in equation (5.2) can be neglected. The simplest case is that of an atom in a singlet state ($\vec{S} = 0$). If the nuclear angular momentum is zero, or neglected due to its small size ($\vec{I} = 0$), each energy level is split into a series of $(2l + 1)$ magnetic sublevels with energy shifts

$$\Delta E = \mu_B m_l B \,. \tag{5.4}$$

These energy levels are equidistant. Due to the selection rules for optical transitions, $\Delta m_l = 0, \pm 1$, three transition lines appear in the spectrum. This behavior is found in textbooks as the normal Zeeman effect, see for instance [47].

The more common case where the atom also carries a non-vanishing spin $\vec{S} \neq 0$ is, for historical reasons, referred to as the anomalous Zeeman effect. The orbital angular momentum $\vec{L}$ and the spin $\vec{S}$ couple to the total angular momentum $\vec{J} = \vec{L} + \vec{S}$. This leads to a more complex interaction and the resulting level splitting is given by

$$\Delta E = \mu_B m_J g_J B \,, \tag{5.5}$$

with the Landé factor

$$g_J = 1 + \frac{J(J+1) + S(S+1) - L(L+1)}{2J(J+1)} \,. \tag{5.6}$$

These energy shifts are not equidistant any more, so, depending on the atomic states involved, more than three transition lines appear in the spectrum.

interaction	coefficient	value	reference
magnetic dipole	$A_{6^2S_{1/2}}$	$h \cdot 2.2981579425\,\mathrm{GHz}$	[12]
	$A_{6^2P_{1/2}}$	$h \cdot 291.9201(75)\,\mathrm{MHz}$	[114, 130]
	$A_{6^2P_{3/2}}$	$h \cdot 50.28827(23)\,\mathrm{MHz}$	[73]
electric quadrupole	$B_{6^2P_{3/2}}$	$-h \cdot 0.4934(17)\,\mathrm{MHz}$	[73]

Table 5.2: Magnetic dipole and electric quadrupole constants for the ground state and $6P_{3/2}$ states in cesium.

If the contribution from the magnetic field exceeds the spin-orbit interaction, the LS coupling is broken. Optical dipole transitions only couple to the orbital angular momentum, so the spectrum reverts back to the simpler case of the normal Zeeman effect: A uniform level splitting with three transition lines. This is referred to as the Paschen-Back regime.

Up to now, the nuclear angular momentum I has been neglected. If included as a perturbation, it cancels the uniformity of the level splitting in the Paschen Back regime. The energy levels are then given to lowest order by [124]

$$\begin{aligned} E_{|J\,m_J\,I\,m_I\rangle} &= A_{HFS}\; m_J m_I \\ &\quad + B_{HFS}\frac{3(m_J m_I)^2 + \frac{3}{2}m_J m_I - I(I+1)J(J+1)}{2J(2J-1)I(2I-1)} \\ &\quad + \mu_B(g_J m_J + g_I m_I)B\,. \end{aligned} \tag{5.7}$$

A_{HFS} and B_{HFS} are the magnetic dipole and electric quadrupole constants. Their values are listed in table 5.2.

Equation (5.7) does not reproduce the behavior in the transition region from the Zeeman to the Paschen-Back regime. A treatment in this region including the

hyperfine structure typically requires a numerical diagonalization of $H_{\mathrm{HFS}} + H_{\mathrm{para}}$. An analytical solution only exists for states where either $J = 1/2$ or $I = 1/2$:

$$E_{|J=1/2\, m_J\, I\, m_I\rangle} = -A_{HFS}\frac{I+1/2}{2(2I+1)} + g_I\mu_B(m_I \pm m_J)B \pm A_{HFS}\frac{I+1/2}{2}\left(1 + \frac{4(m_I \pm m_J)x}{2I+1} + x^2\right)^{1/2}, \tag{5.8}$$

$$\text{with } x = \frac{1}{A_{HFS}}\frac{(g_J - g_I)\mu_B B}{I+1/2}. \tag{5.9}$$

This equation is known as the Breit-Rabi formula. It is exact for fields ranging from zero up to a magnitude where the diamagnetic term has to be considered.

5.1.4 Intermediate Fields

For laboratory fields, neglecting the diamagnetic term is only valid for low lying energy states. Due to its strong n^4 dependence, H_{dia} becomes important for Rydberg states. For this work, two methods were used to calculate the binding energies of high-n-states: A direct diagonalization of the Hamiltonian and a semiclassical approximation. Both cases use hydrogen wave functions and quantum defects are included to extend the treatment to alkali metal atoms like cesium.

Matrix Diagonalization

The difficulty with treating H_{dia} is that it introduces off-diagonal matrix elements in the basis of hydrogen wave functions. Explicitly, the $sin^2\theta$ term in equation (5.2) leads to non-vanishing terms for $\Delta l = 0, \pm 2$ when evaluated between the spherical harmonics Y_l^m. This means that the magnetic field mixes all odd l-states and all even l-states, regardless of n. Due to this mixing, l is not a good quantum number any

more. In the notation of Rydberg states in high fields, l is therefore omitted in this text. A set of diagonal eigenfunctions has not been found yet, so the Hamiltonian has to be diagonalized directly. Since odd- and even-l states do not mix, only one set has to be included in the calculation. In our case, these are the even l-states since we excite from a P-level.

Three contributions have to be considered: The zero field eigenstates and the paramagnetic shift, both of which only have entries along the diagonal of the matrix, and the diamagnetic term that adds off-diagonal elements. The first term, the zero field energy levels of cesium, can be calculated by the extended Ritz formula [134]:

$$E_n = E_\infty - \frac{R}{(n-\mu_n)^2}\,, \tag{5.10}$$

$$\mu_n = A + \frac{B}{(n-A)^2} + \frac{C}{(n-A)^4} + \dots\,. \tag{5.11}$$

$E_\infty = 3.893905\,\mathrm{eV}$ is the ionization energy and $R = 13.60563631\,\mathrm{eV}$ the Rydberg constant for cesium (both from [134]). The coefficients A, B, ... contain the quantum defects for cesium. They are listed in table 5.3 for the even l-states relevant for this work. The quantum defects typically decrease with increasing l, so for $l \geq 6$ it is sufficient to set them to 0. An exception is $F(D_{5/2})$ in table 5.3, but the larger value is strongly suppressed by the power series, equation (5.11). The linear shift introduced by H_{para} is given by equation (5.5).

For the off-diagonal elements, the expectation value of H_{dia} has to be calculated in the basis of hydrogen wave functions:

$$\langle H_{\mathrm{dia}} \rangle = \frac{1}{8}\alpha^2 B^2 \,\langle n\, l\, m | r^2 sin^2\theta | n'\, l + \Delta l\, m \rangle\,, \tag{5.12}$$

where $\Delta l = 0, \pm 2$.

	S	D	G
A	4.04935665(38)	2.46631524(63)	0.00703865(70)
B	0.2377037	0.013577	−0.049252
C	0.255401	−0.37457	0.01291
D	0.00378	−2.1867	
E	0.25486	−1.5532	
F		−56.6739	

Table 5.3: Coefficients for calculating quantum defects with the extended Ritz formula (5.10). Only the values for even l states needed for this work are listed here, the rest is found in [134].

The integration of the spherical term is no challenge for standard computers today. The radial wave functions $R_{nl}(r)$ however become highly oscillatory for high numbers of n and l, which makes integration very time consuming, if possible at all. Fortunately, the radial matrix elements can be calculated by analytical formulas in a recursive way [54,83]. With all entries in the Hamiltonian set, standard algorithms can be used to diagonalize it. For this work, the tools provided by *Mathematica* and the *Gnu Scientific Library (GSL)* [1] are used.

Similar calculations were performed for instance in [140] for the states $n = 25-31$ of sodium in a 6 T field. Good agreement was found with experimental results within a resolution of $0.15\,\mathrm{cm}^{-1} \equiv 4.5\,\mathrm{GHz}$. With more powerful computers available today, we are able to perform calculations for cesium including all energy levels from $n = 10$ to $n = 60$. The source code for the calculation is found in appendix B.1.

Semiclassical Approximation

A different approach to estimate the atomic energy levels is a semi-classical approximation first introduced by Edmonds [53] and Starace [123] for hydrogen. Since the magnetic field only acts in the azimuthal plane, the z-axis is ignored and the problem is treated as two-dimensional. In the $z = 0$ plane, the issue of different symmetries of the Coulomb- and magnetic interactions does not arise. This method was later applied to Rubidium by Economou et al. [52] who found good agreement with experimental data within their resolution of $0.1\,\mathrm{cm}^{-1} \equiv 3\,\mathrm{GHz}$. Using the Bohr-Sommerfeld quantization condition, the problem can be written as:

$$\int_{\rho 1}^{\rho 2} \left(2\left(E - V_{eff}\right)\right)^{1/2} \mathrm{d}\rho = \left(n + \frac{1}{2}\right)\pi\,, \tag{5.13}$$

$$V_{eff} = \frac{1}{2}\frac{\left(m_l + \frac{1}{2}\right)^2}{\rho^2} - \frac{1}{\rho} - \alpha m_l H_0 + \frac{1}{8}\alpha^2\rho^2 {H_0}^2\,. \tag{5.14}$$

The integration runs between the classical turning points ρ_1 and ρ_2, V_{eff} is an effective potential. The calculation is again extended to cesium atoms by introducing quantum defects to n and E. A sample calculation is listed in appendix B.2.

5.1.5 Strong Fields

For extremely strong magnetic fields, or electrons excited to very high n-states, the diamagnetic term becomes dominant and the Coulomb interaction between the electron and the atomic core can be treated as a perturbation. The result is a spectrum of resonances that extends above the zero-field ionization limit. For states around E_∞, the level spacing is $\frac{3}{2}\hbar\omega_c$, with the cyclotron frequency given by equation (3.4). For states high above the ionization limit, the spacing approaches $\hbar\omega_c$, the

level spacing of a free electron in a magnetic field. The problem of a free electron in a magnetic field was first calculated by Lev Landau, therefore these states are referred to as quasi Landau levels. Example for atoms in this regime are found in [23] and [71] where the spectra of sodium and cesium were measured. The Rydberg states used for our experiments are well below this regime.

5.2 Laser excitation

The relevant cesium energy levels for this work are the ground state $6S_{1/2}$, the intermediate $6P_{3/2}$ level and Rydberg states around $n = 40$. For the two low-lying levels, the diamagnetic term can be neglected. The ground state has $J = \frac{1}{2}$ so its energy can be calculated with the Breit-Rabi formula (5.8). For the $6P_{3/2}$ state equation (5.7) is valid for fields larger than 20 mT. For the high-n states, both methods described in section 5.1.4 are applied.

5.2.1 First Transition

Without a magnetic field, the transition $6S_{1/2} \rightarrow 6P_{3/2}$ consists of two groups of three hyperfine transitions each (compare figures 4.1 and 4.4). Cesium has a nuclear angular momentum of $I_{Cs} = 7/2$ so each ground state has eight degenerate sublevels corresponding to $m_I = -7/2, -5/2, \ldots, 7/2$. In a magnetic field, this degeneracy is canceled. The value of m_I cannot be changed by laser light, therefore each of the six zero-field hyperfine transition splits up into eight magnetic sublines. They are separated by about 1 GHz. This spacing is not uniform and it slowly increases with higher magnetic fields. The calculated transition frequencies in dependence of the magnetic field are plotted in figure 5.2. Only one m_I state can be addressed with a

narrow linewidth laser which leads to a signal reduction to 1/8.

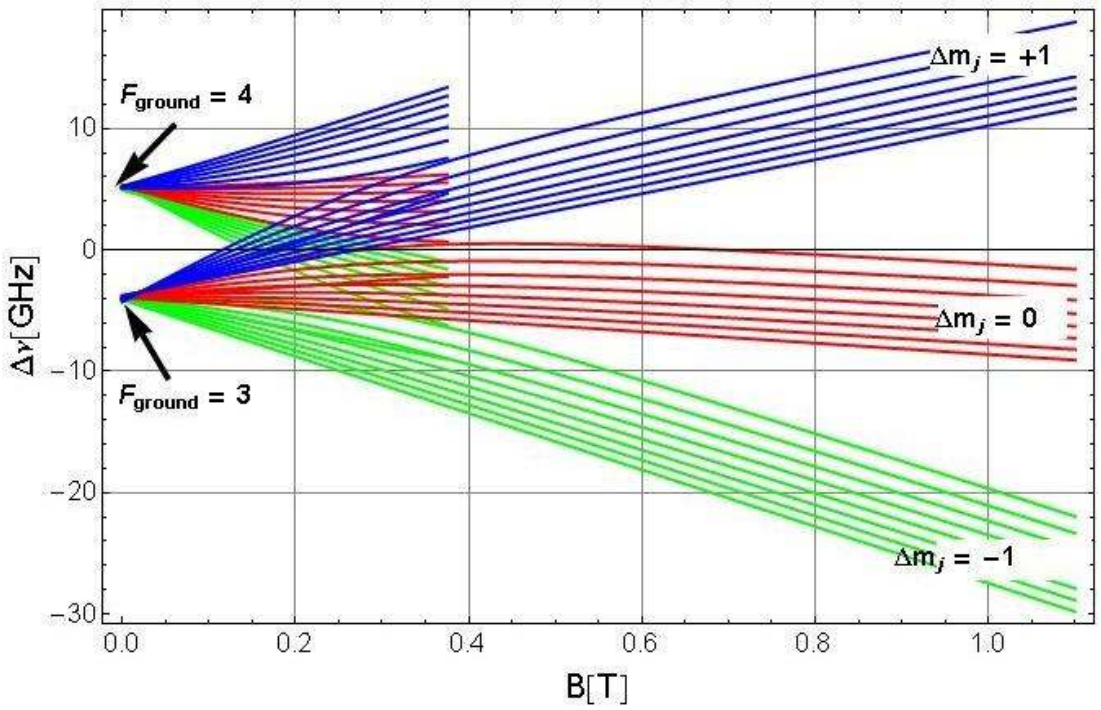

Figure 5.2: Transition frequencies of the cesium D_2 line in a magnetic field. The y-axis zero corresponds to the line-center at 351.7257185 THz [129].

Although a total of 64 transitions exist, only two groups are closed-cycle and can be used without rapidly depopulating the initial ground state. In the basis of $|J, m_J\rangle$, they are:

$$\left|\frac{1}{2}, -\frac{1}{2}\right\rangle \rightarrow \left|\frac{3}{2}, -\frac{3}{2}\right\rangle , \tag{5.15}$$

$$\left|\frac{1}{2}, +\frac{1}{2}\right\rangle \rightarrow \left|\frac{3}{2}, +\frac{3}{2}\right\rangle , \tag{5.16}$$

with m_I unchanged from initial to final state.

Figure 5.3 shows frequency scans over the group corresponding to the positive sign (5.16) at different magnetic fields. The plots show the fluorescence signal

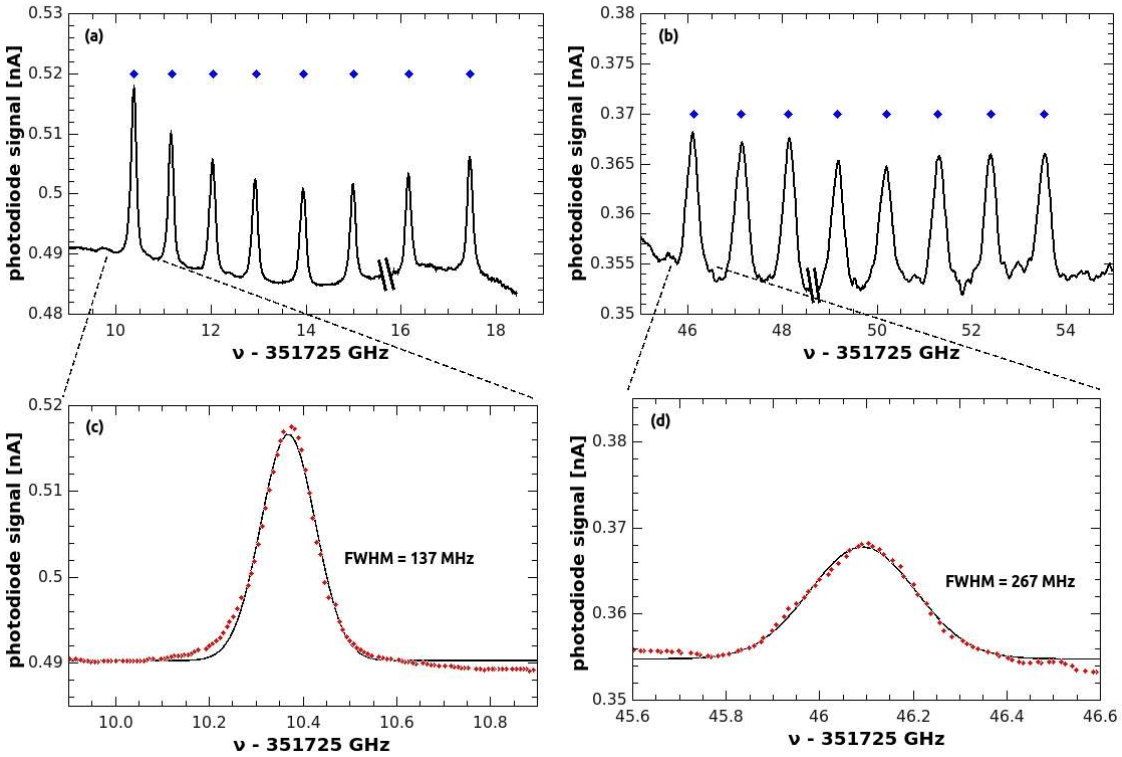

Figure 5.3: Fluorescence signal recorded from the group of closed cycle transitions $|J = 1/2, m_J = +1/2\rangle \rightarrow |J' = 3/2, m_J{}' = +3/2\rangle$ in a magnetic field of 1 T (a) and a superimposed Ioffe field of 3.6 T (b). The group corresponds to the blue lines from $F_{ground} = 3$ in figure 5.2. The diamonds show the calculated transition frequencies using equations (5.7) and (5.8). The double slashes indicate where the laser had to be retuned to cover the entire group. The background signal is caused by scattered light from the laser. Figures (c) and (d) show a magnified view of the first peak for both fields. The broadening of the line in the inhomogenic Ioffe field is clearly visible. The FWHM from a Gaussian fit (solid line) is twice as large in the second case. The x and y axis in figures (c) and (d) span over the same range for better comparison.

recorded with the InGaAs photodiode (figure 3.11). Subfigure 5.3(a) is in the 1 T field of our Penning trap and (b) with the Ioffe trap energized in addition generating a total field of 3.6 T. The inhomogeneous component of the quadrupole field causes a broadening of the transition lines in the second case. This can be clearly seen in the magnified views (c) and (d), which show a single peak from each manifold. For these low lying states, no discrepancy in the transition frequency between calculation and measurement is observed. Therefore such scans can also be used to determine the strength of the magnetic field with an accuracy of about 1 mT ($\equiv 10^{-3}$). Measuring the magnetic field via cyclotron resonances of charged particles typically provides better accuracy, but the necessary amplifiers were not always installed in the apparatus.

5.2.2 Second Transition

To estimate the energy levels of the Rydberg states, we used both methods described in section 5.1.4. Earlier experiments used lasers with spectral resolutions of several GHz [52], 10^3 higher than our system, or focussed on the quasi Landau regime [71].

Figure 5.4 shows the deviation of calculated from measured frequencies $\Delta\nu = \nu_{calc} - \nu_{meas}$ for a number of cesium Rydberg states between $n = 37$ and $n = 50$ in a 1 T field. The energy levels range from about 2.7 THz ($n = 37$) to 1.2 THz ($n = 50$) below the zero-field ionization limit (941.5 THz). For most states, both methods yield good results with an uncertainty of 5 GHz or below. The matrix diagonalization seems better suited to the lower n-states. The offset for the $n = 37$ state is significantly smaller than the one obtained from the semiclassical method. For $n = 50$ however, diagonalization of the Hamiltonian results in an error of almost 90 GHz, presumably because not enough zero-field states were included in the cal-

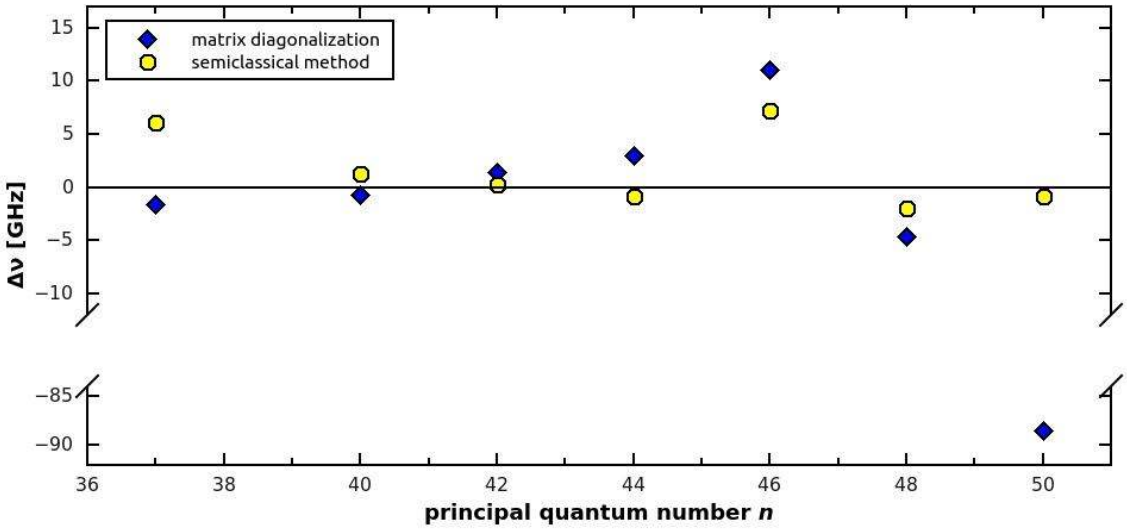

Figure 5.4: Deviation of the frequencies calculated by the two methods described in section 5.1.4 from experimental data $\Delta\nu = \nu_{calc} - \nu_{meas}$ for a number of Rydberg states in a 1 T field.

culation. Adding additional states would greatly increase the computational time required. On the other hand, the semiclassical method yields accurate estimates in this regime and the complexity of the calculation does not increase for higher n states. Why the deviation for the $n = 46$ state is slightly larger than for the surrounding states is not clear.

Using one of the two methods, we were able to calculate the energy levels and therefore the transition frequencies with an uncertainty of a few GHz for various states in the magnetic fields of our Penning-trap. In the much higher field of the Ioffe trap, too many states have to be included for a direct matrix diagonalization. Therefore we can only use the semiclassical method in this case. However, the uncertainty is still in the range of only a few GHz. Since this is well within the tuning range of our 511 nm laser, we can easily find the transition frequencies once they are calculated.

Two of the resonances are shown in figure 5.5: The transitions to the $n = 42$ state in a 1 T field (a) and to the $n = 38$ state in a field of 3.1 T. This corresponds to the Ioffe trap ramped up to 80 % of its maximum current. These are the states primarily used for our experiments. The signal recorded is the field ionization current with a stripping field of 300 V/cm applied (section 3.3.3) while the frequency of the green laser is swept across resonance. Similar to the first transition, a line broadening is observed in the Ioffe field, but in this case even more pronounced. Figures (c) and (d) show the field ionization current when sweeping the amplitude of the electric field from −300 V/cm to +300 V/cm while the lasers are locked to the resonance frequencies. Depending on the direction of the electric field applied, we collect either negative electrons or positive cesium ions. The states are the same as in figures (a) and (b). An amplitude of 300 V/cm is sufficient to ionize all Rydberg atoms. Ionization starts around an amplitude of 100 V/cm. This sets a limit to the acceptable magnitude of stray fields. To avoid Stark-ionization of Rydberg cesium, positronium or antihydrogen, the amplitudes of all fields within the electrode stack must be kept well below this value.

The curves (c) and (d) show a small offset at zero electric field. We seem to collect some positive cesium ions while the lighter electrons escape. We took great care not to expose any dielectric materials to the cesium beam and to ground all conducting components to prevent the build-up of electric charges that could ionize Rydberg atoms. Instead, this effect may originate from an imperfect collimation of the cesium beam or a slight misalignment of the field-ionization components. If Cs^* atoms hit an edge of one of the plates, they may ionize on collision. This should lead to a deposition of cesium on the plate, however in very small quantities. Actually no deposition of cesium is noticeable behind the first collimation baffle (figure 3.11), so this hypothesis cannot be tested without a much more detailed examination.

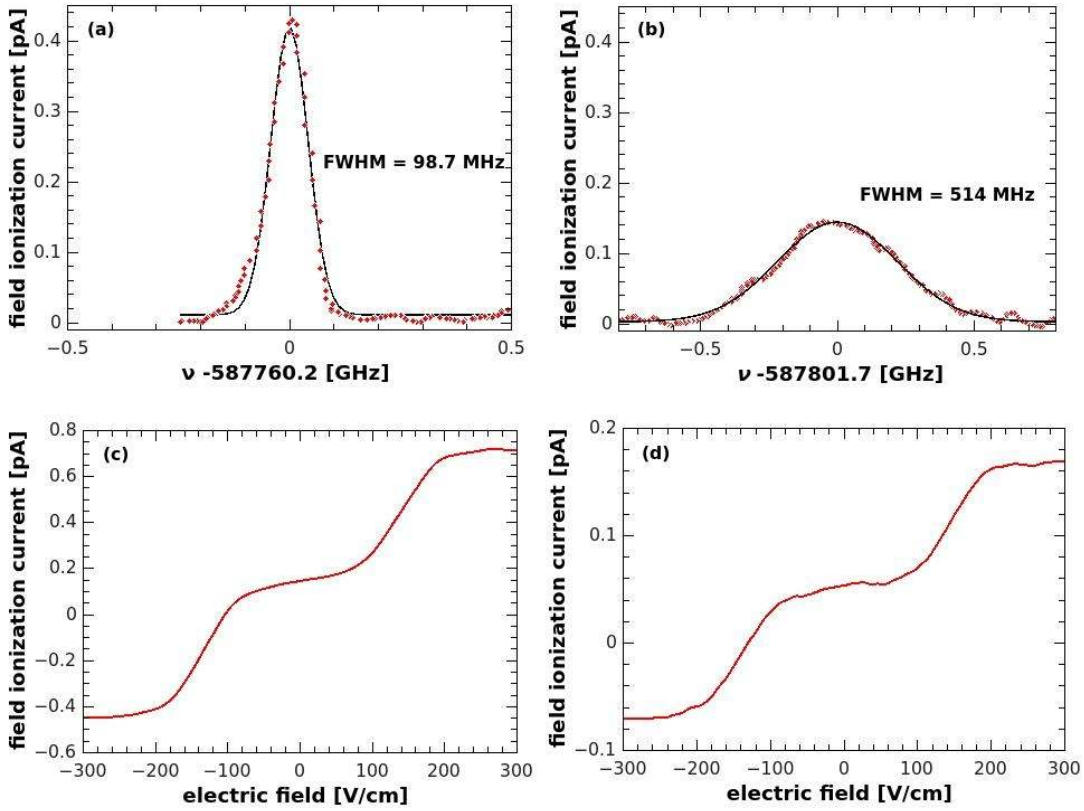

Figure 5.5: Field ionization current recorded from stripping cesium atoms laser excitated to Rydberg states. The magnetic fields are the homogeneous 1 T field from the large solenoid (left coloumn, (a, c)) and a Ioffe trap field of 3.1 T (right column, (b, d)). Without a magnetic field, the states would correspond to $42D_{5/2}$ (left) and $38D_{5/2}$ (right), respectively. Figures (a) and (b) show frequency scans of the green laser. The red diamonds are data points while the solid line is a Gaussian fit to determine the widths of the peaks. As for the first transition, figure 5.3, the line is broadened in the inhomogeneous Ioffe field. Figures (c) and (d) show sweeps of the electric field applied to ionize the Rydberg atoms with the lasers locked to resonance. Ionization starts around a field amplitude of 100 V/cm and 300 V/cm is sufficient to ionize all excited atoms.

Similar data obtained with the copper vapor laser is found in [122] where a maximum ion current of 40 fA was measured from the $n = 37$ state in a uniform 4.9 T magnetic field. With our new laser system, we achieve a value 15 times higher in our Penning trap field, figure 5.5(a), and three times higher in the Ioffe field (b). However, the influence of the magnetic field should be noted. A larger field causes stronger mixing of different l states which reduces the contribution of the S and D orbitals to the final magnetic field state. Therefore the excitation efficiency decreases and the factor of 15 from figure 5.5(a) would be somewhat reduced in a stronger field. On the other hand, the inhomogeneous quadrupole field of our Ioffe trap causes additional broadening of the transition lines, so in a homogeneous field of similar magnitude we would observe a stronger signal than in figure 5.5(b). Also, the observed ion current depends on the amount of ground state cesium crossing the laser beams.

The laser powers typically used for an experiment are 5 mW from the infrared and 175 mW from the green laser. We achieve an incoupling efficiency into the fiber of 75 % for both lasers simultaneously. The fiber feedthrough into the Penning trap and several optical elements within the apparatus cause further losses so that about 55 % of the initial power is available for laser excitation in the trap. At the excitation region, the lasers are collimated to a beam of 1.5 mm diameter.

The first transition to the $6P_{3/2}$ state is easily saturated by the 5 mW emitted from the infrared laser. The expected excitation efficiency to Rydberg states can be calculated by a rate equation model using the parameters above and the cesium oscillator strengths [92]. Such a calculation was performed in [81] for the previous excitation scheme using the pulsed copper vapor laser. The result was an expected excitation efficiency of close to 24 % with the full power of the copper vapor laser. The output power had to be restricted to 15 % to limit the heat load on the cryo-

genic system. This reduces the expected efficiency to about 11 %. Adapting the computation to our new laser system gives an efficiency of 48 % for the $n = 42$ state. This value is four times higher and comes very close to saturation. It should be noted that the calculations neglect the effect of the magnetic field which mixes different l-states and thus reduces the excitation efficiency. This is discussed in more detail in section 6.2. However, the power available from our new laser may partly compensate for this effect. If, for instance, the l-mixed Rydberg states retains $\frac{1}{3}$ of its D character, the excitation efficiency is still as high as 44 %.

From the manufacturer's datasheet, we expect a stream on the order of $\simeq 10^{12}$ ground state cesium atoms per second from the alkali metal dispenser. About $3{\cdot}10^8$/s should pass the collimation baffles and reach the field ionization plates (figure 3.11). The average field ionization current of 600 fA from figure 5.5(c) corresponds to $4 \cdot 10^6$ Rydberg cesium atoms per second. We can only excite one of the 16 magnetic field ground states and some Rydberg atoms decay during the flight from the laser excitation region to the field ionization plates. Considering these factors gives an excitation efficiency of 33 %. While this number comes close to the value calculated above, it should be taken with care. The datasheet only provides values from a room temperature environment while our measurements were done with the apparatus cooled to 4 K and the exact output characteristic of the source is not known.

Due to the higher oscillator strength, laser excitation to the $37D$ state should be more efficient than to the $42D$ state. This is in clear disagreement with the data from figure 5.5(d) which corresponds to 7 % excitation efficiency. The difference is due to the almost four times larger magnetic field which has a much stronger effect on the energy levels. Especially the l-mixing is important since it drastically reduces the effective dipole matrix element of the final state.

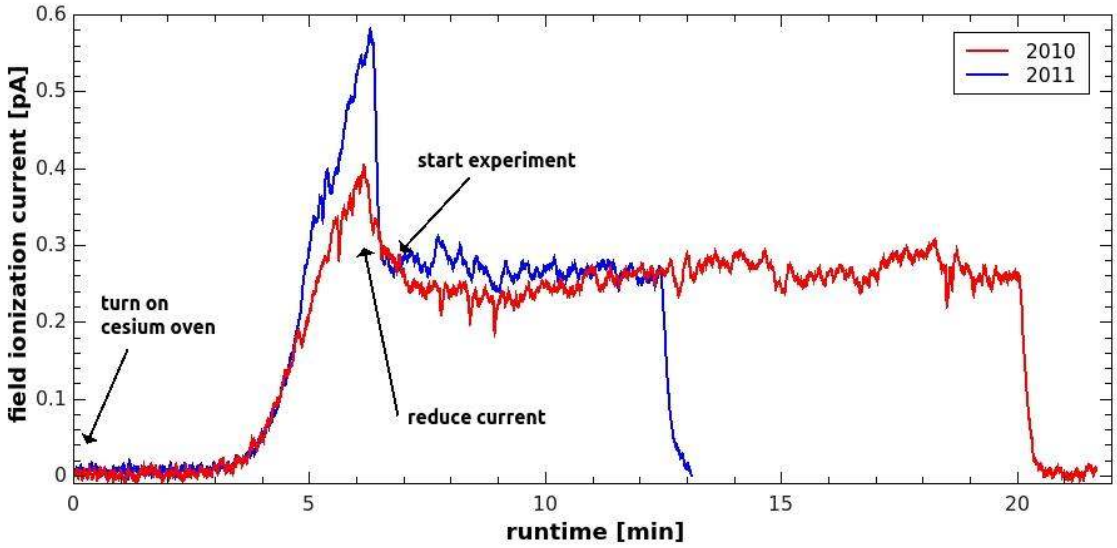

Figure 5.6: Pre-heating cycle to provide a steady stream of Rydberg atoms. After a warm up time of 360 s, the current through the cesium oven is reduced. Another 30 s later, the flux of cesium atoms has reached a steady value. At this point, the lasers are unblocked, marking the start of an experiment.

These calculations and measurements show that our new laser system provides a significantly higher excitation efficiency than the copper vapor laser. Due to this improvement, we achieve a larger stream of Rydberg atoms at a much lower usage of cesium. This reduces the heat load on the cryogenic system and the deposit of cesium on the collimation baffles. In combination with the larger cesium sources, our new laser system allows operation of the trap for an entire AD beam run of several months without the need to warm up the apparatus and break vacuum to exchange the cesium source.

The source requires several minutes to reach an equilibrium temperature. During this time, the output of *Cs* is slowly increasing towards a steady state value. To reduce the waiting time until a constant flux of cesium atoms is reached, the source

is pre-heated for each experiment. Figure 5.6 shows the field ionization signal for such a pre-heating cycle. Usually the green laser is blocked during the warm up to achieve well-defined starting points for each run. The pre-heating current is chosen $0.25 - 0.3\,\mathrm{A}$ higher than the steady state value of $4.2 - 4.8\,\mathrm{A}$. After $360\,\mathrm{s}$ warm-up time, the current is reduced and another $30\,\mathrm{s}$ later, the flux of Rydberg cesium atoms has reached a constant level. At this point, the green laser is unblocked marking the start of an experiment. Once the oven is turned off, the stream of cesium atoms stops almost instantly. The figure shows two curves, one for the 2010 beam run and one from the 2011 beam run. The current through the cesium oven differs by about $0.25\,\mathrm{A}$ in the two cases, but we are able to reproduce an identical flux of Rydberg cesium atoms from one year to another.

Chapter 6

Charge-Exchange Experiments

Chapters 3 and 4 described the ATRAP apparatus and the laser system. Laser excitation of cesium atoms to high n Rydberg states in strong magnetic fields was the subject of chapter 5. So with the tools and methods covered, this chapter contains our charge-exchange experiments. It starts in section 6.1 with a brief description of the required techniques to load and measure the large antimatter plasmas we use for these experiments.

Chapter 5 showed laser excitation to various high-n states, however it is not obvious which of these states is most suited for charge-exchange production of antihydrogen. Our new tunable laser allows selection of an optimized Rydberg state and the necessary considerations are subject of section 6.2.

With all the prerequisites attended to, section 6.3 describes experiments to investigate the first charge-exchange reaction, the production of positronium. The final step, charge-exchange production of antihydrogen, is discussed in section 6.4.

6.1 Particle Loading and Counting

Section 3.1 described our sources for charged antimatter particles, CERN's Antiproton Decelerator and the York positron accumulator. They eject bunches of antiprotons and positrons about every 100 s and 30 s, respectively. The following section describes how these bunches are caught in our Penning trap. Multiple shots are accumulated to load large plasmas of several 10^6 antiprotons and up to $4 \cdot 10^9$ positrons. In addition to antimatter particles, electrons are used for diagnostics and cooling of antiprotons and positrons. They are liberated by photo-emission from UV laser pulses within the trap. The final part of this sections attends to the two methods used to count the number of particles in our plasmas.

6.1.1 Electrons

Although our experiments are conducted with antimatter particles, electrons are required for two reasons: They are available in greater numbers, at higher rates and at much less cost per particle than positrons or antiprotons. So many of the techniques to be used with antimatter particles are first tested with electrons.

Electrons are also essential to cool antiprotons. The 5.3 MeV $\bar{p}$ arriving from the AD are slowed down by a gas-filled tuning cell and the degrader foil (section 3.3.1) to energies of a few keV. The electrode *HV* and the degrader *DEG* can both be biased to −5 kV, so they can confine keV $\bar{p}$ in the Penning trap. However, this energy is still far too high for production of cold antihydrogen atoms which requires antiprotons with energies below 1 meV.

Charged particles circulating in a magnetic field constantly cool by synchrotron radiation. The energy radiated by an accelerated charged particle is given by the

Larmor formula ([98], chapter 11):

$$\frac{dE}{dt} = -\frac{q^2}{6\pi\,\epsilon_0\,c^3}\,|\ddot{\vec{r}}|^2\,. \tag{6.1}$$

In a magnetic field, a charged particle is subject to the Lorentz force

$$\vec{F}_L = m\ddot{\vec{r}} = q\dot{\vec{r}} \times \vec{B}\,. \tag{6.2}$$

Substituting equation (6.2) into (6.1) with $\dot{\vec{r}} = v_\phi\hat{\phi}$ and the cyclotron energy $E = \frac{1}{2}mv_\phi^2$ leads to:

$$\frac{dE}{dt} = -\frac{E}{\tau_D}\,. \tag{6.3}$$

The solution to equation (6.3) is a simple exponential decay of the form

$$E(t) = E_0 e^{-t/\tau_D}\,, \tag{6.4}$$

with the damping time

$$\tau_D = \frac{3\pi\epsilon_0 c^3 m^3}{q^4 B^2}\,. \tag{6.5}$$

The magnetic field in the antiproton catching region is locally raised by a field-boosting solenoid to 3.7 T. The dampening time (6.5) for an antiproton in this field is $\tau_D(\bar{p}) = 1.2 \cdot 10^9\,\mathrm{s} \simeq 37\,\mathrm{years}$. So on their own account, the $\bar{p}$ will need far too long to cool. The time constant for the energy loss from synchrotron radiation scales with m^3, so an electron cools by a factor $1836^3 = 6.2 \cdot 10^9$ times faster which gives $\tau_D(e^-) = 0.19\,\mathrm{s}$. Since e^- and $\bar{p}$ have identical charge, they can be confined in the same potential well. The antiprotons transfer energy to the electrons by collisions, which then quickly loose it via synchrotron radiation. The antiprotons thermalize with the electrons on a fast time scale, so the time constant for electron cooling is dominated by the time it takes the electrons to radiate energy. Electron cooling

is a vital technique to obtain cold antiprotons. It is discussed in [117] and was first demonstrated in [61]. It is now widely used, also in combination with other techniques like adiabatic cooling [64]. In a similar manner, a cloud of electrons can also be used to increase the cooling rate of positrons during loading and stacking (section 6.1.2).

Electrons are liberated from the Be degrader foil at the bottom of the Penning trap by photo emission from UV laser pulses [95]. The laser light is generated by a KrF excimer laser *(GAM Lasers EX5)*. It emits pulses of 10 ns duration with energies of 20 mJ and a wavelength of 248 nm. Its maximum repetition rate is 1 kHz, but for electron loading it is operated at a much lower rate of 1 Hz to allow trapping and cooling of electrons between subsequent pulses. The laser is located near the top hat of the Penning-Ioffe trap, outside of the vacuum space (figure 3.8). Four mirrors allow alignment of the beam which then enters the apparatus through a window in a room-temperature section above the top-hat. Inside the vacuum space, it is directed downward along the trap axis by a 45 ° mirror. Because positrons are also loaded along the same path, the mirror is mounted on a motorized stage which is retracted for e^+ loading. The laser pulses travel downwards for a distance of more than 2 m before they hit the Be degrader foil. The work function of vacuum deposited beryllium is 5.08 eV, slightly higher than the energy of the UV photons of $E = hc/\lambda = 5\,\mathrm{eV}$. However, once beryllium has been exposed to oxygen, its work function reduces to 3.6 eV, which enables the UV photons to liberate photo electrons from the degrader foil [44].

To catch the e^-, the potential structure shown in figure 6.1 is applied to the electrodes in the lower stack. The electrons are accelerated away from the degrader by a positive voltage applied to the *TUBE* electrode. The potential barrier on *LBE1* is pulsed up shortly after the excimer laser fires, allowing electrons to pass.

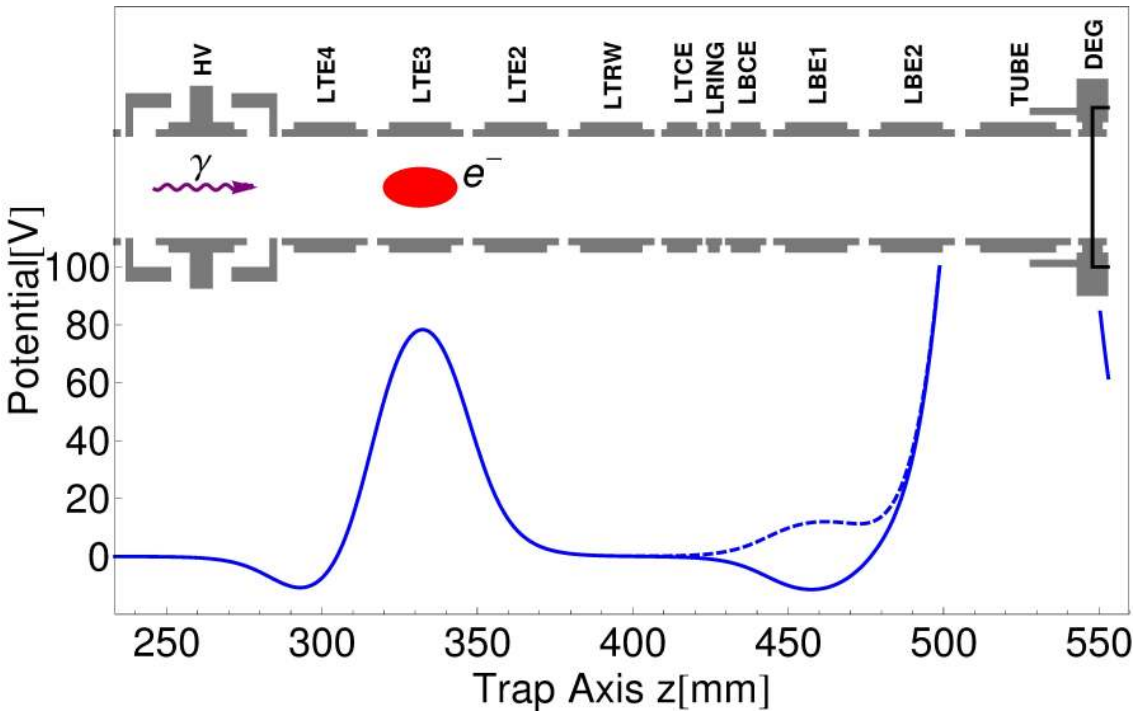

Figure 6.1: Accumulation of electrons: The e^- are liberated from the degrader foil by UV photons from an excimer laser. The potential well on *LBE1* is pulsed up (dashed line), allowing the e^- to enter the potential structure between electrodes *LTE4* and *LBE1*. Once trapped between the two electrodes, they lose energy by synchrotron radiation and cool into the well on *LTE3* before the next laser pulse arrives.

Once the barrier is restored, the e^- are trapped between the electrodes *LTE4* and *LBE1*. They quickly lose energy by synchrotron radiation and cool into the 80 V deep well on *LTE3*. The excimer laser is fired once per second. By this time, the electrons are deeply confined within the well so that they cannot escape when the barrier is pulsed up again to let the next bunch in. In this manner, large numbers of electrons from subsequent laser pulses are accumulated. On average, several 10^8 e^- are loaded within 30 s. When the electrons fall into a deep potential well, they gain kinetic energy which they have to radiate away again. To reduce the cooling

time, the well depth on *LTE3* is initially set to 1 V and after each laser pulse, it is increased by 1 V.

6.1.2 Positrons

Bunches of 10^7 positrons are ejected from the positron accumulator three times per AD cycle or about every 30 s (see section 3.1.2). They are guided into our Penning trap via a several meter long transfer line shown in figure 3.1. The transfer line and steering of the e^+ is described in detail in [33]. The positron bunches are caught and accumulated in the Penning trap using the long catching well depicted in figure 6.2. On arrival of a e^+ bunch, the potential barrier on electrode *UTE1* is pulsed down to let the e^+ enter (dashed line in figure 6.2). The barrier is restored before any of the e^+ reflected from *UBR4* can leave again. The positrons are ejected from the accumulator with a pulse of 63 V. They lose most of their kinetic energy by climbing the 58 V potential plateau between *UTR15* and *UBR2*. To shorten the e^+ cooling time, electrons are pre-loaded and stored in a nested well potential centered on *UTR8*. The positrons lose energy by subsequent collisions with the e^- and cool into one of the deep wells on *UTR7* and *UTRW* before the next bunch of e^+ arrives. Since the interaction time with the electrons is short and the positrons cool into separate wells, losses from annihilation are negligible. Up to $2 \cdot 10^8$ positrons are loaded before the trapping efficiency decreases. At this point, the electrons are ejected by lowering the voltage on electrode *UTR8*. This merges the two positron wells. Since the e^+ have cooled to the bottom of their wells, no losses are observed at this stage.

The positron cloud is then compressed to a radius of 2 mm by a rotating wall drive (section 3.2.3) applied to the segmented electrode *UTRW*. The plasma is now

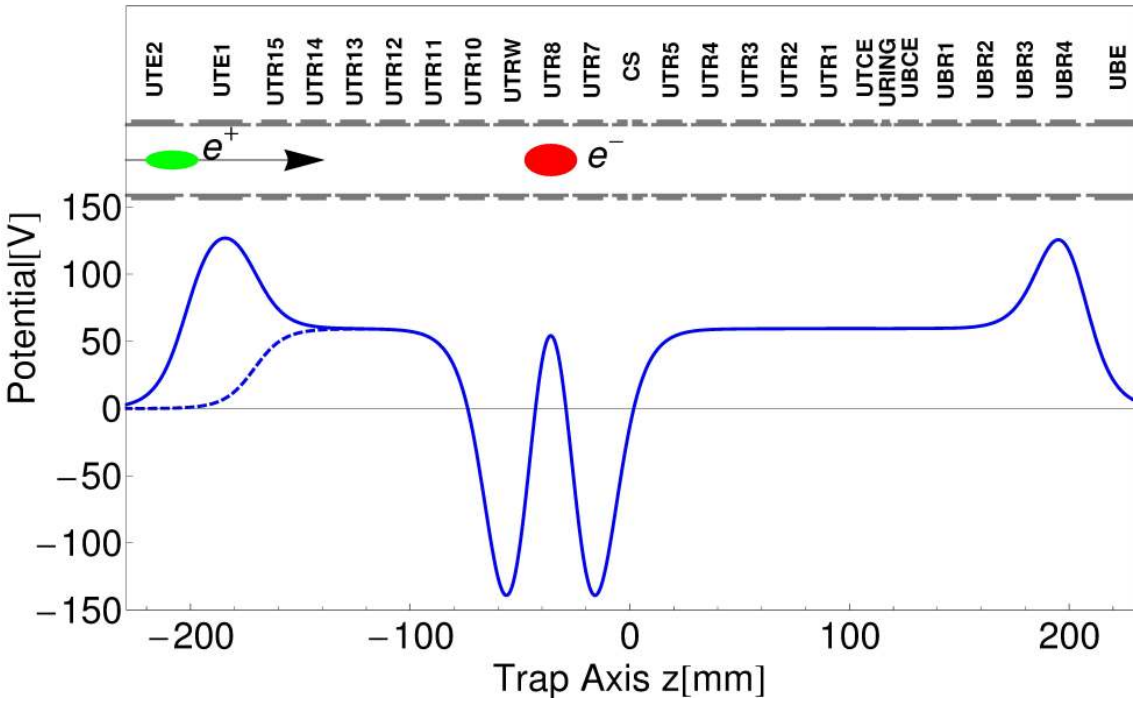

Figure 6.2: Potential structure for loading positrons. On arrival of a e^+ bunch, the barrier on electrode *UTE1* is pulsed down (dashed line). The e^+ lose energy by climbing the potential plateau and by collisions with pre-loaded electrons. By periodic application of a rotating wall drive, accumulation of up to $4 \cdot 10^9$ positrons is possible, many more than needed for our experiments.

either used for experiments or to cool additional bunches of positrons to accumulate even larger numbers. By applying a rotating wall drive every half hour to counteract plasma expansion, up to $4 \cdot 10^9$ positrons are loaded. This number is much larger than needed for any of our experiments. For charge-exchange production of $\bar{H}$, we typically use $3 \cdot 10^8$ e^+ per trial. Unlike previous experiments [122], we are therefore not limited by the number of positrons available.

6.1.3 Antiprotons

The antiprotons enter the Penning trap with an energy of 5.3 MeV, 10^5 times more than the positrons. This requires a multi-stage process for $\bar{p}$ loading, starting with steering of the incident beam into the trap and reducing the $\bar{p}$ energy by three orders of magnitude. Inside the trap, the antiprotons are caught in a high-voltage potential well and rapidly cooled by collisions with a preloaded electron plasma. After $\bar{p}$ loading, the e^- must be ejected since they would strongly interfere with antihydrogen experiments. The catching efficiency is greatly enhanced by the field boosting solenoid that increases the magnetic field in the trapping region during $\bar{p}$ loading. To prevent losses from plasma expansion, a rotating wall drive compresses the radius of the $\bar{p}$ cloud before the field boosting solenoid is ramped down again.

Beam Steering

Antiprotons are ejected from CERN's AD in bunches of $3 \cdot 10^7$ once every ~ 100 s. They are sent through a beam line along the floor of the AD hall and bent upwards into the Penning trap by steering magnets (see figure 3.1). For efficient catching, the $\bar{p}$ must enter the trap on axis. Hysteresis effects in the room temperature electro-magnets and the numerous magnetic fields from several experiments in the AD hall require fine tuning of the currents through the steering magnets at the beginning of each beam shift. Two detectors located underneath the Penning trap allow measurement of the incident beam's trajectory. The antiprotons first pass through a segmented silicon detector located $\simeq 1$ m below the trap. The beam is centered on this detector by tuning the currents through the steering magnets. The silicon detector is mounted on a rotatable cube. Turning it by 90° moves the detector out of the path of the beam and lets the $\bar{p}$ pass into the trap through an

aperture. The silicon detector is used for rough steering of the antiproton beam.

For fine tuning, a parallel plate avalanche counter (PPAC) is installed just below the bottom of the Penning trap. It consists of two anodes and a common cathode oriented in the plane perpendicular to the beam. Each anode has five 2 mm wide strips of aluminum foil evaporated on Mylar. They are separated by 0.5 mm. The cathode is made of aluminized mylar foil. The strips of the two anodes are oriented in right angle, so that one serves as diagnostic for the x and the other one for the y direction. The space between the anodes and cathodes is filled with argon gas at atmospheric pressure. Antiprotons passing through the cell ionize gas atoms. The liberated electrons are accelerated towards the anodes by voltages of 150 V applied to the strips. The device is operated in linear mode so that the charge collected from each strip is proportional to the number of $\bar{p}$ that have passed through it. The PPAC detector allows reliable fine tuning of the beam position to achieve repeatable antiproton catching conditions for each beam shift.

Reduction of Beam Energy

The AD decelerates the antiprotons by three orders of magnitude from 3.6 GeV down to an energy of 5.3 MeV. This is still too high to trap them with electrostatic potentials, so further reduction of their energy is required. For this purpose, a beryllium degrader foil and a gas filled energy tuning cell are installed in the beam path. The two 10 μm thick titanium foils that separate the Penning trap's vacuum space from that of the AD and the thin mylar foils of the PPAC also slow the antiprotons, but most of the $\bar{p}$ energy is deposited in the 100 μm thick Be degrader. The gas tuning cell installed between the PPAC and the degrader allows active control of the $\bar{p}$ energy loss. It is filled with a variable mixture of He and SF_6. A

larger fraction of SF_6 corresponds to a higher energy loss. Under typical operation condition of the AD, the $\bar{p}$ catching efficiency is highest with a gas mixture of (by number) 80 % He and 20 % SF_6. Only about 0.5 % of the antiprotons passing through the gas cell and the foils emerge with an energy low enough to be caught by the 5 keV potential barriers in the Penning trap.

Installation of the new ELENA ring will significantly improve this situation [108]. ELENA will further decelerate the $\bar{p}$ down to 100 keV so that the thickness of the degrader foil can be reduced, improving the trapping efficiency by at least an order of magnitude. Right now, we need about an hour of beam time to accumulate the several 10^6 antiprotons we need per experiment. With a higher trapping efficiency, this time will be much shorter.

Catching and Accumulation

Trapping and accumulating antiprotons is done in a similar manner as positron loading. The signs of the potentials must be inverted and larger amplitudes of the confining barriers are required to catch the antiprotons that still arrive with energies of several keV. For this purpose, two electrodes, *HV* and the degrader foil *DEG*, can be biased to −5 keV. As mentioned in section 6.1.1, antiprotons require a very long time to lose energy by synchrotron radiation. Therefore cooling with electrons is essential. About 10^8 e^- are pre-loaded, spun up to a radius of 6 mm and placed into the potential structure shown in figure 6.3. When a $\bar{p}$ shot arrives from the AD, the potential barrier on the degrader foil *DEG* is raised from −5000 V up to +600 V (dashed line) to let the $\bar{p}$ in. The barrier is restored to its negative value 300 ns after the $\bar{p}$ are ejected from the AD. This prevents the antiprotons reflected from the second barrier on *HV* to escape again. Once confined, the $\bar{p}$ lose energy

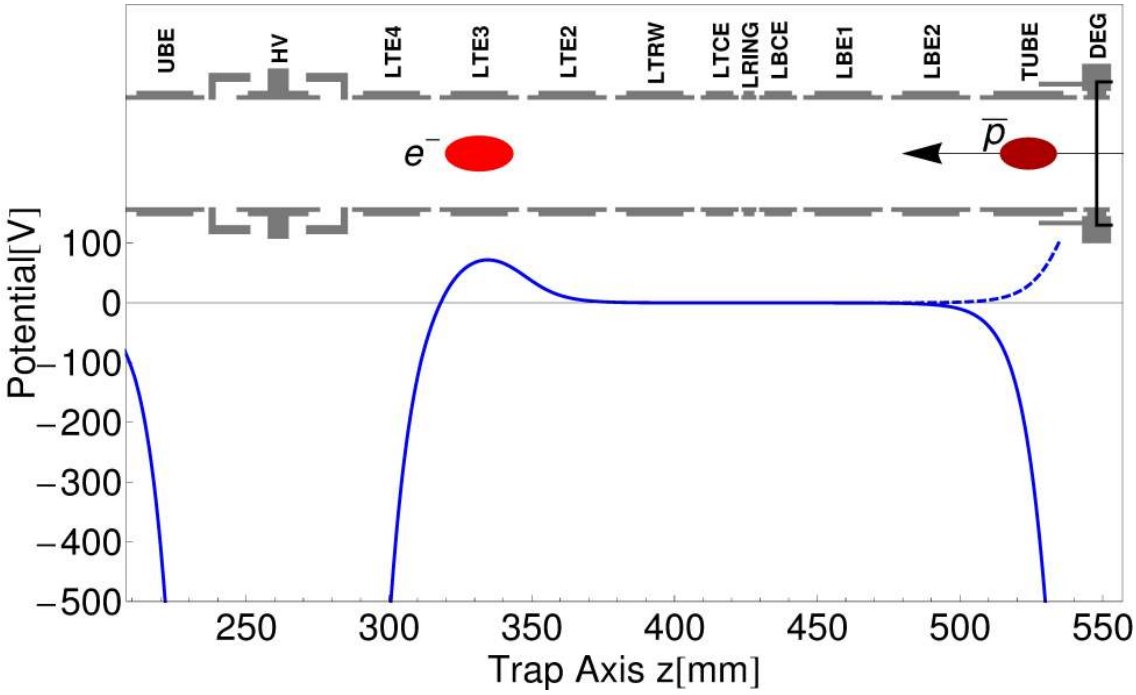

Figure 6.3: Potential structure for trapping and accumulating antiprotons. The electrodes *HV* and *DEG* are biased to −5 kV and form a confining well for high energy $\bar{p}$. On arrival of a $\bar{p}$ bunch from the AD, the barrier on *DEG* is pulsed up to let the $\bar{p}$ in. Once trapped, the $\bar{p}$ lose energy by collisions with pre-loaded electrons and cool into the e^- well on *LTE3* before the next shot of antiproton arrives from the AD.

by collisions with the electrons stored on electrode *LTE3* and cool into the e^- well before the next shot from the AD arrives.

The field boosting solenoid increases the magnetic field around the $\bar{p}$ trapping region to 3.7 T. Raising the field compresses the antiproton bunches to a smaller radius, which increases the fraction of $\bar{p}$ that can be retained. In the 1 T field of the large solenoid, about $3 \cdot 10^4$ $\bar{p}$ are caught per AD shot. With the magnetic field increased to 3.7 T, this number increases by a factor of five to $1.6 \cdot 10^5$. Furthermore, the stronger field reduces the time the electrons require to cool by synchrotron

radiation, equation (6.5). The dampening time is reduced to 0.19 s compared to 2.6 s in a 1 T field.

When the intended number of $\bar{p}$ has been accumulated, the mixed electron antiproton plasma is spun up to a radius of $r \simeq 2$ mm by a rotating wall drive applied to the segmented electrode *LTRW*. Afterwards, the plasma is stored in a 80 V deep well on *LTE3* and the electrons are removed by a series of fast voltage pulses. The confining potential well is pulsed to zero for 75 ns. This is short enough to allow a large fraction of the light electrons to escape while the much heavier antiprotons remain trapped. Typically, three or four pulses are applied which leaves a small number of electrons in the $\bar{p}$. From the initial 10^8 e^-, about $6 \cdot 10^3$ or $9 \cdot 10^2$ are retained from three or four pulses, respectively. These numbers are small enough so that they do not affect antihydrogen experiments, but they still provide cooling for the $\bar{p}$ [64]. The rapid voltage pulses heat the $\bar{p}$, so the plasma is left to cool for 10 minutes.

Afterwards, the field boosting solenoid is ramped down. During the ramp, the radius of the $\bar{p}$ plasma expands to almost twice its original value. Without compression from the rotating-wall drive, a large fraction of the $\bar{p}$ would hit the electrode walls during expansion and annihilate. With the magnetic field lowered to 1 T, the antiprotons are transfered to the upper part of the electrode stack where they can be used for antihydrogen experiments.

About $1.6 \cdot 10^5$ to $2 \cdot 10^5$ antiprotons are caught per shot, depending on the performance of the AD. The field boosting solenoid and rotating-wall drive allow linear accumulation of up to 10^7 antiprotons in a time of 90 minutes. This is an improvement by a factor of 14 compared to the $7 \cdot 10^5$ $\bar{p}$ that were previously accumulated in the 1 T field. Up to 10^6 $\bar{p}$ are loaded loss-free. For larger plasmas, a few percent of the antiprotons are lost during the rotating wall drive and the solenoid ramp

down. Most of our current experiments that produce antihydrogen by three-body recombination use 10^6 $\bar{p}$ per trial. For charge-exchange experiments, we typically use larger plasmas of $5 \cdot 10^6$ antiprotons.

6.1.4 Counting Particles

Well controlled experiments require the use of identical particle numbers for each trial. At ATRAP, the number of particles in our large plasmas is determined by one of two methods: Charge counting and annihilation detection. Only positrons can be counted by both methods. Our typical antiproton plasmas are too small to accurately measure their charge while annihilation detection of electrons would require an antimatter target. The two methods are destructive, so we have to rely on reproducible loading techniques. For each particle species, electrons, positrons and antiprotons, the number acquired per pulse depends on the performance of the corresponding source, the excimer laser, the positron accumulator and the AD. Since the conditions of these machines may vary, calibrations are run at the beginning of each series of experiments.

Charge Counting

Our plasmas consist solely of singly charged particles, therefore the total charge of the cloud Q is directly proportional to the number of particles in the plasma. To measure Q, the particles are sent onto a Faraday cup coupled to a charge-sensitive preamplifier. In the BTRAP Penning trap, the degrader foil used to slow antiprotons also serves as a Faraday cup. Figure 6.4 shows the potential for counting an electron cloud. The particles are held in a well on electrode *LTE3* and a voltage ramp towards the degrader is set up. The degrader itself is biased to a positive

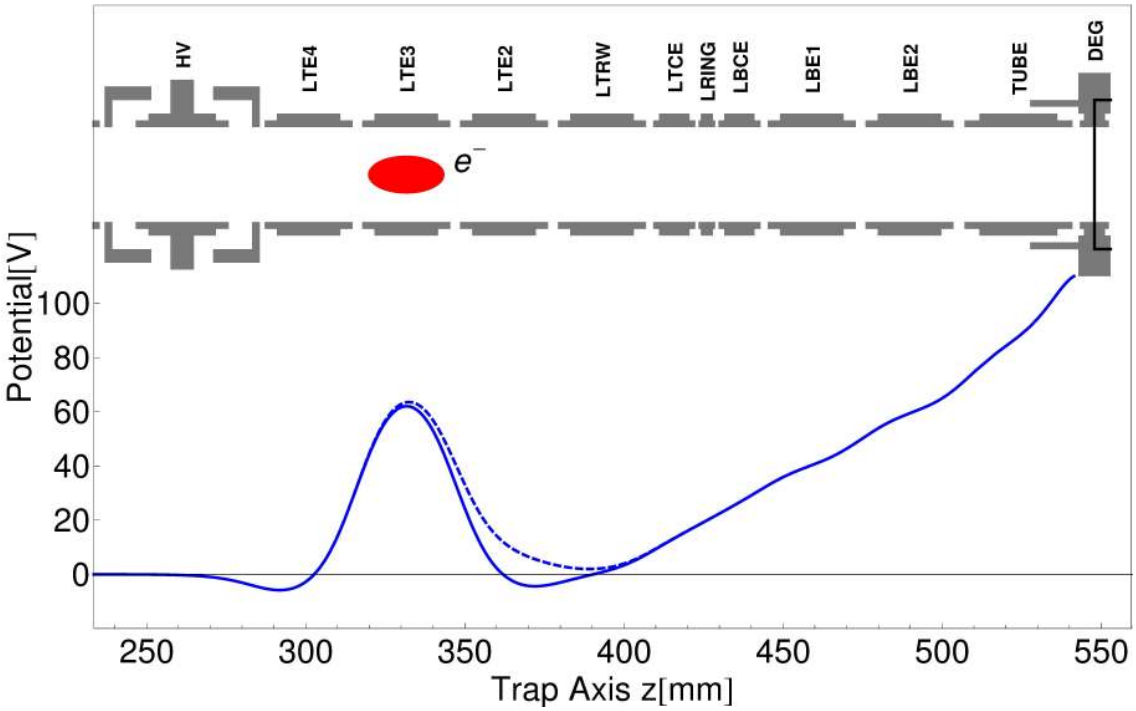

Figure 6.4: Potential structure for charge-counting electrons. The e^- are held in the well on *LTE3* and are pulsed onto the Be degrader foil. The well depth is gradually reduced, and after each step, the barrier is pulsed up (dashed line) allowing the most energetic particles to escape and hit the degrader. The degrader is connected to a charge-sensitive preamplifier. For e^+ counting, the sign of the potentials must be inverted.

voltage to suppress emission of secondary electrons. Each electron ejected from the foil would be counted as a positive charge hitting the degrader and would thus influence the result. To avoid saturation of the preamplifier, the electrons are ejected to the degrader in several steps of 1 s duration. In each step, the barrier on *LTE2* is pulsed up for 75 ns allowing the particles with highest energy to escape. Afterwards, the well depth is lowered by 2.5 V until the well is inverted. The measurement also determines the energy distribution of the plasma: High energy particles are pulsed out first while the coldest ones are deeply confined in the well and can only leave

when its boundary is sufficiently lowered.

Each pulse induces a noise in the charge sensitive preamplifier corresponding to an impact of about 100 000 charges on the degrader. Therefore charge counting is only suitable for our large lepton plasmas with $N = 10^7 - 10^8$. For positrons, the sign of the potential well and the ramp in figure 6.4 has to be inverted. The degrader must still be biased to a low positive voltage to suppress emission of secondary electrons. Our antiproton clouds typically only contain $N = 10^6$ particles, so counting the $\bar{p}$ via their annihilation signature is much more accurate.

Annihilation Counting

Particle counting via annihilation detection essentially works in the same manner as charge counting. The particles are held in a potential well and are gradually pulsed onto the degrader. This is identical to the procedure depicted in figure 6.4. Instead of the charges, the annihilation events registered by our detector system are used to count the particles. The scintillating paddles and fibers are specifically designed for detection of antiproton annihilations, see section 6.4.2. Therefore this method is most suited for counting antiprotons. The 511 keV γ quants from positron annihilations are also registered by the scintillating fibers, but only with a low efficiency of 0.5 %. The scintillating paddles are not sensitive to the γ particles. Still, the e^+ plasmas used are large enough so that annihilation counting of positrons is also a valuable and frequently used method.

6.2 Choice of Rydberg State

Our new laser system allows us to access a wide range of Rydberg states (chapter 5). In principle, all of these states are usable for charge-exchange production of antihydrogen, but in practice a number of factors severely limit the effectivity of most states. Low levels are not suited because of their small cross sections while for high states, the excitation efficiency strongly decreases. In the following section, the relevant factors are discussed and evaluated to find an optimum Rydberg state.

The cross sections for charge-exchange collisions were calculated in [82] by classical trajectory Monte Carlo (CTMC) simulations. They are proportional to the geometric size of the atom and therefore scale with $r^2 \propto n^4$. For the charge-exchange production of positronium and antihydrogen, the simulations resulted in

$$\sigma_{Ps} = 9.7\, n_{Cs}^4\, \pi a_0^2\,, \tag{6.6}$$

$$\sigma_{\bar{H}} = 58\, n_{Ps}^4\, \pi a_0^2\,, \tag{6.7}$$

where a_0 is the Bohr radius and n_{Cs} and n_{Ps} are the principal quantum numbers of the cesium and positronium atoms, respectively. The binding energy is transfered in the charge-exchange collisions, but due to the different reduced masses in the two systems, $\mu_{Cs} \simeq m_e$ and $\mu_{Ps} = 1/2\, m_e$, the same binding energy corresponds to a different n state, namely $n_{Ps} = n_{Cs}/\sqrt{2}$ [82]. For $n_{Cs} = 40$, the cross section values are $\sigma_{Ps} = 2.2 \cdot 10^{-9}\,\mathrm{cm}^2$ and $\sigma_{\bar{H}} = 3.3 \cdot 10^{-9}\,\mathrm{cm}^2$. These cross sections were originally calculated in absence of a magnetic field. However, later simulations show only small deviations if a magnetic field is included [45, 132].

The Rydberg cesium atoms must cover a distance of 6 cm from the laser excitation region to the center of the trap, where the positrons are stored (figure 3.11). At

thermal velocities, this corresponds to a time of flight of 220 μs. Without a magnetic field, the lifetime of the $40D$ state is $\simeq 38\,\mu$s [55] so that most Rydberg atoms would decay before reaching the positrons. While the magnetic field complicates laser excitation, it has a positive effect on the lifetimes of the Rydberg states: The field mixes the D state with higher l orbitals which have much longer lifetimes. Thus, the lifetime of the resulting state is significantly larger than the zero-field D state. The amount of l-mixing is determined by the relative strength of the magnetic field. It increases for higher n-states or stronger fields. If the final n-state is an equal mixture of all l- and m-levels, its lifetime is given by [26]

$$\tau = \frac{3}{4}\left(\frac{n}{\alpha}\right)^5 \frac{\hbar}{\mu c^2}\left(ln(2n-1) - 0.365\right)^{-1} . \tag{6.8}$$

A fully mixed $n = 40$ Rydberg state in cesium already has a lifetime of more than 1 ms, so practically all Rydberg atoms survive until they reach the positrons. Measurements with the front- and rear side field ionization detectors (see figure 3.11) indicate that for $n = 40$ and $B = 1\,\mathrm{T}$, we are not in the fully mixed regime, yet. A rough estimate using the signal amplitudes from front- and rear-side detectors and the expected loss from geometric factors gives a lifetime of about 170 μs for the $n = 40$ state. The lifetime is therefore significantly prolonged by l-mixing, but the losses from decay of the excited state are not negligible. With a lifetime of 170 μs, less than 30 % of the cesium atoms are still in an excited state when reaching the positrons.

The cross sections and lifetime favor using states as high as possible. On the other hand, the l-mixing that increases the lifetime also decreases the efficiency for laser excitation. From the intermediate $6P_{3/2}$ level, optical dipole transitions are only possible to an S or D state. The more l-mixing occurs, the less S or

D character is preserved in the final state, thus reducing the efficiency for laser excitation. Additionally, the oscillator strengths also decrease for larger values of n.

The lower binding energy of higher n-states is also an important factor. The electric field amplitude required to field-ionize a Rydberg atom scales with n^{-4} [69]

$$E_{FI} = \left(\frac{\mu}{m_e}\right)^2 3 \cdot 10^8 \frac{1}{n^4}\,\mathrm{V/cm}\,. \tag{6.9}$$

In higher n-states, the atoms are therefore easier stripped by stray fields or the space charge potential of the positron cloud. This limits the number of positrons that can be used per experiment.

As shown in figure 6.5(a), these factors scale over several orders of magnitude for the cesium states of interest. To find the optimum Rydberg state, all the relevant factors must be taken into account. First of all, the cesium atoms are laser excited. In general, the oscillator strengths scale as n^{-3} [69]. The l-mixing from the magnetic field further reduces the excitation efficiency. If the lifetime of the n-state is too low, a significant fraction of the Rydberg atoms will decay in flight. For sufficiently high states, practically all Rydberg atoms reach the positrons and an excitation to still higher n-states only results in a minimal gain. These factors determine the fraction of cesium atoms that reach the positrons in a Rydberg state. The efficiency of the charge-exchange process itself is then determined by the cross sections, equations (6.6) and (6.7), and the number of positrons and antiprotons. The number of e^+ is limited by their space-charge potential. The electric field generated must be kept below the field required to Stark-ionize the Rydberg states, equation (6.9). The number of antiprotons used is typically two orders of magnitude smaller, so their space charge potential can be neglected here.

The result of this optimization, the normalized cross section for antihydrogen production per Cs atom, is shown in figure 6.5(b). The steep increase on the left

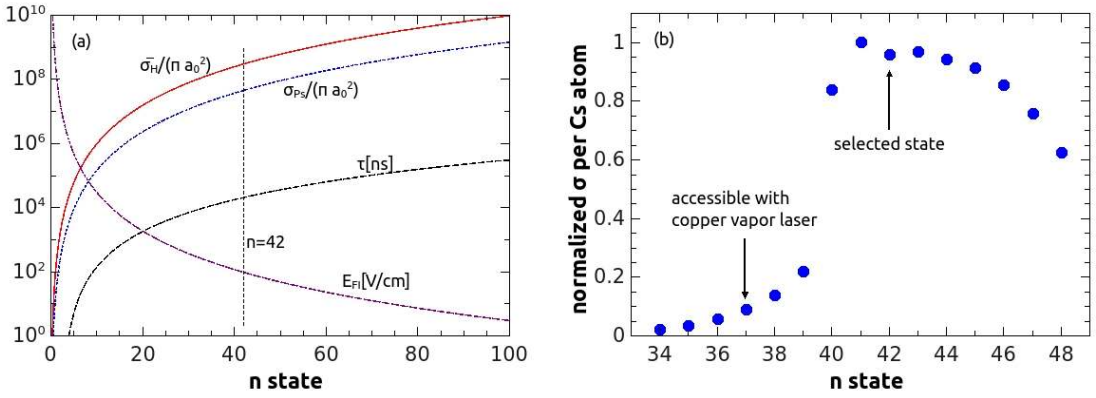

Figure 6.5: Selection of the optimum Rydberg state. (a) Factors that contribute to the antihydrogen production efficiency scale over several orders of magnitude. Namely, they are the cross sections for Ps and $\bar{H}$ production σ_{Ps} and $\sigma_{\bar{H}}$, respectively, the lifetime of the Rydberg state τ and the electric field amplitude E_{FI} necessary to Stark-ionize the Rydberg atoms. (b) The normalized cross section for antihydrogen production considering these factors shows a narrow maximum around the selected $n = 42$ state. The level accessible with the fixed-frequency copper vapor laser is also indicated.

hand side is due to the n^4-dependence of the cross sections and the increasing lifetimes of the Rydberg states. The gain from longer lifetimes levels off above $n \simeq 40$. The l-mixing becomes more prominent in this regime as the spacing between neighboring energy levels decreases and the overall decline in excitation efficiency causes the drop on the right hand side of the plot. The curve has a narrow maximum centered around $n = 42$, which is the state we select to use. Cesium atoms in this state survive electric fields up to $\simeq 100\,\mathrm{V/cm}$ (see figure 5.5(c)), which is sufficiently large to avoid ionization by stray fields within the trap. It allows us to use plasmas with up to $3 \cdot 10^8$ positrons.

As indicated in figure 6.5(b), the $n = 37$ level used in ATRAP's earlier experiment in 2004 [126] has a much lower efficiency. This state was set by the fixed

frequency of the copper vapor laser. The 2004 experiment used a five times larger magnetic field of 5.3 T. Since this causes stronger l-mixing at lower n-states, the maximum in figure 6.5(b) is shifted towards lower Rydberg states in this case. However, using the copper vapor laser and therefore the $n = 37$ state in the 1 T field of our current apparatus would decrease the production efficiency for antihydrogen by an order of magnitude.

The quadrupole Ioffe trap increases the magnetic field at the laser excitation region to 3.6 T. The same optimization could not be done in this stronger field since too many states would have to be included in the determination of the remaining S and D character (see section 5.1.4). Instead, we chose $n = 38$, one level above the $n = 37$ state used in the 5.3 T field.

The wide tunability of our new laser system proved to be an important advancement. Since it offers access to all Rydberg states above $n = 20$, it allows us to select the state most fitting to the experimental conditions.

6.3 Positronium

With the prerequisites for charge-exchange experiments attended to, the next step is to examine the first charge-exchange reaction: the formation of Rydberg positronium. As for other antihydrogen experiments, the voltages applied to the Penning trap electrodes must be thoroughly chosen. The potential structure used for Positronium production is shown in figure 6.6. When designing such a structure, a number of possible issues must be avoided. Any voltage applied to the cesium electrode *CS* produces an electric field which adds to that generated by the space charge of the positrons. To avoid ionization of incoming Rydberg cesium atoms and to maximize the number of e^+, the voltage on *CS* is set to 0 V for all charge-exchange experi-

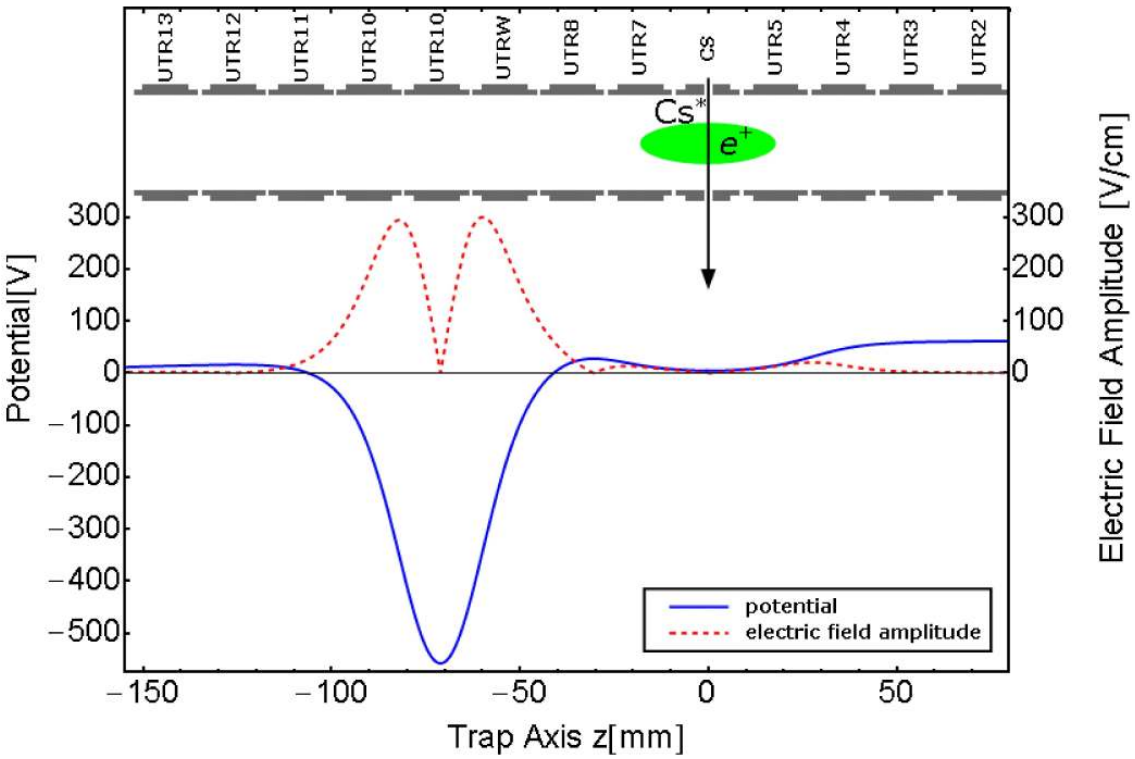

Figure 6.6: Potential structure for Positronium experiments. The solid blue line shows the potential along the trap axis, the dashed red line corresponds to the electric field amplitude. The e^+ are initially placed into a shallow harmonic well centered on the CS electrode. When Ps^* are made, they leave this well and some will enter the deep detection well to the left which ionizes the Ps^* and traps the e^+. The lower end of the trap is towards the right hand side of the figure.

ments. The positrons must be held in a harmonic potential to avoid expansion of the plasma. Minimizing the anharmonic coefficients C_4 and C_6 (section 3.2) constrains the voltages on the electrodes neighboring *CS*.

To verify the production of Positronium, a detection well is set up on electrode *UTR10*. This technique was first developed to detect antihydrogen produced by

three-body recombination [59], but it is also applicable to similar excited atomic systems like Positronium. A voltage of 1000 V is applied to an electrode close to the positrons, which generates a deep potential well. Positronium atoms that form by charge-exchange collisions in the positron plasma are electrically neutral and therefore not confined by the Penning trap. They emerge with a roughly isotropic distribution and some enter the detection well. The strong electric field Stark-ionizes the positronium atoms on entry and the positrons are confined in the detection well. The well can trap positrons from Ps^* that ionize between 50 V/cm and 300 V/cm. The upper bound is given by the maximum voltage of 1000 V that can be applied to the electrode *UTR10*. Figure 5.5(c) shows that a field of 300 V/cm is sufficient to ionize all cesium atoms in the $n = 42$ state. The binding energy of the Rydberg Cs^* is transfered in the charge-exchange collisions first to positronium and then to the antihydrogen atoms. These are therefore Stark-ionized by the same electric field amplitude. A field of 300 V/cm Stark-ionizes cesium atoms in states from $n = 32$ upwards, equation (6.9). While some fraction of the Cs^* atoms will decay in flight (compare section 6.2), this is no issue for the positronium. For a sufficiently cold positron plasma, their velocity is determined by the classical speed of the Rydberg electron in the cesium atom:

$$v = \frac{e^2}{4\pi\epsilon_0 n\hbar}\,. \tag{6.10}$$

For $n = 42$ this equates to $v = 52000\,\mathrm{m/s}$ and the Ps^* will reach the detection well within $1\,\mu$s. Positronium forms in a state with $n_{Ps} \simeq n_{Cs}/\sqrt{2} \simeq 30$ [82]. From equation (6.8), a lifetime larger than $600\,\mu$s is expected, so practically no Ps^* will decay on its way to the detection well. The e^+ from Ps^* that ionizes below 50 V/cm cannot be confined. These atoms are stripped high up in the shoulder of

the detection well between electrodes *UTR8* and *UTRW* and since the barrier on the left hand side of the well must be lower (see below), the positrons gain enough energy to pass through the detection well and leave on the left hand side. A stripping field of 50 V/cm can only ionize states with $n_{Ps} \geq 35$. The distribution of n_{Ps} from $n = 42$ cesium atoms is sharply peaked around $n_{Ps} = 30$. Therefore we expect to catch the majority of the Ps^* atoms produced in the detection well.

After an experiment, the remaining particles from the initial positron well are ejected. The particles in the detection well are then counted by the methods described in section 6.1.4. Each positron found in the detection well corresponds to a Positronium atom. To prevent false counts, the potentials must be designed so that all positrons which escape from their initial well by some mean pass through the detection well without being confined. To this purpose, the left hand side of the detection well is slightly lower so that all charged particles that cross the right hand side barrier have sufficient energy to exit the detection well again. The slope on the right hand side of the positron well is designed to guide electrons towards the degrader. A potential structure with a second detection well, as it was used previously [122], could trap electrons with high energies that would oscillate through the positrons, heating them up and reducing the production efficiency. The potential structure used now is designed to guide every free charged particle to the upper or lower end of the trap in a single pass.

Before each experiment, the cesium oven is pre-heated with the lasers blocked (see section 3.3.3). When the beam blocker is opened, we see an immediate rise in the event rate of the scintillating fibers caused by positronium atoms that leave the e^+ well and annihilate on the electrodes, see figure 6.7. When the laser is blocked again, only ground state cesium is sent into the positron cloud and due to the much lower cross section, no positronium is made and the detector signal reduces to

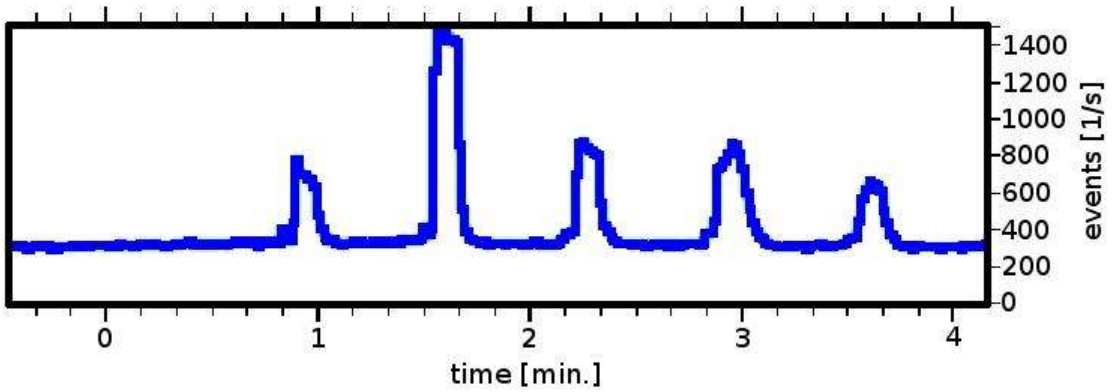

Figure 6.7: Signal from the scintillating fibers during a positronium experiment. The lasers are sent into the apparatus for 10 s intervals with 30 s pauses in between. The laser excited cesium atoms interact with the e^+, forming positronium which then emerges from the trap and annihilates on the walls. Due to the n^4 dependence of the cross section, no positronium is produced when the lasers are blocked and the count rate from the fibers drops to background.

background. Figure 6.7 shows the signal from the scintillating fibers when the lasers are sent into the trap for 10 s intervals, separated by 30 s. This specific measurement was started with the cesium oven still in its warm-up phase, therefore the second plateau is higher than the first one. It also used a higher flux of Cs^* than most other experiments, therefore the e^+ are used up in a short time causing the decrease in signal amplitude. No difference is observed whether both lasers are blocked or only one at a time. Taking the detector efficiency of 0.5 % for positron annihilations into account, the trace in figure 6.7 corresponds to about $6 \cdot 10^6$ Ps^* produced in the five "laser-on" cycles.

For a more thorough series of Positronium experiments, clouds of 30 million e^+ with a radius of 4.5 ± 0.5 mm are loaded and placed into the potential structure of figure 6.6. The cesium source is pre-heated for 360 s. The beam stopper is opened after 390 s for a time window ranging from 225 s to over an hour. After the run,

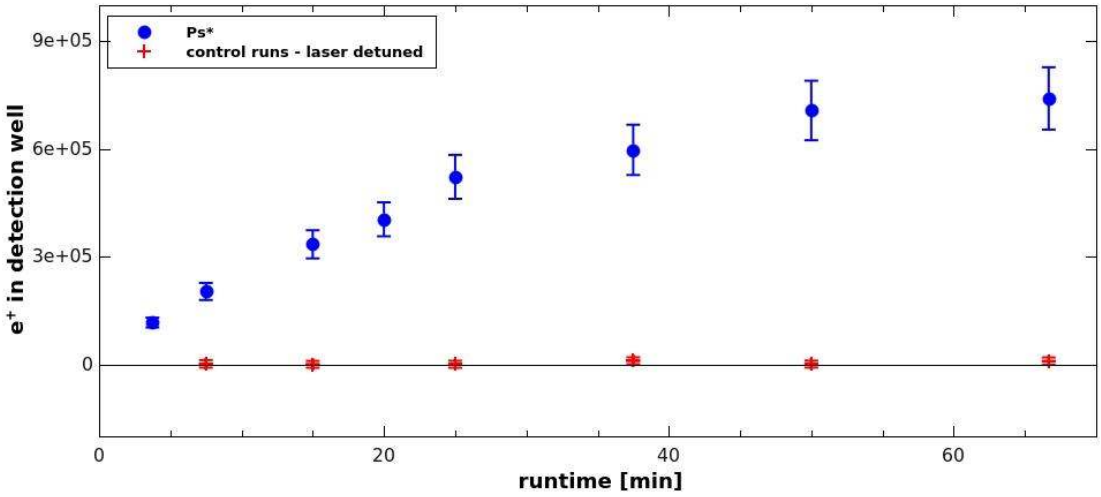

Figure 6.8: Number of positrons found in the detection well for different runtimes of the cesium oven. Each e^+ corresponds to a Positronium atom emerging from the e^+ well on-axis. The number saturates around 750 000 Ps^* when all of the 30 Million e^+ are used up. In control trials with the infrared laser detuned, no e^+ are found in the detection well.

the remaining e^+ from the initial well are ejected and finally, the positrons from the detection well are pulsed to the degrader and counted using the scintillating fibers (section 6.1.4).

The results are shown in figure 6.8 for the cases of the lasers tuned to the cesium resonances (blue circles) and the infrared laser detuned (red crosses). In the first case, we find reproducible numbers of positrons in the detection well that increase with runtime. Each e^+ corresponds to a positronium atom that emerged from the positron well on axis. Only those will reach the $\bar{p}$ and are thus usable for antihydrogen production. The error bars in figure 6.8 originate from averaging over several trials for each runtime. The number of e^+ found first increases almost linearly and then saturates around 750 000 when all positrons in the initial well

are used up. In later antihydrogen experiments using larger positron clouds, over 1 million positronium atoms were detected by charge counting electrons confined in an antihydrogen detection well (see section 6.4). If the 852 nm laser is detuned from resonance, the positrons only interact with ground state cesium and due to the much lower cross section, no positronium atoms are produced. All data points from these control trials are consistent with zero.

The numbers from our longest trials correspond to a on axis angular production efficiency of

$$\frac{dN_{Ps}}{d\Omega} = 2.1 \cdot 10^6 \,\text{atoms/sr}\,, \tag{6.11}$$

which is an increase by a factor of 520 compared to previous results [122]. Most of this is due to the larger particle clouds that are now available in the new apparatus. The earlier experiments were limited by their positron source to $2 \cdot 10^5$ e^+ per trial, a factor of 150 less. Normalized to the number of positrons, our efficiency is still larger by a factor of three. This is most likely due to eliminating the second detection well used in [122] which formed a large trapping well for electrons with the positrons located in its center so that the e^- could oscillate through the positrons and heat them.

6.4 Antihydrogen

With the production of Rydberg positronium well under control, the following section focuses on antihydrogen experiments. The first part, section 6.4.1 describes the series of measurements performed and a new detection method developed to verify production of antihydrogen atoms. This method requires a more elaborate analysis of the data gathered from the detector system, which is subject of section 6.4.2.

The final results are then presented in section 6.4.3.

6.4.1 Experiments

The potential structure for antihydrogen production has to meet the same requirements than the one for the positronium experiments, with the additional complication that a second harmonic potential well must be included to hold the antiprotons. The positronium atoms emerge from the e^+ cloud with an almost uniform distribution [45]. To maximize the number of Ps^* that interact with the antiprotons, the $\bar{p}$ must be placed as close to the e^+ as possible. Ideally, both particle clouds are held on neighboring electrodes. On the other hand, harmonic wells are necessary to limit expansion of the plasmas. In our stack of radius length electrodes, this requires wells that span over several electrodes.

The final potential structure is a compromise between these two conflicting requirements. It is shown in figure 6.9. The positron well is similar to the structure used for positronium experiments, figure 6.6. The antiprotons are located in a shallow well on electrodes *UTR3* and *UTR4*.

The distance from the positron well to the antiprotons is about the same than to the positronium detection well in figure 6.6. Therefore the same fraction of positronium atoms that reach the detection well is also available for charge-exchange production of antihydrogen. The detection well on *URING* and its neighboring electrodes is identical to the one used for the Positronium experiments, only its sign is inverted to confine antiprotons instead of positrons. As before, potential ramps guide electrons onto the degrader and unbound positrons towards the upper end of the electrode stack. This ensures that no free charged particles oscillate through the trap heating the e^+ or $\bar{p}$ plasmas.

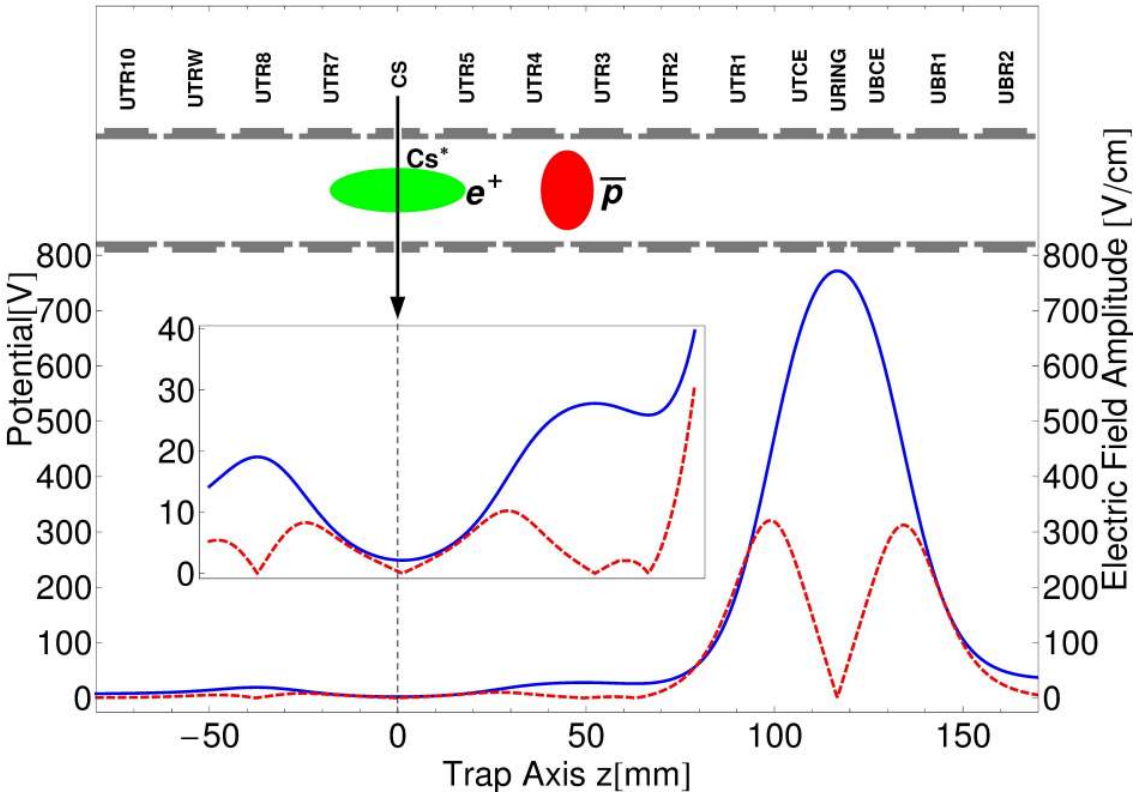

Figure 6.9: Potential structure for charge-exchange production of antihydrogen. Compared to the structure for Ps^* production, figure 6.6, it has an additional well containing antiprotons and the sign of the detection well is inverted to confine antiprotons from stripped $\bar{H}$. The y-axis of the inset is magnified by a factor of 10. As before, the lower end of the trap is towards the right hand side of the figure.

The number of positrons used per experiment is limited by the particle's space-charge potential. Cesium atoms in the $n = 42$ state ionize at fields of about 100 V/cm and above, figure 5.5(c). We set a factor of two safety margin in the acceptable electric field amplitude, limiting it to 50 V/cm. This corresponds to a maximum of $3 \cdot 10^8$ positrons per experiment, ten times more than for the positro-

nium trials in section 6.3 and 200 times more than used in ATRAP's first charge-exchange experiment [126]. The antiproton plasmas typically used at ATRAP are two orders of magnitude smaller, so their space-charge is no issue. For our charge-exchange experiments, we use on average $5 \cdot 10^6$ antiprotons per trial, 20 times more than before.

As before, the cesium oven is pre-heated for 360 s. When the laser beam blocker is opened, we observe the same increased event rate from the fiber detectors as in our positronium experiments (figure 6.7). This indicates that Ps^* atoms are produced as before. During a runtime of one hour, almost all of the positrons are used up, while a large fraction of the antiprotons is retained. From the cross sections, equations (6.6) and (6.7), and the initial numbers we expect production of several 10^3 antihydrogen atoms, so most of the $\bar{p}$ should be left in their well.

Despite these promising indications, we did not find any antiprotons in the detection well in any of our trials. This means that either no $\bar{H}$ are produced, or they are made, but not detected. In the second case, the detection well would either be unable to strip the antihydrogen atoms or to confine the antiprotons.

To investigate this, we performed a series of tests. First, we used the fact that a detection well for antihydrogen will also ionize Positronium atoms and trap the electrons. We therefore charge-counted the content of the detection well at the end of a run (section 6.1.4). In two trials, we found an average of $1.0 \pm 0.28 \cdot 10^6$ negative charge counts when the detection well was pulsed out. The detector system showed no events above background during the pulsing, therefore the charges must originate from electrons and not from antiprotons. In control runs with the infrared laser detuned, no electrons were found in the detection well. These runs show that:

- We are making Positronium atoms during our antihydrogen experiments.

- Since the detection well is behind the $\bar{p}$ plasma (figure 6.9), at least 10^6 Ps^* atoms must have crossed the antiprotons and thus have had the possibility to form antihydrogen.

- The detection well used is capable of stripping atoms with the same binding energy than the antihydrogen atoms that should be produced. It can also confine light charged particles.

This test rules out a couple of possible errors but does not definitely answer the question whether antihydrogen is not produced or not detected. Therefore we simulated antiproton capture by dropping a small amount of $\bar{p}$ in a detection well. A cloud of about $90\,000\,\bar{p}$ is placed in a shallow well next to a deep detection well. The small barrier between the two is either pulsed down or slowly lowered. A series of runs was done for different depths of the detection well. We find that for on axis well depths below 200 V, only about half of the antiprotons are retained. For depths above 500 V, almost no $\bar{p}$ remain in the well. This includes the detection well used for our $\bar{H}$ trials. The 1000 V applied to the electrode *URING* corresponds to an on-axis well depth of 760 V. The results are largely independent of how the the barrier is lowered and the exact shape of the detection well. Also, placing the well on different electrodes does not affect the outcome. We suspected that the electrons from stripped Ps^* might have a negative effect on the $\bar{p}$. For instance, the centrifugal separation of the two particle species observed in different experiments [65] may drive the $\bar{p}$ out of the detection well radially. This, however, is a plasma effect which should not occur at the low particle densities we expect in the detection well. On the other hand, electrons may cool the antiprotons and thus help to stabilize the $\bar{p}$ in the detection well. To determine the influence of electrons, a number of runs were repeated with e^- preloaded into the detection well. However, no effect

from the presence of electrons is observed.

If antiprotons are loaded into a shallow well which is then deepened to 1000 V, all of them are retained. This indicates that, in contrast to the lighter electrons and positrons, the antiprotons are not trapped when they fall into the 1000 V deep detection well. So far, the reason for the different behavior has not been identified. Previous charge-exchange experiments successfully used detection wells, but required much lower voltages due to a smaller radius of the trap electrodes [126]. Instead of 760 V, the on axis well depth was only 250 V. These experiments differed in a second important aspect which may also be related to the $\bar{p}$ behavior, the strength of the magnetic field. The previous experiments of 2004 used a field of 5.3 T, more than five times larger than the 1 T field in our current setup.

The detection well was initially developed to count antihydrogen atoms produced by three-body recombination [59]. The TBR process forms $\bar{H}$ in very high n states, well above the Rydberg states used for charge-exchange experiments. Therefore the well depths required are also much lower, on the order of 200 V, and detection wells have been successfully used for various experiments. Since a shallow well may be able to retain $\bar{p}$, we reduced the well depth from 1000 V to 450 V. This also reduces the amplitude of the stripping field, so we had to excite to a higher cesium Rydberg state of $n = 50$ instead of $n = 42$. Unfortunately, the overall efficiency at this high n state is greatly reduced (compare figure 6.5). The production efficiency for positronium already dropped to 1/6, despite running the cesium oven at a higher current and we were unable to see a signal from the $\bar{H}$ detection well.

Although the reason remains unclear, these test show that, under our experimental conditions, a detection well is not a suitable tool to verify antihydrogen production. Therefore we developed a different method depicted in figure 6.10. The infrared laser is modulated with a mechanical chopper wheel, thus switching between

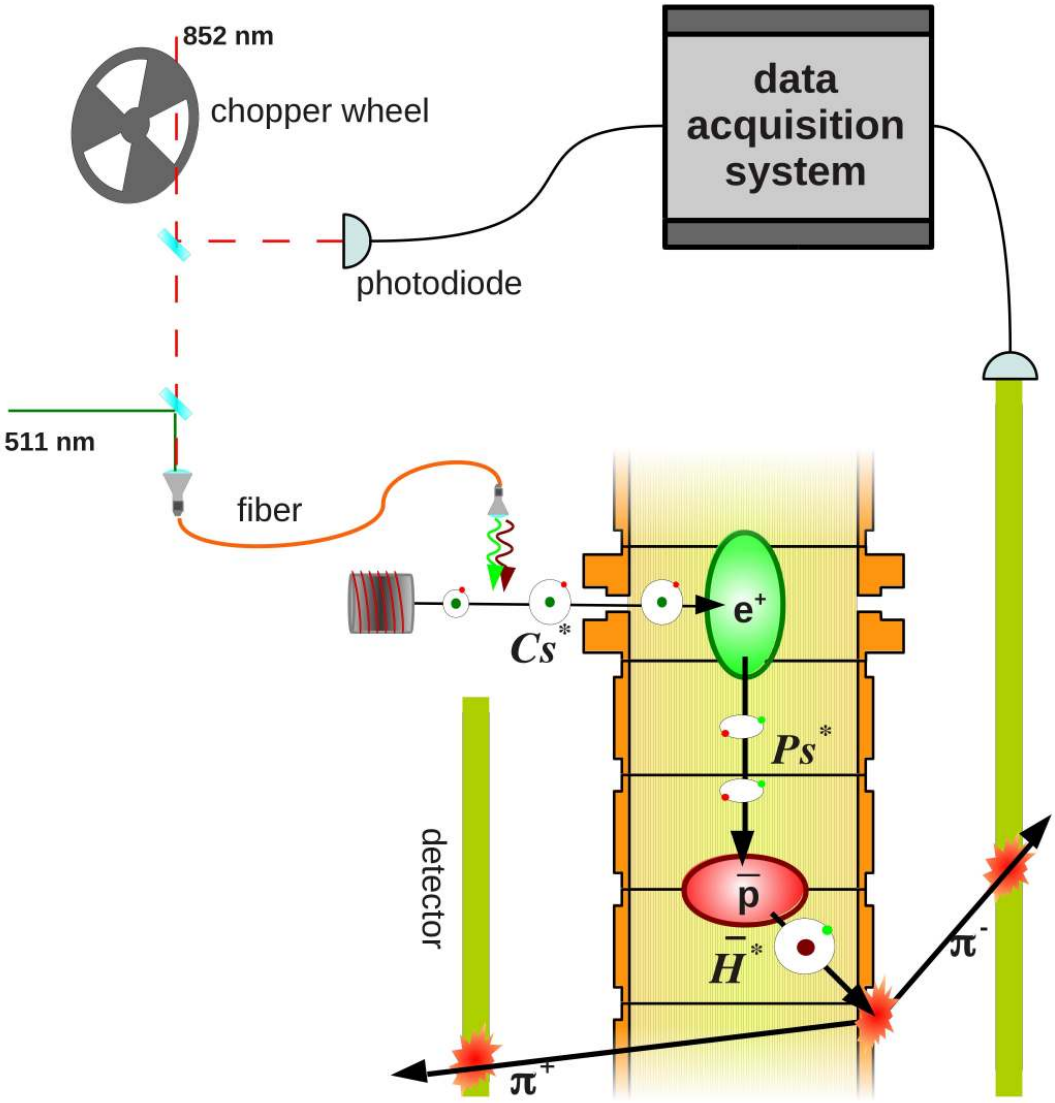

Figure 6.10: New detection method to verify the production of antihydrogen: The 852 nm laser is modulated with a chopper wheel. $\bar{H}$ production only happens when the laser light reaches the excitation region and can be seen as excess $\bar{p}$ annihilations during these time windows.

ground-state and Rydberg cesium atoms. To keep the changes as minimal as possible, only the low power infrared laser is modulated while the much stronger green laser is sent in continuously. In the time windows when both lasers are sent into the trap, cesium atoms are excited to Rydberg states, followed by charge-exchange production of positronium and then antihydrogen. Like positronium, the antihydrogen atoms are not confined by the Penning trap and drift to the walls of the electrodes where they annihilate. In the time slots when the infrared laser is blocked, only ground state cesium is sent into the trap and due to the much lower cross section, no charge-exchange reactions occur.

An analysis of the data collected from our detector system should therefore show an excess of antiproton annihilations in the time slots when the infrared laser is sent into the trap. To determine these time windows accurately, a small fraction of the infrared light is split off after the chopper wheel and recorded with a photodiode. This signal is directly fed into an input channel of the detector's data acquisition system. For consistency, the potential structure of figure 6.9, including the detection well, is used for these trials, too. We performed a series of experiments with this new detection technique, but before presenting the results, the analysis of the detector data is discussed in the following section.

6.4.2 Data Analysis

The detector system is described in section 3.4. It consists of two rings of scintillating paddles and four layers of scintillating fibers, two vertical straight layers and two helical layers. The data acquisition system (DAQ) offers two monitoring modes: An online readout providing essential informations in real time and the full acquisition system gathering more detailed data at a higher rate for a later analysis.

event type	fibers firing	paddles firing	efficiency	bg rate [Hz]
fiber	≥ 1	-	2.1	2500
paddle	-	≥ 1	0.75	450
Trigger 1	≥ 2	≥ 1	0.48	30
Trigger 2	≥ 2	≥ 2	0.16	4

Table 6.1: Criteria, efficiencies and background rates for the four event types commonly used with the online detector readout. The efficiencies are for annihilations of $\bar{p}$ on the degrader foil, as used for particle counting (section 6.1.4). Since the foil is below the fiber ring, the efficiencies for detection $\bar{p}$ that annihilate in the trap are higher.

The DAQ registers four different event types which differ in background rates and efficiency to detect p-$\bar{p}$ annihilations. They are listed in table 6.1. The simplest case is a fiber count, which corresponds to a signal from a single fiber. It has the highest sensitivity, but also the highest background rate which is caused by cosmic particles that constantly hit the detectors. The scintillating paddles are operated in coincidence mode. A "paddle count" is registered when one of the 16 inner paddles and the corresponding outer paddle fire within a 40 ns time window. Additionally, two combined event types are defined: A "Trigger 1" event corresponds to at least two fiber counts in coincidence with one paddle count. The more strict "Trigger 2" event requires two fiber counts in combination with two paddle counts. These event types are mostly used with the online readout.

The online system provides information about the status of an experiment in real-time. For instance, antiproton shots from the AD can be observed during $\bar{p}$ loading or losses from antimatter plasmas are instantly detectable. The online readout has a maximum time resolution of 0.1 s. This is sufficient for real-time monitoring, typ-

ically it is run with 1 s resolution, but for a more sophisticated analysis, a higher time resolution is required. Also, the online readout only counts how many scintillating fibers fired, but it does not record specifically which fibers registered a signal. However, this information is valuable to discriminate between antiproton annihilations and events caused by cosmic particles. An antiproton annihilating with its matter twin typically generates several pions that leave on randomly distributed trajectories. A cosmic particle on the other hand crosses the detector system in a straight line. If all fibers and paddles that fire during an event are located on a straight line, the event is most likely produced by a cosmic particle and is therefore discarded. The position information is only recorded by the full data acquisition system. This system also provides a higher time resolution of up to 1000 events per second with a dead time of less than 20 %. Since it generates large amounts of data, it is only used when its high sensitivity is needed, for instance when looking for trapped antihydrogen atoms [62] or during charge-exchange production of $\bar{H}$.

Each scintillating fiber and especially each paddle has a significant volume. It is not traceable exactly where within this volume the detector was hit by a crossing particle. Therefore identifying straight line trajectories and eliminating events caused by cosmic particles requires a thorough analysis after an experiment. Each event is characterized by its number of fiber- and paddle counts, the spatial distribution of these hits and how many adjacent fibers and paddles were triggered. The first step in the analysis is to group all straight fibers that fired during an event into clusters. A passing particle may strike several fibers, therefore clusters can contain one or more fibers. A cluster with at least two fibers is referred to as "multiplicity-2". This distinction is made since a single triggered fiber may also be due to electrical noise. The energy deposited in a fiber from a grazing particle may be too low to trigger it, therefore single "dark" fibers are accepted within a cluster

and a distance of at least two dark fibers is required between two clusters. Next, the number of clusters separated by an angle of at least $\pi/8$ radians is counted. The angle, although somewhat arbitrary, is chosen large enough to ensure that the two clusters are clearly separated. The same analysis is done for the helical fibers. For the scintillating paddles, the number of coincidence counts and non-neighboring coincidence counts is determined.

We then test whether the events fulfill twelve criteria originally, developed in [100]. The test checks whether the event contains:

1. ≥ 1 paddle coincidence.

2. ≥ 3 helical fiber clusters.

3. ≥ 3 straight fiber clusters.

4. ≥ 3 non-neighboring paddle coincidences.

5. ≥ 5 fiber clusters, helical or straight.

6. ≥ 5 helical fiber clusters OR
   ≥ 4 multiplicity-2 helical fiber clusters OR
   ≥ 4 helical fiber clusters separated by more than $\pi/8$ OR
   ≥ 3 multiplicity-2 helical fiber clusters separated by more than $\pi/8$

7. ≥ 5 straight fiber clusters OR
   ≥ 4 multiplicity-2 straight fiber clusters OR
   ≥ 4 straight fiber clusters separated by more than $\pi/8$ OR
   ≥ 3 multiplicity-2 straight fiber clusters separated by more than $\pi/8$

8. ≥ 2 helical fiber clusters AND ≥ 1 straight fiber cluster or paddle coincidence.
   A straight line through the helical fiber clusters may not pass through the straight fiber cluster or paddle.

9. ≥ 2 straight fiber clusters AND ≥ 1 helical fiber cluster or paddle coincidence.
   A straight line through the straight fiber clusters may not pass through the helical fiber cluster or paddle.

10. ≥ 2 paddle coincidences AND ≥ 1 fiber cluster, helical or straight.
    A straight line through the paddles may not pass through the fiber cluster.

11. ≥ 2 multiplicity-2 helical fiber clusters separated by more than $\pi/8$
    AND ≥ 1 paddle coincidence or ≥ 2 straight fiber clusters.
    A straight line through the helical fiber clusters must miss the paddle or straight fiber clusters by at least $\pi/8$.

12. ≥ 2 multiplicity-2 straight fiber clusters separated by more than $\pi/8$
    AND ≥ 1 paddle coincidence or ≥ 2 helical fiber clusters.
    A straight line through the straight fiber clusters must miss the paddle or helical fiber clusters by at least $\pi/8$.

An event may or may not fulfill each of these criteria, resulting in $2^{12} = 4096$ mutually exclusive classes. These classes are then tested with two sets of data, one containing only events from cosmic background and one generated by letting a known number of antiprotons annihilate in the trap. To each class, a merit rating is assigned based on the number of p-$\bar{p}$ annihilations compared to the number of cosmic events falling into this class. Classes with high merit ratings are mostly populated by p-$\bar{p}$ annihilation events while classes with low merit ratings are mostly populated by

cosmic events. A high merit rating therefore greatly reduces the cosmic background rate, but also discards a significant amount of the p-$\bar{p}$ annihilations which may look similar to cosmic particles. Arbitrary thresholds, or "cuts", are then applied. All events in classes with merit ratings higher than the threshold are accepted, the rest is discarded. The overall detection efficiencies versus background rates are plotted for a number of cuts in figure 6.11. Cut number 1 is the strictest, it provides the lowest background rate but also discards more than 90 % of the p-$\bar{p}$ annihilation events. Therefore strict cuts are not suitable when searching for a small number of events, for instance from trapped antihydrogen atoms. On the other hand, accepting too many events will strongly increase the background rate. Cut number 16 for instance has a detection efficiency about 14 % higher than cut number 13 (0.46 compared to 0.32), but its background rate is six times larger. The advantage of using position information to discard events caused by cosmic particles becomes obvious when comparing the cuts to the Trigger 1 and Trigger 2 event types also shown in figure 6.11. The cuts achieve the same detection efficiencies at much lower background rates.

6.4.3 Results

During the AD beam runs of 2010 and 2011, we performed a total of 11 antihydrogen production experiments with the infrared laser modulated by the chopper wheel. The particle numbers are identical to previous experiments, $5 \cdot 10^6$ $\bar{p}$ and $3 \cdot 10^8$ e^+ are used per trial. Five of these runs are control trials where the infrared laser is detuned from resonance. Two different arbitrary modulation frequencies are used, 9.3 Hz and 117 Hz. The longest time in the $\bar{H}$ formation chain is the 220 μs the cesium atoms need to travel from the laser excitation region to the center of the

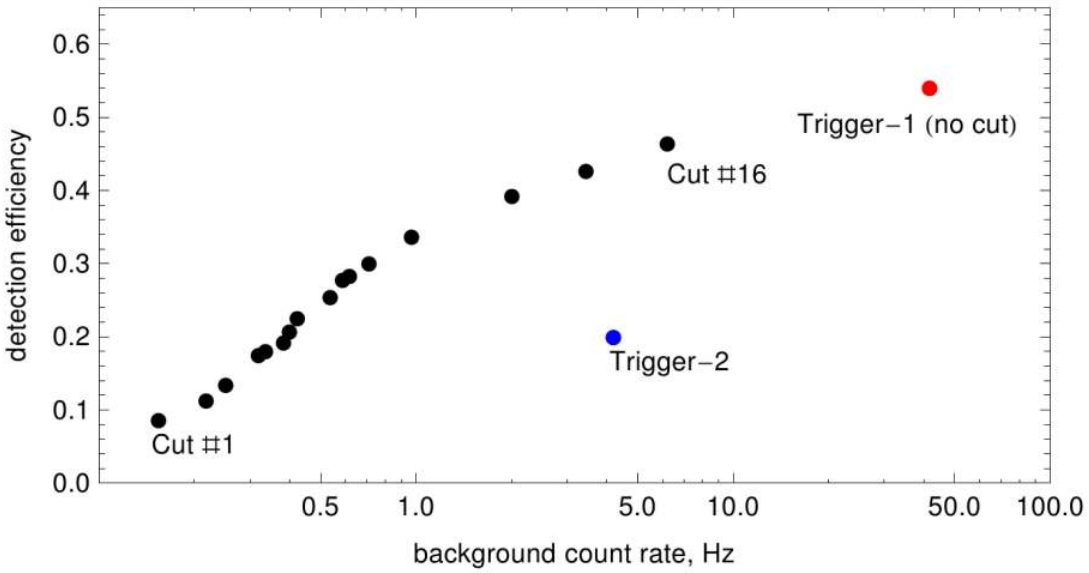

Figure 6.11: Antiproton detection efficiency versus background rate for a number of cuts. For reference, the Trigger 1 and -2 event types that use no position information are also shown.

trap. The modulation frequencies must be smaller than the value defined by this time: $(220\,\mu\mathrm{s})^{-1} = 4.5\,\mathrm{kHz}$. The runtimes are up to one hour with the full data acquisition system running the entire time. When holding large particle clouds of several $10^6\,\bar{p}$ for such long times, we always observe some losses. During an experiment, on average 10 % of the $5 \cdot 10^6$ $\bar{p}$ annihilate on the electrodes. When searching for antiproton annihilations in coincidence with the "laser-in" time slots, these losses cause the largest part of the background signal. Additional background from cosmic events is small in comparison. Therefore, a cut with a good detection efficiency and a relatively high rate for cosmic events can be applied. We use cut number 14 which has a detection efficiency for p-$\bar{p}$ annihilations of close to 40 % and a cosmic background rate of 2 Hz.

After applying the cut, the remaining events are sorted into two groups, depend-

ing on whether the infrared laser was blocked at the time of the event or not. The photodiode used to determine these time windows (figure 6.10) has a non-negligible rise time. Data points recorded while its signal is either rising or falling, plus a small additional safety margin, are discarded. Finally, the number of antiproton annihilations in all "laser-on" time frames is summed up and the corresponding number from the "laser-off" time frames is subtracted. The number of excess antiproton annihilations corresponds to antihydrogen atoms produced.

The results are displayed in figure 6.12. The individual runs are shown in subfigure (a), grouped by modulation frequency. Subfigure (b) shows weighted averages per modulation frequency and for all data points. The averages for both frequencies do not quite agree, but given the scatter of the individual data points, this may as well be a chance effect. The total average shows just above 2000 excess antiproton annihilations in coincidence with the infrared laser going into the trap. For the control trials, only the infrared laser is detuned from resonance while every other parameter is unchanged. This includes operation of the cesium oven and modulation of the lasers. If the infrared laser is detuned, no Rydberg excitation can take place and only ground state cesium atoms enter the trap regardless of whether the laser is blocked or not. Therefore no excess $\bar{p}$ annihilations should be observed. This is the case for all control trials, all of the points are consistent with zero.

The error bars are determined by the square root of the total counts per time bin. This background is caused by antiprotons being lost from their well. The rate of this loss process varies from trial to trial, therefore the error bars are also different. In some cases, the antiproton losses grew very large after $20-30$ minutes. This was often the case when experiments had to be run after the Ioffe trap had been quenched to look for trapped $\bar{H}$ atoms from TBR trials [62]. Therefore only the first 20 minutes of each run which show comparable plasma behavior are used

for figure 6.12. Those runs where the plasma remained stable for longer times show almost twice as many excess $\bar{p}$.

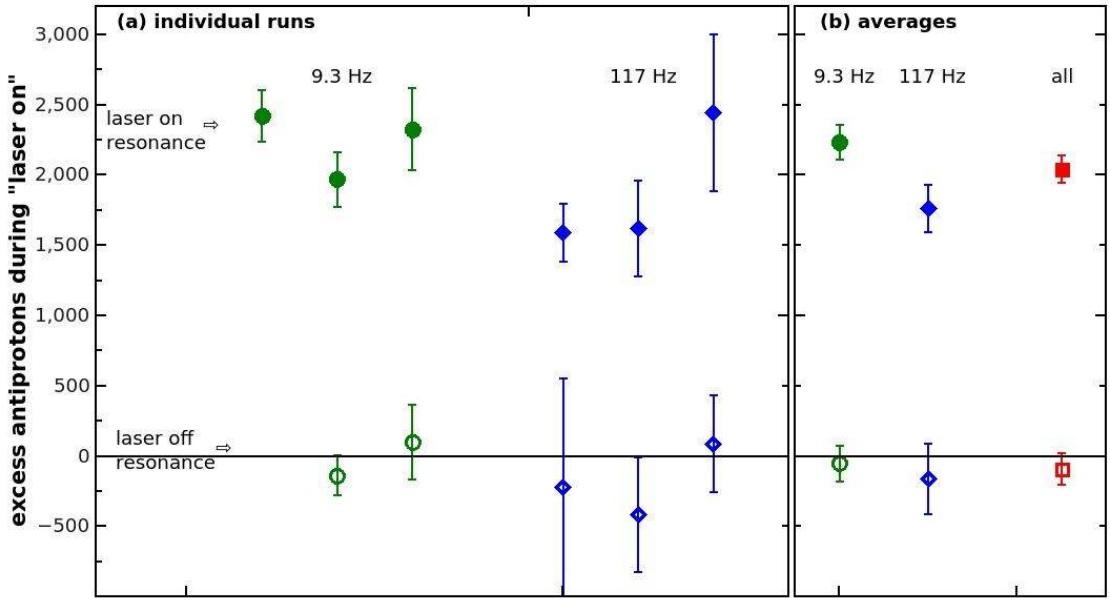

Figure 6.12: Results of antihydrogen experiments using the modulated laser detection (figure 6.10). The runtime for each point is 20 minutes. Two modulation frequencies are used: 9.3 Hz (green circles) and 117 Hz (blue diamonds). Full symbols indicate experiments with both lasers on resonance, while open symbols correspond to control trials with the infrared laser detuned from resonance. Graph (a) shows the individual runs while graph (b) displays weighted averages for both modulation frequencies and a weighted average of all data points (red squares). The overall average corresponds to just over 2000 antihydrogen atoms produced.

The expected number of antihydrogen atoms can be calculated from the cross section, equation (6.6), the density of the $\bar{p}$ plasmas, its diameter and the number of positronium atoms that interact with the antiprotons:

$$N_{\bar{H}} = \sigma_{\bar{H}}\, n_{\bar{p}}\, d_{\bar{p}}\, N_{Ps^*}\,. \tag{6.12}$$

Typical plasma densities and diameters are $n_{\bar{p}} = 10^{12}\,\mathrm{m}^{-3}$ and $d_{\bar{p}} = 10\,\mathrm{mm}$, respectively. The positronium trials found $4 \cdot 10^5\, Ps^*$ in the detection well after 20 minutes. The antihydrogen experiments use a factor of ten more positrons and a three times higher flux of cesium atoms and the number of Ps^* should scale appropriately. A correction has to be applied due to the different cross sectional areas: The plasma radius is 5 mm while the detection well strips Ps^* atoms up to a radius of 16 mm.

Inserting the numbers and considering a duty cycle of 50 % due to the chopper wheel gives an expected number of $\simeq 2400\,\bar{H}$ atoms, which is very close to the number observed. However, some estimates had to go into the calculation so the agreement should not be overrated.

The detection method assumes that charge-exchange production of antihydrogen is the only mechanism that produces antiproton losses in coincidence with the laser modulation. Any other process that would generate the same signature must have a turn-on time τ_{on} and turn-off time τ_{off} faster than the time constant of the modulation frequency: $\tau_{on/off} \ll (117\,\mathrm{Hz})^{-1} = 8.5\,\mathrm{ms}$. Also, to follow the same pattern, such a process must be triggered by the 852 nm laser. Thermal effects act on time scales much longer than a few ms. This can be seen for instance from the heating curve of the electrode stack by the cesium oven, figure 3.12. The lasers do not have a direct line of sight to the electrodes (see figure 3.11) and no heating of the stack is observed even from the 200 mW green laser. The infrared laser is operated at 5 mW, so a thermal effect from switching this power on and off can be safely excluded. A second possible effect is heating of the $\bar{p}$ plasma from secondary particles. Positronium atoms that form antihydrogen by charge-exchange collisions deposit electrons in the $\bar{p}$ plasma. If these electrons acquire high energies, they could transfer it to the antiprotons via collisions. This thermalization may happen

on a fast time scale [64], so it could explain an increase of the $\bar{p}$ loss rate. But in order to mimic charge-exchange production of $\bar{H}$, the loss rate must revert to background once the laser is blocked. Thus the energy added by the electrons must also be removed on the same time scale. The fastest process for energy loss of a mixed $\bar{p}$-e^- plasma is synchrotron radiation from the electrons, which, in a 1 T field has a time constant of 2.6 s, equation (6.5), much longer than the time scale of the laser modulation. Therefore insertion of energetic electrons could continuously heat the $\bar{p}$ plasma, but it cannot mimic modulated antihydrogen production with a ms time constant.

We therefore conclude that the data of figure 6.12 shows the production of an average of 2000 antihydrogen atoms in 20 minute trials. In single longer runs, up to twice as many $\bar{H}$ were observed. Also, since most of the initial particles are retained in the first 20 minutes of each trial, it seems safe to assume that removing the chopper wheel and sending the lasers in continuously would again double these numbers. However, verification requires an alternative detection method. The double charge-exchange is thus suitable to produce comparable numbers of $\bar{H}$ as the only production method established so far, the three-body recombination.

Chapter 7

Conclusion

At the beginning of this work, charge-exchange production of antihydrogen had only been demonstrated once with less than 20 $\bar{H}$ atoms produced per trial [126]. During this thesis, we could demonstrate an increase of this number by two orders of magnitude, an average of 2000 antihydrogen atoms are produced per experiment. Removing the chopper wheel needed for detection would likely double this number again. This work therefore shows that the double charge-exchange is capable of producing the same quantities of antihydrogen than the established method of three-body recombination. In contrast to the TBR production of $\bar{H}$, the charge-exchange method does not require any drives or modifications of the potential structures that would heat the particles. Especially the heavy antiprotons remain at rest the entire time. Therefore the fraction of cold, trappable $\bar{H}$ atoms is expected to be much larger.

The increased number was made possible by numerous advancements in the tools and methods available. ATRAP's second generation combined Penning-Ioffe trap allows loading and manipulation of much larger antimatter plasmas than before.

Up to 10^7 antiprotons and $4 \cdot 10^9$ positrons can be loaded at a time. Using the field boosting solenoid and the rotating wall technique, these particle clouds are accumulated on reasonable time scales on the order of hours or below. The large capacity cesium sources used in this new apparatus and the greatly improved laser excitation efficiency allowed us to perform experiments for months at a time without warming up the trap and breaking vacuum. The thorough thermal insulation of the cesium oven minimized the heat load on the cryogenic electrode stack and enabled experiments with runtimes of more than one hour.

The new 511 nm laser system developed for this work provides several major improvements. Its continuous-wave operation produces a steady stream of Rydberg cesium atoms. Due to the narrow linewidth, all of its output power is usable for laser excitation. The most important feature however is the laser's wide tunability. The various factors contributing to the efficiency of the charge-exchange process were first investigated during this work. We found that the overall efficiency strongly depends on the choice of the Rydberg state and a tunable laser allows us to excite to the optimum state. The laser's mode-jump free scan range of 20 GHz enables us to easily find the transition frequencies once their approximate location is calculated.

We used two different methods to estimate the cesium energy levels in the strong magnetic fields of our trap, both of which yield good agreement with experimental data. The two methods complement each other. For lower magnetic fields, or lower n-states, a direct diagonalization of the Hamiltonian is more accurate while for stronger fields or higher n-states, a semi-classical estimate is more appropriate. Previous work on Alkali Rydberg atoms in strong magnetic fields dates back 30 years and used pulsed laser with GHz resolution. During this work, we could accurately measure the cesium energy levels, but focusing on $\bar{H}$ experiments only allowed us to probe a small range of the spectrum. The laser system has shown

reliable performance over the last years and the green laser's output power could be significantly increased during this time.

We achieved a gain by a factor of 500 in the production of positronium. Most of this is due to the larger number of positrons available now, but we could also increase the efficiency by a factor of three. Using laser modulation to monitor the production of antihydrogen allowed us to detect the larger numbers of $\bar{H}$ atoms produced during this work.

The next steps will be to include ATRAP's adiabatic cooling technique to reduce the $\bar{p}$ temperature and to repeat these experiments within the field of a Ioffe tap to confine the $\bar{H}$ atoms produced. Some of the ground work could already be prepared during this thesis. We demonstrated laser excitation of cesium atoms within the inhomogeneous magnetic field of a neutral atom Ioffe trap. The magnetic gradient causes a broadening of the transition lines, but causes no further complications. The calculations to estimate the cesium energy levels are also applicable in this case. We already performed several trial experiments for Ps and $\bar{H}$ formation in the Ioffe field, but due to time constraints, these could not advance enough to deliver results.

With adiabatically cooled $\bar{p}$ at 3.5 K, about 150 $\bar{H}$ atoms should be trapped per trial. This would correspond to an increase by a factor of 30 compared to numbers obtained by the TBR method so far. This would be an important step towards the 1000 trapped $\bar{H}$ atoms suggested for spectroscopy [79].

ATRAP is currently commissioning a new apparatus named CTRAP. It features a combined quadrupole-octopole Ioffe trap with a much shorter turn-off time. This will significantly reduce the background signal when looking for trapped antihydrogen atoms. The new trap required a re-design of the components for producing a cesium beam in the apparatus. So after commissioning of the new apparatus, the charge-exchange experiments will be continued.

Appendix A

Laser Control Software

The structure of the laser control software is described in section 4.4. It is an object oriented design where each module is largely independent. This allows fast extension to include additional lasers and easy adaption of new hardware components. This section explains the functionality with the help of screenshots of the graphical user interface (GUI).

Figure A.1 shows a screenshot of the main window. Currently, the program is compiled with two PID modules labeled *"Laser 1"* and *"Laser 2"*. Four input fields for each PID controller allow the user to enter the gain parameters, proportional (P), integral (I) and differential (D) and the target frequency for the laser in THz. All values are changeable during operation. The values are automatically saved when the program is terminated and restored at the next launch. The two lower fields display information gathered and calculated by the program. The one labeled *"Actual"* displays the value currently read by the PID controllers *Input* modules, in this case the laser frequencies measured by the wavemeter. The field *"Output"* shows the correction signal calculated by the controller and sent to its *Output* module. In

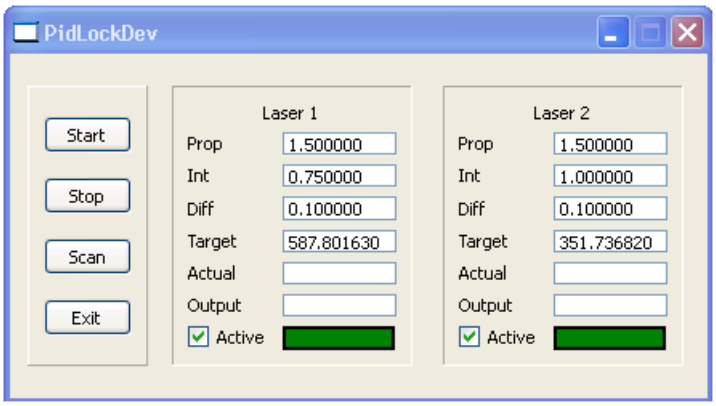

Figure A.1: Main window of the laser control software.

the current configuration this corresponds to the voltage supplied by the analog output channel of the multipurpose measurement card.

The checkbox *"Active"* allows to (de)activate each controller separately without disturbance to the other one. The green square provides optical feedback to the user. If the laser frequency deviates too much from the target value, for instance because a mode jump occurred, the square turns red.

The *"Start"* button on the left initiates an internal timer which triggers every active PID controller once every 100 ms. The *"Stop"* button interrupts this timer. The button labeled *"Scan"* opens the scan-window shown in figure A.2.

The scan-window is already initiated when the program starts but remains invisible until activated. It provides several modes of data acquisition. The simplest one is chosen by selecting *"External Ramp"*. In this mode, the program records data from all active channels at the given interval. This is used for instance to log the laser parameters during charge-exchange experiments when the laser frequencies are locked to the cesium resonances. If the laser frequency is ramped by an external function generator, this mode is also suitable to gather data from spectroscopy. The

program can also emulate its own function generator. The mode *"Locked Scan"* uses one of the PID regulators to ramp a laser. The advantage compared to a function generator is that the upper and lower frequencies can be directly set in the program.

Both modes are compatible with the *"Trigger"* option. If activated, the program waits until the signal of the selected channel rises above a set threshold before starting to record. This option was implemented for long automated measurements testing the capacity of our cesium ovens. A function generator periodically turned on the current through a *Cs* oven installed in a test chamber for several minutes at a time with long cooldown cycles in between. The fluorescence from the infrared laser was recorded to measure how much cesium the oven was emitting and by how much the amount decreased over several hundred cycles. These measurements took a few days and using the trigger-function allowed us to completely automate them and only record data while the oven was running.

Usually, data acquisition must be stopped manually. The field *"Runtime"* also allows to set a time after which the recording terminates automatically. A value of zero is interpreted as infinity.

Currently, the program reads more than 20 input channels. Since many of them are not needed for every run, they can be (de)activated individually. Also, a name can be assigned to each channel which will be added to the top of each data column. When a recording is started, the data from each active channel is written to the large text box and, if *"Save to File"* is selected, to the hard drive. The data is written continuously so in case of a power failure or a computer crash only the last set of values is lost. The filename is automatically generated. The first part is the date and time when the measurement was started. If a custom name is entered in the *"Filename"* field, it is appended to the time stamp.

The button *"Done"* hides the scan window from view if it isn't needed any more.

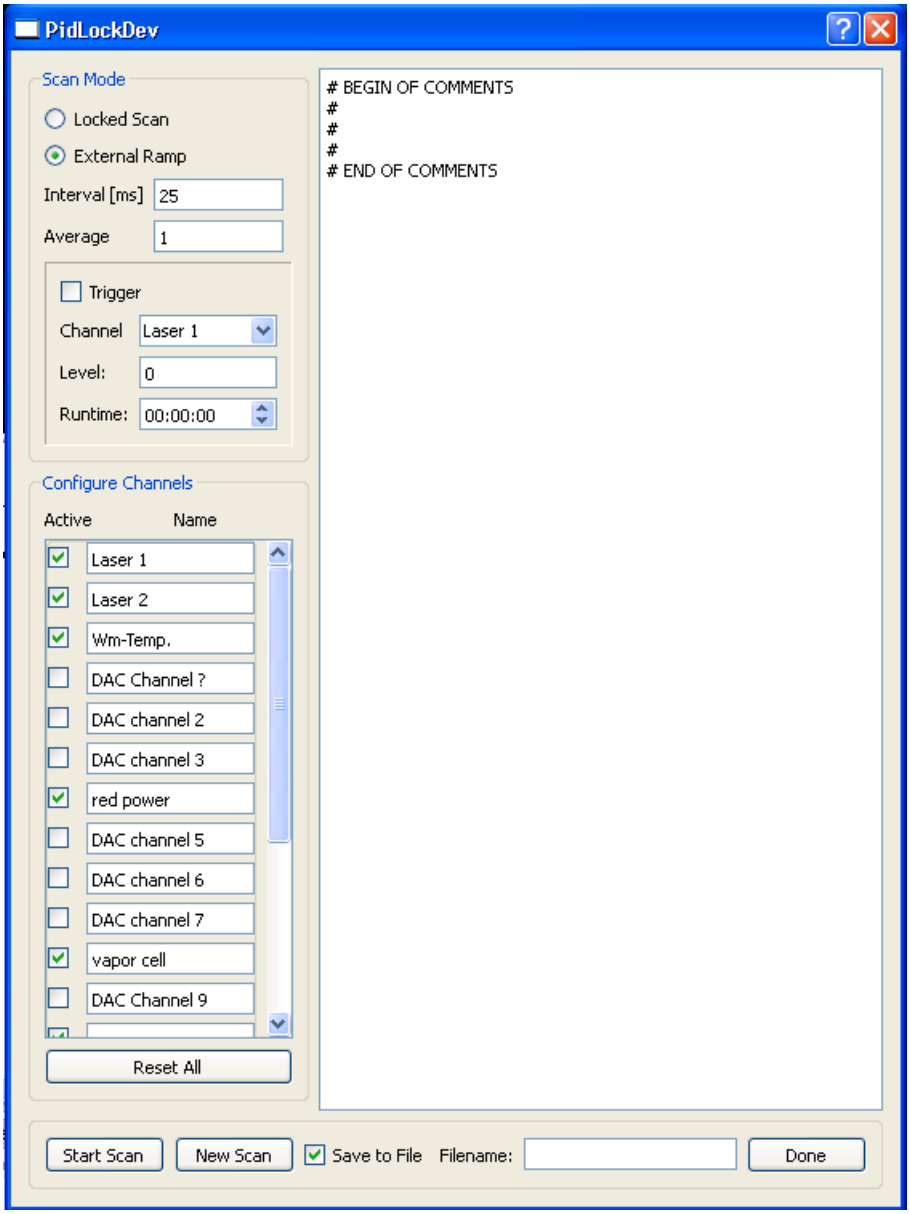

Figure A.2: The data acquisition module.

Appendix B

Calculation of Rydberg Energy Levels

This chapter contains the source code for the calculation of Rydberg energy levels by the two methods described in section 5.1.4. Section B.1 lists the code for the matrix diagonalization while section B.2 contains a Mathematica file that implements the semiclassical method.

B.1 Matrix Diagonalization

The program is written in C++ and requires the Gnu Scientific Library (gsl) [1]. The calculations are contained in the file *main.cpp*. *WaveFunctions.cpp* provides numerically calculated expectation values for the spherical harmonics $Y_l^m(\theta, \phi)$ and the radial hydrogen wave functions $R_{nl}(r)$. Numerical integration of the radial term for high values of n and l fails due to their oscillatory behavior, but they can be calculated from analytical formulas [54, 83]. This is done in *RadialAnalytics.cpp*.

main.cpp

```
1   // RYDBERG ENERGY LEVELS
2   //
3   // Created on: Sep 26, 2010
4   // Author: Andreas Muellers
5   //
6   // Programm to estimate cesium Rydberg energy levels in a magnetic field. A
7   // Hamiltonian is set using energy levels from quantum defect theory and the
8   // operators for dia- and paramagnetic shifts combined with Hydrogen wave-
9   // functions. Spin-Orbit coupling is neglected. Eigenvalues and eigenvectors of
10  // this Hamiltonian are calculated.
11  // The Hamiltonian consists of three parts: H = H_0 + H_Para + H_Dia
12  // H_0 delivers know energy values (quantum-defect-theory) and H_Para causes a
13  // shift in the energy levels proportional to B. These two terms have diagonal
14  // contributions only whereas H_Dia adds to off-diagonal elements too, since the
15  // magnetic field mixes states of |l1-l2| = 2. The diamagnetic term requires the
16  // expectation value <n1,l,m1| r^2 sin^2(\theta) |n2,l2,m2>, which separates into
17  // a radial and an angular part.
18  //
19  // The angular part is calculated using numerical integration routines provided by
20  // the gnu scientific library (GSL). The angular wavefunctions are the spherical
21  // harmonics. Since the integration over \phi is not affected, only elements with m1=m2
22  // contribute and the expansion to complex numbers can be avoided. The associated
23  // Legendre polynoms are also provided by GSL. While the integration is performed in the
24  // main routine, the function evaluation is capsuled in the module "WaveFunctions".
25  // This module also provides the zero-field quantum defect energy levels and numerical
26  // values for the radial part of the wavefunction, but due to the highly oscillatory
27  // behavior, the numerical integration routines of the GSL fail for the regions of
28  // interest. Therefore, analytic expressions are used to calculate the radial matrix
29  // elements of interest. This is done in the module "RadialAnalytics".
30  //
31  // Both modules are static, meaning that they calculate the angular wave functions,
32  // energy levels and radial matrix elements for all states between n=10 and n=70,
33  // regardless of how many of these are actually needed. Changing this would require
34  // dynamic multidimensional data-storage, but since these calculations do not take
35  // long, the drawback is minimal. The demanding calculations are all performed in the
36  // main program which only runs for the requested number of states. First and last
37  // state and the magnetic field are entered each time the program runs.
38  //
39  // The main program stores the hamiltonian in a GSL-matrix and uses the library routines
40  // to calculate eigenvalues and eigenvectors. The eigenvalues are printed to the standard-out
41  // whereas the eigenvectors are written to the file eigenvectors.dat.
42
43  #include <stdio.h>
44  #include <math.h>
45  #include <cstring>
46  #include <iostream>
47  #include <fstream>
48  #include <gsl/gsl_integration.h>
49  #include <gsl/gsl_matrix.h>
50  #include <gsl/gsl_vector.h>
```

```
51  #include <gsl/gsl_eigen.h>
52  #include "WaveFunctions.h"
53  #include "RadialAnalytics.h"
54
55  WaveFunctions *Wave1;
56  WaveFunctions *Wave2;
57  RadialAnalytics *Radial;
58  gsl_matrix *MatrixElements;
59  gsl_matrix *EigenVectors;
60
61  int nStart = 36;
62  int dn = 10;
63
64  /* constant numerical factors */
65  const double AUtoMHz = 6579683920.722; //conversion factor atomic units to MHz
66  const double TESLAtoAU = 1./(2.350517e5); //conversion factor Tesla to a.u.
67  const double muB = 0.5; //Bohr magneton in atomic units
68  const double ge = 2.002319; //electron g-factor
69  //Cs frequencies: Can be used to convert output to frequency for the green laser
70  const double nuIon = 9.415422145882682e+14; // Cs ionization energy in Hz
71  const double nu1 = 351.7368e+12; // frequency for first transisiton 6S-6P in 1T field
72  const double n6S = 17.2733e+9; //ground state energy level
73
74  double SphHarm(double x, void *parameters)
75  {
76    double result = 0.;
77    if ( (Wave1->getM() == Wave2->getM())
78        && abs(Wave1->getL()-Wave2->getL()) <= 2
79        && Wave1->getM() <= Wave1->getL()
80        && Wave2->getM() <= Wave2->getL() )
81    {
82      result = pow(sin(x),3) * Wave1->getSphericalHarmonic(cos(x)) *
            Wave2->getSphericalHarmonic(cos(x));
83    }
84    return (result);
85  }
86
87  int getIndexij(int n, int l, int m)
88  {
89    int index = 0;
90    for (int k = nStart; k <= n; k++)
91    {
92      index += floor((k-1)/2)*2;
93    }
94    index += 2 * floor(l/2);
95    index += m;
96    index -= nStart;
97    index -= 2;
98    return(index);
99  }
100
101 double linearShift(int m, double B)
```

```
102  {
103    double result = muB * B * TESLAtoAU *(m + ge*(2.5-m));
104    return (result);
105  }
106
107  int main()
108  {
109    /* read input and check parameters */
110    double B = 1.;
111    bool InputComplete = false;
112    printf("Calculate Cesium Rydberg-energy-levels in a magnetic fields. \n States available
           between n=10 and n= 70.\n");
113    while (InputComplete == false)
114    {
115      printf("Enter first n-state (range: 10-70): ");
116      std::cin >> nStart;
117      if ( !(nStart >= 10 && nStart <= 70) ){
118        InputComplete = false;
119        nStart = 20;
120        printf("Input error: first n set to 20.\n");
121      }
122      int nLast;
123      printf("Enter last n-state (range: %2i-70): ",nStart);
124      std::cin >> nLast;
125      if ( !(nLast > nStart && nLast <= 70))
126      {
127        nLast = 50;
128        printf("input error: last n set to 50.\n");
129      }
130      dn = nLast-nStart;
131      printf("Enter magnetic field in Tesla: ");
132      std::cin >> B;
133      printf("\n Input complete: Use levels from n=%2i to n=%2i and B=%5fT. \n Proceed?
             Y/N\n",nStart,nLast,B);
134      char in;
135      std::cin>>in;
136      if (in == 'Y' || in == 'y')
137        InputComplete = true;
138    }
139
140    // Initialize
141    Wave1 = new WaveFunctions();
142    Wave2 = new WaveFunctions();
143    Radial = new RadialAnalytics();
144    int dim = getIndexij(nStart+dn+1, nStart+dn-1,3);
145    MatrixElements = gsl_matrix_calloc(dim,dim);
146    EigenVectors = gsl_matrix_calloc(dim,dim);
147
148    /* make Spherical Harmonics Table */
149    // Using integration routines from the Gnu Scientific Library (GSL)
150    gsl_integration_workspace *workspace = gsl_integration_workspace_alloc(1e7);
151    double result, error;
```

```
152     gsl_function F;
153     F.function = &SphHarm;
154
155     printf("integrating spherical harmonics...\n");
156     double Spherical[nStart+dn+1][2][nStart+dn+1][2];
157     for (int l1 = 2; l1 <= nStart+dn; l1+=2)
158     {
159       for (int l2 = 2; l2 <= nStart+dn; l2+=2)
160       {
161         for(int m1 = 2; m1 <= 3; m1++)
162         {
163           for (int m2 = 2; m2 <= 3; m2++)
164           {
165             if (abs(l1-l2)<=2 && m1 <= l1 && m2 <= l2) //select states of interest
166             {
167               Wave1->setLM(l1,m1);
168               Wave2->setLM(l2,m2);
169               gsl_integration_qag(&F, 0,M_PI, 0, 1e-4, 1000, GSL_INTEG_GAUSS61, workspace,
                      &result, &error);
170               Spherical[l1][m1-2][l2][m2-2] = result;
171             } //if
172             else
173             {
174               Spherical[l1][m1-2][l2][m2-2] = 0.;
175             } // else
176           } //for m2
177         } // for m1
178       }//for l2
179     } //for l1
180
181     double buffer = 0.;
182
183     /* set matrix elements */
184     printf("setting matrix elements...\n");
185     printf("\t diagonal\n");
186     /* diagonal elements */
187     for (int n = nStart; n <= nStart+dn; n++)
188       for (int l = 2; l < n; l+=2)
189         for (int m = 2; m <= 3; m++)
190         {//diagonal elements
191           buffer = gsl_matrix_get(MatrixElements,getIndexij(n,l,m), getIndexij(n,l,m));
192           buffer += Wave1->getEnergyLevel(n,l) + linearShift(m, B);
193           gsl_matrix_set(MatrixElements, getIndexij(n,l,m), getIndexij(n,l,m), buffer);
194           //printf("%2i, %2i: %5e\n ",n,l,
                  gsl_matrix_get(MatrixElements,getIndexij(n,l,m),getIndexij(n,l,m)) );
195         }
196
197     printf("\t off-diagonal\n");
198     /* off-diagnonal elements */
199     for (int n1 = nStart; n1 <= nStart+dn; n1++) {
200       for (int n2 = nStart; n2 <= nStart+dn; n2++) {
201         for (int l1 = 2; l1 < n1; l1 += 2 ) {
```

```
202           for (int l2 = 2; l2 < n2; l2+= 2) {
203             for (int m = 2; m <= 3; m++)
204             {
205               if (fabs(l1-l2)<= 2)
206               { //off-diagonal
207                 buffer = gsl_matrix_get(MatrixElements,getIndexij(n1,l1,m), getIndexij(n2,l2,m));
208                 buffer +=  ( 1./8. * (B* TESLAtoAU)*(B* TESLAtoAU) * Spherical[l1][m-2][l2][m-2]
                        * Radial->getRsqElement(n1,n2,l1,l2) ) ;
209                 gsl_matrix_set(MatrixElements, getIndexij(n1,l1,m), getIndexij(n2,l2,m), buffer);
210               } // if off-diagonal
211             }// for m
212           } // for l2
213         }//for l1
214       }//for n2
215     }//for n1
216
217     std::ofstream File0("MatrixElements.dat");
218       for (int i = 0; i < dim; i++) {
219         for (int j = 0; j < dim; j++) {
220           //printf("%5e ", gsl_matrix_get(MatrixElements,i,i) );
221           File0<<gsl_matrix_get(MatrixElements,j,i)<<" ";
222         }
223         //printf("\n");
224         File0<<"\n";
225       }
226       printf("MatrixElements written to 'MatrixElements.dat'.\n");
227
228     /* diagonalizing the matrix */
229     printf("calculating eigenvalues...\n");
230     gsl_vector *eigenvalues = gsl_vector_alloc(dim);
231     gsl_eigen_symmv_workspace *w = gsl_eigen_symmv_alloc(dim);
232     gsl_eigen_symmv(MatrixElements, eigenvalues, EigenVectors, w);
233     gsl_eigen_symmv_free(w);
234     printf("Done!\n");
235
236     /* output */
237     std::ofstream File1("eigenvalues.dat");
238     for (int i = 0; i < dim; i++) {
239       File1<<(gsl_vector_get(eigenvalues,i))<<"\n";
240     }
241     printf("Eigenvalues written to 'eigenvalues.dat'.\n");
242
243     std::ofstream File2("eigenvectors.dat");
244     for (int i = 0; i < dim; i++) {
245       for (int j = 0; j < dim; j++) {
246         //printf("%5e ", gsl_matrix_get(MatrixElements,i,i) );
247         File2<<gsl_matrix_get(EigenVectors,i,j)<<" ";
248          //printing values of interest
249         if (gsl_matrix_get(EigenVectors,i,j)*gsl_matrix_get(EigenVectors,i,j) > 0.8)
250           printf("%4i,%4i\n",i,j);
251
252       }
```

```
253       //printf("\n");
254       File2<<"\n";
255     }
256     printf("Eigenvectors written to 'eigenvectors.dat'.\n");
257     printf("indices for (n,2,2) levels:\n");
258     for (int n = nStart; n <= nStart+dn; n++)
259       printf("%2i, %6i\n", n, getIndexij(n,2,2));
260     return (0);
261   }
```

WaveFunctions.cpp

```
1   /*  WaveFunctions.cpp
2   *
3   *  Created on: Oct 2, 2010
4   *  Author:Andreas Muellers
5   *
6   *  This module provides numerical values for the spherical Y_lm(\theta, \phi) and
7   *  the radial probability part of hydrogen wavefunctions P_n,l(r) for given n,l,m.
8   *  The normalization coefficients independent of the variables r, \theta and
9   *  \phi are calculated on startup to minimize the calculations during runtime.
10  *  This will speed up frequent access as needed for numerical integration.
11  *  Also, a lookup-table for the faculty function is provided.
12  *
13  *  Since this module is meant for numerical integration of pairs of wavefunctions,
14  *  the complex part of the spherical harmonics is not given explicitely. Only the
15  *  phase factor exp(-im\phi) is complex which evaluates to the delta function of
16  *  m1 and m2 when integrating a pair. Only the real part of one wavefunction is
17  *  returned, the orthogonality in m has to be ensured externally. This means that
18  *  the spherical-function returns the associated Legendre polynom and the according
19  *  normalization factor.
20  *  Also, the factors for one wants to compute the expectation values (in this case
21  *  sin^2(\theta) and r^2) are not given here but have to be multiplied externally.
22  *  The angular function expects not \theta but cos(\theta) as argument.
23  *
24  *  Two access functions are provided for both radial and angular elements:
25  *  One that only supplies the variable (r or cos(\theta)) and one that
26  *  additionally provides the quantum numbers n,l and l,m, respectively.
27  *  In the first case, these quantum numbers are taken from an internal variable
28  *  which can be set and read by access functions. Providing the quantum numbers
29  *  to the access function does not change the value of the internal variables.
30  *
31  *  The module also provides quantum defect energy levels for the cesium atom.
32  *  Since only even l-states starting from l=2 are originally of interest, only
33  *  these qd-values are provided. The coefficients are stored in an array, so the
34  *  extension to other states is trivial. The result is provided as the energy
35  *  below ionization in atomic units.
36  *
37  *  The module is static, it always calculates a lookup-table of all normalization
38  *  factors between two n-values given by preprocessor values.
39  */
40
```

```
41 #include "WaveFunctions.h"
42 #include <gsl/gsl_sf_legendre.h>
43 #include <gsl/gsl_math.h>
44 #include <math.h>
45 #include <stdio.h>
46
47 WaveFunctions::WaveFunctions()
48 {
49   n = 0;
50   l = 0;
51   m = 0;
52   //calculate lookup-tables
53   makeFaculty();
54   makeNormalizationSph();
55   makeNormalizationRad();
56 }
57
58 /* access function for internal quantum numbers */
59 void WaveFunctions::setN(int newN)
60 {
61   this->n = newN;
62 }
63
64 /* get- and set-functions
65 *  only examples are shown here
66 void WaveFunctions::setN(int newN)
67 {
68   this->n = newN;
69 }
70
71 int WaveFunctions::getN()
72 {
73   return(this->n);
74 }
75 // analogous functions for quantum numbers l,m and combined functions
76
77 /****************************************
78 *      NORMALIZATION          *
79 ****************************************/
80
81 void WaveFunctions::makeNormalizationSph()
82 {
83   for (int l = 0; l <= NMAX; l++) {
84     for (int m = 0; m <= NMAX; m++) {
85       NormalizationTableSph[l][m] = 0.;
86       if (m <= l)
87       {
88        NormalizationTableSph[l][m] = sqrt((2*l+1) * getFaculty(l-m) / (2. * getFaculty(l+m) ));
89       }
90     }
91   }
92 }
```

```
93
94  double WaveFunctions::getNormalizationSph(int l, int m)
95  {
96    if( l <= NMAX && m <= NMAX){
97      return(NormalizationTableSph[l][m]);
98    }
99    else
100   {
101     return (0.);
102   }
103 }
104
105 void WaveFunctions::makeNormalizationRad()
106 {
107   for (int i = NMIN; i <= NMAX; i++) {
108     for (int j = 0; j < NMAX; j++) {
109       NormalizationTableRad[i-NMIN][j] = 0.;
110       if (l < n) {
111         NormalizationTableRad[i-NMIN][j] = sqrt(getFaculty(i-j-1) * getFaculty(i+j) / (i*i));
112       }
113     }
114   }
115
116 }
117
118 double WaveFunctions::getNormalizationRad(int n, int l)
119 {
120   if (n >= NMIN && n <= NMAX && l <= NMAX){
121     return(NormalizationTableRad[n-NMIN][l]);
122   }
123   else
124   {
125     return(-1.);
126   }
127 }
128
129 /****************************************
130 *   FACULTY      *
131 ****************************************/
132
133 double WaveFunctions::faculty(int k)
134 {
135   double result = 1;
136   for (int i = 1; i <= k; i++) {
137     result *= i;
138   }
139   return(result);
140 }
141
142 void WaveFunctions::makeFaculty()
143 // generates a lookup-table for values of k!
144 {
```

```
145     for (int k = 0; k <= 3*NMAX; k++) {
146       FacultyTable[k] = faculty(k);
147     }
148   }
149
150   double WaveFunctions::getFaculty(int index)
151   {
152     if (index <= 3*NMAX)
153     {
154       return (FacultyTable[index]);
155     }
156     else
157     {
158       return (-1.);
159     }
160   }
161
162   /*****************************************
163   *    Spherical Harmonics Sq       *
164   *****************************************/
165
166   double WaveFunctions::getSphericalHarmonic(double cosTheta)
167   {
168     return(getSphericalHarmonic(this->l,this->m,cosTheta));
169   }
170
171   double WaveFunctions::getSphericalHarmonic(int l, int m, double cosTheta)
172   {
173     double result = gsl_sf_legendre_Plm(l,m, cosTheta) ;
174     result *= getNormalizationSph(l,m);
175
176     return(result);
177   }
178
179   /*****************************************
180   *      Radial Sq          *
181   *****************************************/
182
183   double WaveFunctions::getRadial(double r)
184   {
185     return( getRadial(this->n, this->l,r) );
186   }
187
188   double WaveFunctions::getRadial(int n, int l, double r)
189   {
190
191     double result = 0.;
192     //sum-part
193     for (int k = 0; k <= n-l-1; k++)
194     {
195       result +=  ( pow(-2*r/n,k) / ( getFaculty(k) * getFaculty(n-l-k-1) * getFaculty(2.*l+k+1) )
           ) ;
```

```
196     }
197     result *= ( pow(2*r/n,l+1) * exp(-r/n) ); // r-dependent factors
198     result *= getNormalizationRad(n,l);
199     return(result);
200   }
201
202   /****************************************
203   *    Zero Field Energy Levels     *
204   ****************************************/
205
206   double WaveFunctions::getEnergyLevel(int n, int l)
207   {
208     //Quantum Defect Coefficients for the d-State
209     /* initialize table for coefficients */
210     double ConstD[6][6];
211     for (int i = 0; i < 6; i++)
212       for (int j = 0; j < 6; j++)
213         ConstD[i][j] = 0;
214
215     /* set coefficients
216      * Using data from Weber and Sansonetti, PRA (1987) 35, 4650
217      * Other coefficients can be added when needed.
218      */
219     /* d-states */
220     ConstD[2][0] = 2.46631524;
221     ConstD[2][1] = 0.0133577;
222     ConstD[2][2] = -0.37457;
223     ConstD[2][3] = -2.1867;
224     ConstD[2][4] = -1.5532;
225     ConstD[2][5] = -56.6739;
226     /* g-states */
227     ConstD[4][0] = 0.00703865;
228     ConstD[4][1] = -0.049252;
229     ConstD[4][2] = 0.01291;
230     //calculate the correction term for the principal quantum number n
231     double nCorr = 0.;
232
233     if (l < 6) { /* consider quantum defects */
234       double factorSq = (n-ConstD[l][0])*(n-ConstD[l][0]); //(n-AD)^2
235       double factorK = factorSq; //will store (n-AD)^k
236       nCorr = ConstD[l][0];
237       for (int i = 1; i <= 5; i++)
238       {
239         nCorr += ConstD[l][i]/factorK;
240         factorK*=factorSq;
241       }
242     }
243     //calculate the energy level
244     double EnergyLevel = -0.5; //negative Cs Ionization energy in a.u.;
245     EnergyLevel = EnergyLevel/((n - nCorr)*(n-nCorr));
246     return(EnergyLevel);
247   }
```

RadialAnalytics.cpp

```
1  /*
2   *  RadialAnalytics.cpp
3   *
4   *  Created on: Oct 2, 2010
5   *  Author:Andreas Muellers
6   *
7   *  This class calculates radial matrix elements for <r^2> using analytic
8   *  relations provided in:
9   *  A: Enciso-Aguilar et al, EJTP 13 (2006) 117   (for elements with n1 = n2)
10  *  B: Hey, J. Phys. B 39 (2006) 2641        (for elements with n1 != n2)
11  *
12  *  Source B provides recursive relations for the matrix elements starting from
13  *  the elements with highest l, but they have to be derived specifically for
14  *  each combination of delta-l = l1-l2 and r^k. Originally of interest are
15  *  elements for delta-l = {-2,0,2} (quadrupole moments) and r^2. The equations
16  *  required for these are provided in B. The calculation of the quadrupole
17  *  moments requires the dipole moments (delta-l = 1), so they have to be
18  *  calculated first. These calculations all happen by the same scheme: A start-
19  *  equation provides the element with highest l for a given n1 and n2. Using
20  *  this, one or two recursive relations traverse down to the lowest l. Each
21  *  calculation function automatically stores its result in the appropriate array.
22  *  Although source A is in principle able to provide elements for all combinations
23  *  of delta-l and r^k, the calculation is limited to the same set as above.
24  *
25  *  In its current version, the module calculates all elements from n=10 to n=70,
26  *  regardless whether they are needed or not. Variables and functions for dynamic
27  *  initialisation are provided, but dynamic multidimensional data-storage is not
28  *  included.
29  */
30
31 #include <math.h>
32 #include <stdio.h>
33 #include "RadialAnalytics.h"
34
35 RadialAnalytics::RadialAnalytics()
36 { /*  constructor with parameters: pre-processor
37    *  values for NSTART and DN are copied to
38    *  local variables. This allows easy change
39    *  in case this module is expanded to run
40    *  dynamically.
41    */
42   nStart = NSTART;
43   dn = DN;
44   makeElements();
45 }
46
47 RadialAnalytics::RadialAnalytics(int nStart, int dn)
48 {
49   /* constructor with parameters: for future use */
50   this->nStart = nStart;
```

```
51    this->dn = dn;
52    makeElements();
53  }
54
55  void RadialAnalytics::makeElements()
56  {
57    /* iterates over the whole range of given n
58     * and triggers calculation of the corresponding
59     * submatrices for each pair of n1 and n2.
60     * Different routines are used for symmetric (n1=n2)
61     * and asymmetric matrices (see above).
62     */
63    for (int n1 = NSTART; n1 <= NSTART+DN; n1++)
64      for (int n2 = NSTART; n2 <= n1; n2++)
65      {
66        if (n1==n2)
67        {
68          makeSymmetricElements(n1);
69        }
70        else
71        {
72          makeDipoleElements(n1,n2);
73          makeQuadrupoleElements(n1,n2);
74        }
75      }
76  }
77
78  /* set functions */
79
80  /* internal set functions to access the arrays used for data-storage. They
81   * internally shift the indices of the actual wavefunction n,l to the ones
82   * used for data storage.
83   */
84  void RadialAnalytics::setR1(int n1, int n2, int l1, int l2, double value)
85  {
86    DipoleElements[n1-NSTART][n2-NSTART][l1][l2] = value;
87  }
88
89  void RadialAnalytics::setR2(int n1, int n2, int l1, int l2, double value)
90  {
91    QuadElements[n1-NSTART][n2-NSTART][l1][l2] = value;
92  }
93
94  /* get functions */
95
96  /* Data access functions: The first one is public for internal use,
97   * the other two are meant for internal use only.
98   */
99  double RadialAnalytics::getRsqElement(int n1, int n2, int l1, int l2)
100 {
101   return ( getR2(n1,n2,l1,l2) );
102 }
```

```
103
104 double RadialAnalytics::getR1(int n1, int n2, int l1, int l2)
105 {
106   return (DipoleElements[n1-NSTART][n2-NSTART][l1][l2]);
107 }
108
109 double RadialAnalytics::getR2(int n1, int n2, int l1, int l2)
110 {
111   return (QuadElements[n1-NSTART][n2-NSTART][l1][l2]);
112 }
113
114 /* calculations */
115
116 /* Calculation of the A_n,l coefficient used
117  * in source B (see above).
118  */
119 double RadialAnalytics::A(int n, int l)
120 {
121   double value = sqrt( (n-l)*(n+l) );
122   value *= 1./(n*l);
123   return (value);
124 }
125
126 /*  SYMMETRIC ELEMENTS
127  *   Calculations follow source A */
128
129
130 /* iteration function */
131 void RadialAnalytics::makeSymmetricElements(int n)
132 {
133   for(int i = 0; i <n; i++)
134   {
135     for(int j = -2; j <= 2; j++)
136     {
137       symmetricElement(n,i,i+j);
138     }
139   }
140 }
141
142 void RadialAnalytics::symmetricElement(int n, int l1, int l2)
143 {
144   double value = 0.;
145   if (l1 == l2)
146   {
147     /* calculate the fully symmetric elements
148      * n1=n2 and l1=l2.
149      */
150     value = n*n/2. *(5*n*n + 1 - 3*l1*(l1+1));
151   }
152   else
153   {
154     /* Elements asymmetric in l. Calculation starts with
```

```
155         * the sum-term (back to front). In the sum, invalid
156         * faculty-operations or division by 0 can occur, these
157         * are sorted out.
158         */
159        double a = 0.;
160        double b = 0.;
161        for (int j = 0; j <= n-l2-1; j++)
162        {
163          a = pow(-1,j)*faculty(n+2-l1-j)*faculty(n+2+l1-j+1);
164          b =  faculty(j)*faculty(n-l2-1-j)*faculty(n+l2-j)*faculty(3-j) ;
165          if (b != 0.)
166            value += a/b;
167        }
168        value *= pow(-1,l1+l2)*pow(n/2.,2)/(2*n);
169        value *= sqrt( faculty(n-l2-1) * faculty(n+l2) / faculty(n-l1-1) / faculty(n+l1) );
170      }
171      if (l2 < n )
172      {
173        /* set elements */
174        setR2(n,n,l1,l2,value);
175        setR2(n,n,l2,l1,value);
176      }
177    }
178
179    /* dipole elements */
180    void RadialAnalytics::makeDipoleElements(int n1, int n2)
181    {
182      DipoleStart(n1,n2);
183      for (int l = n2-1; l>= 1; l--)
184      {
185        DipoleIteratorA(n1,n2,l);
186        DipoleIteratorB(n1,n2,l);
187      }
188    }
189
190    void RadialAnalytics::DipoleStart(int n1, int n2)
191    {
192      double value =  pow(-1,n1-n2-1) * pow(2,2*n2+2);
193      value *= sqrt( faculty(n1+n2) / (faculty(n1-n2-1) * faculty(2*n2-1)  ) );
194      value *= pow(n1*n2,n2+2);
195      value *= pow(n1-n2, n1-n2-2 ) / pow(n1+n2,n1+n2+2);
196      setR1(n1,n2,n2,n2-1,value);
197      setR1(n2,n1,n2-1,n2,value);
198    }
199
200    void RadialAnalytics::DipoleIteratorA(int n1, int n2, int l)
201    {
202      //start building up the term from the back
203      double value = A(n2,l+1)*getR1(n1,n2,l,l+1);
204      value += (2*l+1)*A(n1,l+1)*getR1(n1,n2,l+1,l);
205      value *= 1./(2*l*A(n2,l));
206      setR1(n1,n2,l,l-1,value);
```

```
207     setR1(n2,n1,l-1,l,value);
208   }
209
210   void RadialAnalytics::DipoleIteratorB(int n1, int n2, int l)
211   {
212     //start building up the term from the back
213     double value = A(n1,l+1)*getR1(n1,n2,l+1,l);
214     value += (2*l+1)*A(n2,l+1)*getR1(n1,n2,l,l+1);
215     value *= 1./(2*l*A(n1,l));
216     setR1(n1,n2,l-1,l,value);
217     setR1(n2,n1,l,l-1,value);
218   }
219
220   /* Quadrupole Elements */
221   void RadialAnalytics::makeQuadrupoleElements(int n1, int n2)
222   {
223     QuadrupoleL0Start(n1,n2);
224     for (int l = n2; l>= 1; l--)
225       {
226         QuadrupoleL0IteratorA(n1,n2,l);
227       }
228     QuadrupoleL2Start(n1,n2);
229     for (int l = n2-1; l>=2; l--)
230     {
231       QuadrupoleL2IteratorA(n1,n2,l);
232       QuadrupoleL2IteratorB(n1,n2,l-1);
233     }
234     QuadrupoleL2IteratorA(n1,n2,1);
235     /*
236      * correct for sign-issues. Not sure where they come from
237      * but this gets rid of them
238      */
239     double buffer;
240     for(int l1 = 0; l1 <n1; l1++)
241       for (int l2 = 0; l2 < n2; l2++)
242       {
243         buffer = getR2(n1,n2,l1,l2);
244         buffer *= pow(-1,n1-n2);
245         setR2(n1,n2,l1,l2,buffer);
246         buffer = getR2(n2,n1,l2,l1);
247         buffer *= pow(-1,n2-n1);
248         setR2(n2,n1,l2,l1,buffer);
249       }
250   }
251
252   void RadialAnalytics::QuadrupoleL0Start(int n1, int n2)
253   {
254     double value = 2*n1*n2/sqrt(n1*n1-n2*n2);
255     value *= getR1(n1,n2,n2,n2-1); //dipole-start
256     setR2(n1,n2,n2-1,n2-1,value);
257     setR2(n2,n1,n2-1,n2-1,value);
258   }
```

```
259
260 void RadialAnalytics::QuadrupoleL0IteratorA(int n1, int n2, int l)
261 {
262   double value =  2*getR1(n1,n2,l,l-1);
263   value += sqrt(n2*n2-l*l)/(n2*l*1.)*getR2(n1,n2,l,l);
264   value*=n1*l/sqrt(n1*n1-l*l);
265   setR2(n1,n2,l-1,l-1,value);
266   setR2(n2,n1,l-1,l-1,value);
267 }
268
269 void RadialAnalytics::QuadrupoleL2Start(int n1, int n2)
270 {
271   if (fabs(n1-n2)>= 2)
272   {
273     double value =  pow(-1,n1-n2) ;
274     value *= pow(2,2*n2+4);
275     value *= sqrt( faculty(n1+n2+1) / faculty(n1-n2-2) / faculty(2*n2-1) );
276     value *= n2*pow(n1*n2,n2+3);
277     value *= pow(n1-n2,n1-n2-3)/pow(n1+n2,n1+n2+3);
278     setR2(n1,n2,n2+1,n2-1,value);
279     setR2(n2,n1,n2-1,n2+1,value);
280   }
281 }
282
283 void RadialAnalytics::QuadrupoleL2IteratorA(int n1, int n2, int l)
284 {
285   double value = 2*(2*l+1)*(3*l+5)*getR1(n1,n2,l+1,l);
286   value += 2*(l+1)*A(n2,l+1)*getR2(n1,n2,l+1,l+1);
287   value += (2*l+1)*(l+2)*A(n1,l+2)*getR2(n1,n2,l+2,l);
288   value *= 1./( l*(2*l+3)*A(n2,l) );
289   setR2(n1,n2,l+1,l-1,value);
290   setR2(n2,n1,l-1,l+1,value);
291 }
292
293 void RadialAnalytics::QuadrupoleL2IteratorB(int n1, int n2, int l)
294 {
295   double value = 2*(2*l+1)*(3*l+5)*getR1(n1,n2,l,l+1);
296   value += 2*(l+1)*A(n1,l+1)*getR2(n1,n2,l+1,l+1);
297   value += (2*l+1)*(l+2)*A(n2,l+2)*getR2(n1,n2,l,l+2);
298   value *= 1./( l*(2*l+3)*A(n1,l) );
299   setR2(n1,n2,l-1,l+1,value);
300   setR2(n2,n1,l+1,l-1,value);
301 }
```

B.2 Semi-Classical Method

The following Mathematica code allows calculation of Rydberg energy levels by the semi-classical method described in section 5.1.4. The program gives all energy levels between two n-states for a given value of the magnetic field B_0. The results are displayed as a table listing the energy shifts in wavenumbers and Hz.

Basic Input

Quantum Defects

In[1]:=
```
μ[n_, A_, B_, C_, D_, E_] := A + B / (n - A)^2 + C / (n - A)^4 + D / (n - A)^6 + E / (n - A)^8;
Ad = 2.46631524;
Bd = 0.013577;
Cd = -0.37457;
Dd = -2.1867;
Ed = -1.5532;
```

Constants

In[7]:=
```
cAU = 137.0359991; (* speed of light in a.u.*)
cSI = 299792458;  (* speed of light is SI units *)
GaussToAu = 1 / (1.7152553 10^7); (* conversion for mag. field in a.u.*)
Hartree = 219474.63068;
Eion = 31406.46769; (*Ionization energy of cesium [1/cm] *)
vIon = Eion 10^2 cSI;
v6S = 17.2733 10^9; (*6S energy shift *)
```

Effective Potential

In[12]:=
$$V[r\_, ml\_, En\_, H\_] := \sqrt{2\,En - \frac{(ml + 1/2)^2}{r^2} + \frac{2}{r} - \frac{H\,ml}{cAU} - \left(\frac{H\,r}{2\,cAU}\right)^2}$$

Parameters

In[16]:=
```
Bo = 1.011 10^4 GaussToAu; (* magnetic field *)
ml = 2; (* quantum number m *)
v1 = 351.7368 10^12;  (* frequency of the first laser *)
```

Calculations

Classical Turning Radii

```
NSolve[V[r, ml, Bo ml / (2 cAU), Bo] == 0, r];
ρ1 = r /. %[[4]][[1]];
ρ2 = r /. %%[[3]][[1]];

nStart = 20;
nEnd = 30;
EnergyLevels = Table[{n,
    (En /. FindRoot[Re[NIntegrate[V[r, ml, En, Bo], {r, ρ1, ρ2}]] ==
          (n - μ[n, Ad, Bd, Cd, Dd, Ed] + 1 / 2 - 3) π, {En, Bo ml / (2 cAU)}]][[
        1]]) Hartree, 0, 0, 0}, {n, nStart, nEnd}];
For[k = 1, k < Length[[EnergyLevels]], k++,
 EnergyLevels[[k, 3]] = EnergyLevels[[k, 2]] 10^2 * cSI
]
For[k = 1, k ≤ nEnd - nStart + 1, k++,
 {
  EnergyLevels[[k, 3]] = Eion + EnergyLevels[[k, 2]] ;
  EnergyLevels[[k, 4]] = EnergyLevels[[k, 2]] 10^2 * cSI;
  EnergyLevels[[k, 5]] = νIon - ν1 - ν6S + EnergyLevels[[k, 2]] 10^2 * cSI ;
 }
]
TableForm[EnergyLevels , TableHeadings →
  {None, {"n", "Δ ν̄ [cm^-1]", "ν̄ [cm^-1]", "energy level [Hz]", "green frequency [Hz]"}}]
```

Bibliography

[1] *Gnu Scientific Library (GSL),* `http://www.gnu.org/software/gsl/` (2012)

[2] *Particle Data Group,* `http://pdg.lbl.gov` (2012)

[3] C. Amole et al. *Nature*, **483**:439 (2012)

[4] M. Amoretti et al. *Nature*, **419**:456 (2002)

[5] M. Amoretti et al. *Physics Letters B*, **583**:59 (2004)

[6] M. Amoretti et al. *Phys. Rev. Lett.*, **97**:213401 (2006)

[7] C. Amsler. *Rev. Mod. Phys.*, **70**:1293 (1998)

[8] C. D. Anderson. *Science*, **76**:238 (1932)

[9] C. D. Anderson. *Phys. Rev.*, **43**:491 (1933)

[10] G. B. Andresen et al. *Nature*, **468**:673 (2010)

[11] G. B. Andresen et al. *Phys. Rev. Lett.*, **106**:025002 (2011)

[12] E. Arimondo, M. Inguscio and P. Violino. *Rev. Mod. Phys.*, **49**:31 (1977)

[13] G. Baur et al. *Physics Letters B*, **368**:251 (1996)

[14] T. Bergeman, G. Erez and H. J. Metcalf. *Phys. Rev. A*, **35**:1535 (1987)

[15] G. Blanford, D. C. Christian, K. Gollwitzer, M. Mandelkern, C. T. Munger, J. Schultz and G. Zioulas. *Phys. Rev. Lett.*, **80**:3037 (1998)

[16] R. Bluhm. In *Special Relativity*, vol. 702 of *Lecture Notes in Physics* (edited by J. Ehlers and C. Lämmerzahl), 191–226. Springer Berlin / Heidelberg (2006)

[17] R. Bluhm, V. A. Kostelecký and N. Russell. *Phys. Rev. Lett.*, **82**:2254 (1999)

[18] S. Böttner. *Optimierung von kompakten Resonatoren zur Frequenzverdopplung*. Diplomarbeit, Johannes Gutenberg Universität Mainz (2010)

[19] R. W. Boyd. *Nonlinear Optics*. Academic Press, 3rd ed. (2008)

[20] L. S. Brown and G. Gabrielse. *Rev. Mod. Phys.*, **58**:233 (1986)

[21] G. I. Budker. *Atomic Energy*, **22**:438 (1967)

[22] R. Carosi et al. *Physics Letters B*, **237**:303 (1990)

[23] J. C. Castro, M. L. Zimmerman, R. G. Hulet, D. Kleppner and R. R. Freeman. *Phys. Rev. Lett.*, **45**:1780 (1980)

[24] C. L. Cesar, D. G. Fried, T. C. Killian, A. D. Polcyn, J. C. Sandberg, I. A. Yu, T. J. Greytak, D. Kleppner and J. M. Doyle. *Phys. Rev. Lett.*, **77**:255 (1996)

[25] O. Chamberlain, E. Segrè, C. Wiegand and T. Ypsilantis. *Phys. Rev.*, **100**:947 (1955)

[26] E. S. Chang. *Phys. Rev. A*, **31**:495 (1985)

[27] G. Chardin et al. *Proposal to measure the Gravitational Behaviour of Antihydrogen at Rest*. Tech. Rep. CERN-SPSC-2011-029. SPSC-P-342, CERN, Geneva (2011)

[28] M. Charlton. *Physics Letters A*, **143**:143 (1990)

[29] M. Charlton, J. Eades, D. Horvath, R. J. Hughes and C. Zimmermann. *Physics Reports* (1994)

[30] J. H. Christenson, J. W. Cronin, V. L. Fitch and R. Turlay. *Phys. Rev. Lett.*, **13**:138 (1964)

[31] S. Cialdi, I. Boscolo, F. Castelli, F. Villa, G. Ferrari and M. Giammarchi. *Nuclear Instruments and Methods in Physics Research B*, **269**:1527 (2011)

[32] D. Colladay and V. A. Kostelecký. *Phys. Rev. D*, **55**:6760 (1997)

[33] D. Comeau, A. Dror, D. W. Fitzakerley, M. C. George, E. A. Hessels, C. H. Storry, M. Weel, D. Grzonka, W. Oelert, G. Gabrielse, R. Kalra, W. S. Kolthammer, R. McConnell, P. Richerme, A. Müllers and J. Walz. *New Journal of Physics*, **14**:045006 (2012)

[34] B. Cork, G. R. Lambertson, O. Piccioni and W. A. Wenzel. *Phys. Rev.*, **104**:1193 (1956)

[35] J. R. Danielson and C. M. Surko. *Phys. Rev. Lett.*, **94**:035001 (2005)

[36] J. R. Danielson and C. M. Surko. *Physics of Plasmas*, **13**:055706 (2006)

[37] R. C. Davidson. *Physics of Nonneutral Plasmas*. World Scientific Pub. Co., 2nd ed. (2001)

[38] W. Demtröder. *Laserspektroskopie*. Springer (2007)

[39] B. I. Deutch, A. S. Jensen, A. Miranda and G. C. Oades. *Proceedings of The First Workshop on Antimatter Physics at Low Energy*, 371 (1986)

[40] P. A. M. Dirac. *Proceedings of the Royal Society A*, **117**:610 (1928)

[41] P. A. M. Dirac. *Mathematical Proceedings of the Cambridge Philosophical Society*, **26**:361 (1930)

[42] P. A. M. Dirac. *Proceedings of the Royal Society A*, **126**:360 (1930)

[43] P. A. M. Dirac. *Proceedings of the Royal Society A*, **133**:60 (1931)

[44] R. D. Dixon and L. A. Lott. *Journal of Applied Physics*, **40**:4938 (1969)

[45] P. H. Donnan and F. Robicheaux. *New Journal of Physics*, **14**:035018 (2012)

[46] M. Doser. *Journal of Physics: Conference Series*, **199**:012009 (2010)

[47] G. Drake (editor). *Springer Handbook of Atomic, Molecular, and Optical Physics*. No. 1 in Springer Handbooks. Springer (2005)

[48] G. Y. Drobychev et al. *Proposal for the AEGIS Experiment at the CERN Antiproton Decelerator*. Tech. Rep. SPSC-P-334. CERN-SPSC-2007-017, CERN, Geneva (2007)

[49] D. H. E. Dubin. *Phys. Rev. Lett.*, **66**:2076 (1991)

[50] D. H. E. Dubin and T. M. O'Neil. *Rev. Mod. Phys.*, **71**:87 (1999)

[51] R. C. Duncan and C. Thompson. *The Atsrophysical Journal*, **392**:L9 (1992)

[52] N. P. Economou, R. R. Freeman and P. F. Liao. *Phys. Rev. A*, **18**:2506 (1978)

[53] A. R. Edmonds. *J. Phys. Colloques*, **31**:C4 (1970)

[54] M. Enciso-Aguilar, J. López-Bonilla and M. Sánchez-Meraz. *Electronic Journal of Theoretical Physics*, **3**:117 (2006)

[55] Z.-G. Feng, L.-J. Zhang, J.-M. Zhao, C.-Y. Li and S.-T. Jia. *Journal of Physics B*, **42**:145303 (2009)

[56] D. W. Fitzakerley, M. C. George, E. A. Hessels, C. H. Storry, M. Weel, D. Grzonka, W. Oelert, S. Ettenauer, G. Gabrielse, R. Kalra, E. Tardiff, A. Müllers and J. Walz (2012). Electron cooling and accumulation of 4×10^9 positrons in a system capable of longterm storage of antihydrogen atoms; *submitted to PRL*

[57] S. Friedreich, D. Barna, F. Caspers, A. Dax, R. Hayano, M. Hori, D. Horváth, B. Juhász, T. Kobayashi, O. Massiczek, A. Sótér, K. Todoroki, E. Widmann and J. Zmeskal. *Physics Letters B*, **700**:1 (2011)

[58] G. Gabrielse. *Phys. Rev. A*, **27**:2277 (1983)

[59] G. Gabrielse, N. S. Bowden, P. Oxley, A. Speck, C. H. Storry, J. N. Tan, M. Wessels, D. Grzonka, W. Oelert, G. Schepers, T. Sefzick, J. Walz, H. Pittner, T. W. Hänsch and E. A. Hessels. *Phys. Rev. Lett.*, **89**:213401 (2002)

[60] G. Gabrielse, X. Fei, K. Helmerson, S. L. Rolston, R. Tjoelker, T. A. Trainor, H. Kalinowsky, J. Haas and W. Kells. *Phys. Rev. Lett.*, **57**:2504 (1986)

[61] G. Gabrielse, X. Fei, L. A. Orozco, R. L. Tjoelker, J. Haas, H. Kalinowsky, T. A. Trainor and W. Kells. *Phys. Rev. Lett.*, **63**:1360 (1989)

[62] G. Gabrielse, R. Kalra, W. S. Kolthammer, R. McConnell, P. Richerme, D. Grzonka, W. Oelert, T. Sefzick, M. Zielinski, D. W. Fitzakerley, M. C. George, E. A. Hessels, C. H. Storry, M. Weel, A. Müllers and J. Walz. *Phys. Rev. Lett.*, **108**:113002 (2012)

[63] G. Gabrielse, A. Khabbaz, D. S. Hall, C. Heimann, H. Kalinowsky and W. Jhe. *Phys. Rev. Lett.*, **82**:3198 (1999)

[64] G. Gabrielse, W. S. Kolthammer, R. McConnell, P. Richerme, R. Kalra, E. Novitski, D. Grzonka, W. Oelert, T. Sefzick, M. Zielinski, D. W. Fitzakerley, M. C. George, E. A. Hessels, C. H. Storry, M. Weel, A. Müllers and J. Walz. *Phys. Rev. Lett.*, **106**:073002 (2011)

[65] G. Gabrielse, W. S. Kolthammer, R. McConnell, P. Richerme, J. Wrubel, R. Kalra, E. Novitski, D. Grzonka, W. Oelert, T. Sefzick, M. Zielinski, J. S. Borbely, D. Fitzakerley, M. C. George, E. A. Hessels, C. H. Storry, M. Weel, A. Müllers, J. Walz and A. Speck. *Phys. Rev. Lett.*, **105**:213002 (2010)

[66] G. Gabrielse, P. Larochelle, D. Le Sage, B. Levitt, W. S. Kolthammer, R. McConnell, P. Richerme, J. Wrubel, A. Speck, M. C. George, D. Grzonka, W. Oelert, T. Sefzick, Z. Zhang, A. Carew, D. Comeau, E. A. Hessels, C. H. Storry, M. Weel and J. Walz. *Phys. Rev. Lett.*, **100**:113001 (2008)

[67] G. Gabrielse and F. Mackintosh. *International Journal of Mass Spectrometry and Ion Processes*, **57**:1 (1984)

[68] G. Gabrielse, S. Rolston, L. Haarsma and W. Kells. *Physics Letters A*, **129**:38 (1988)

[69] T. F. Gallagher. *Rydberg Atoms*. Cambridge University Press (1994)

[70] R. L. Garwin, L. M. Lederman and M. Weinrich. *Phys. Rev.*, **105**:1415 (1957)

[71] J. C. Gay, D. Delande and F. Biraben. *Journal of Physics B: Atomic and Molecular Physics*, **13**:L729 (1980)

[72] M. Gell-Mann. *Phys. Rev.*, **125**:1067 (1962)

[73] V. Gerginov, A. Derevianko and C. E. Tanner. *Phys. Rev. Lett.*, **91**:072501 (2003)

[74] V. Gerginov, C. E. Tanner, S. A. Diddams, A. Bartels and L. Hollberg. *Opt. Lett.*, **30**:1734 (2005)

[75] D. W. Gidley, H.-G. Peng and R. S. Vallery. *Annual Review of Materials Research*, **36**:49 (2006)

[76] M. E. Glinsky and T. M. O'Neil. *Physics of Fluids B: Plasma Physics*, **3**:1279 (1991)

[77] O. W. Greenberg. *Phys. Rev. Lett.*, **89**:231602 (2002)

[78] D. Hanneke, S. Fogwell and G. Gabrielse. *Phys. Rev. Lett.*, **100**:120801 (2008)

[79] T. Hänsch and C. Zimmermann. *Hyperfine Interactions*, **76**:47 (1993)

[80] T. W. Hänsch and B. Couillaud. *Optics Communications*, **35**:441 (1980)

[81] M. Herrmann. *Untersuchung zur Produktion von Antiwasserstoff mittels zweifachem Ladungstransfer*. Diplomarbeit, TU München (2003)

[82] E. A. Hessels, D. M. Homan and M. J. Cavagnero. *Phys. Rev. A*, **57**:1668 (1998)

[83] J. D. Hey. *Journal of Physics B*, **39**:2641 (2006)

[84] M. H. Holzscheiter and M. Charlton. *Reports on Progress in Physics*, **62**:1 (1999)

[85] M. Hori, A. Soter, D. Barna, A. Dax, R. Hayano, S. Friedreich, B. Juhasz, T. Pask, E. Widmann, D. Horvath, L. Venturelli and N. Zurlo. *Nature*, **475**:484 (2011)

[86] X.-P. Huang, F. Anderegg, E. M. Hollmann, C. F. Driscoll and T. M. O'Neil. *Phys. Rev. Lett.*, **78**:875 (1997)

[87] M. Y. Ivanov and A. Stolow. *Chemical Physics Letters*, **265**:231 (1997)

[88] J. N. Kavanagh, F. J. Currell, D. J. Timson, M. H. Holzscheiter, N. Bassler, R. Herrmann, K. M. Prise and G. Schettino. *European Physical Journal D*, **60**:209 (2010)

[89] D. Kolbe, A. Beczkowiak, T. Diehl, A. Koglbauer, M. Sattler, M. Stappel, R. Steinborn and J. Walz. *Hyperfine Interactions*, 1 (2011)

[90] W. S. Kolthammer. *Antimatter Plasmas Within a Penning-Ioffe Trap*. PhD thesis, Harvard University (2011)

[91] C. Kouveliotou, S. Dieters, T. Strohmayer, J. van Paradijs, G. J. Fishman, C. A. Meegan, K. Hurley, J. Kommers, I. Smith, D. Frail and T. Murakami. *Nature*, **393**:235 (1998)

[92] J. Lahiri and S. T. Manson. *Phys. Rev. A*, **33**:3151 (1986)

[93] P. Larochelle. *Machines and Methods for Trapping Antihydrogen*. PhD thesis, Harvard University (2009)

[94] T. D. Lee and C. N. Yang. *Phys. Rev.*, **104**:254 (1956)

[95] B. Levitt, G. Gabrielse, P. Larochelle, D. L. Sage, W. Kolthammer, R. McConnell, J. Wrubel, A. Speck, D. Grzonka, W. Oelert, T. Sefzick, Z. Zhang, D. Comeau, M. George, E. Hessels, C. Storry, M. Weel and J. Walz. *Physics Letters B*, **656**:25 (2007)

[96] Z. Lin-Jie, F. Zhi-Gang, L. An-Ling, Z. Jian-Ming, L. Chang-Yong and J. Suo-Tang. *Chinese Physics B*, **18**:1838 (2009)

[97] G. Lüders. *Annals of Physics*, **2**:1 (1957)

[98] F. Major, V. Gheorghe and G. Werth. *Charged Particle Traps: Physics and Techniques of Charged Particle Field Confinement*. Springer Series on Atomic, Optical, and Plasma Physics. Springer (2005)

[99] S. Mariazzi, P. Bettotti, S. Larcheri, L. Toniutti and R. S. Brusa. *Phys. Rev. B*, **81**:235418 (2010)

[100] R. McConnell. *Laser-Controlled Charge-Exchange Production of Antihydrogen*. PhD thesis, Harvard University (2011)

[101] J. Mehra and H. Rechenberg. *The historical development of Quantum Theory*, vol. 6. Springer (2001)

[102] J. P. Merrison, H. Bluhme, J. Chevallier, B. I. Deutch, P. Hvelplund, L. V. Jørgensen, H. Knudsen, M. R. Poulsen and M. Charlton. *Phys. Rev. Lett.*, **78**:2728 (1997)

[103] D. Möhl, G. Petrucci, L. Thorndahl and S. van der Meer. *Physics Reports*, **58**:73 (1980)

[104] P. J. Mohr, B. N. Taylor and D. B. Newell. *ArXiv e-prints* (2012). CODATA Recommended Values of the Fundamental Physical Constants: 2010

[105] A. Müllers. *A Solid State Laser System for Production of Antihydrogen via Double Charge Exchange*. Diplomarbeit, Johannes Gutenberg Universität Mainz (2008)

[106] A. Müllers, S. Böttner, D. Kolbe, T. Diehl, A. Koglbauer, M. Sattler, M. Stappel, R. Steinborn, J. Walz, G. Gabrielse, R. Kalra, W. S. Kolthammer, R. P. McConnell, P. Richerme, D. W. Fitzakerley, M. C. George, E. A. Hessels, C. H. Storry, M. Weel, D. Grzonka and W. Oelert. *New Journal of Physics*, **14**:055009 (2012)

[107] T. J. Murphy and C. M. Surko. *Phys. Rev. A*, **46**:5696 (1992)

[108] W. Oelert, G. Gabrielse, R. Hayano, M. Holzscheiter, J. Hangst and P. Lichard. *ELENA: An Upgrade to the Antiproton Decelerator*. Tech. Rep. CERN-SPSC-2009-026. SPSC-P-338, CERN, Geneva (2009)

[109] J. R. Oppenheimer. *Phys. Rev.*, **35**:562 (1930)

[110] M. Pajek and R. Schuch. *Hyperfine Interactions*, **108**:185 (1997)

[111] C. G. Parthey, A. Matveev, J. Alnis, B. Bernhardt, A. Beyer, R. Holzwarth, A. Maistrou, R. Pohl, K. Predehl, T. Udem, T. Wilken, N. Kolachevsky, M. Abgrall, D. Rovera, C. Salomon, P. Laurent and T. W. Hänsch. *Phys. Rev. Lett.*, **107**:203001 (2011)

[112] P. Pérez, L. Liszkay, J.-M. Rey, V. Blideanu, M. Carty, A. Curtoni, O. Delferrierre, P. Dupré, T. Muranaka, N. Ruiz and Y. Sacquin. *Physica Status Solidi C*, **6**:2462 (2009)

[113] H. Pittner. *The Production and Investigation of Cold Antihydrogen Atoms*. PhD thesis, Ludwig-Maximilians-Universität München (2005)

[114] R. J. Rafac and C. E. Tanner. *Phys. Rev. A*, **56**:1027 (1997)

[115] L. Ricci, M. Weidemüller, T. Esslinger, A. Hemmerich, C. Zimmermann, V. Vuletic, W. König and T. Hänsch. *Optics Communications*, **117**:541 (1995)

[116] P. Richerme. *Trapped Antihydrogen in its Ground State*. PhD thesis, Harvard University (2012)

[117] S. Rolston and G. Gabrielse. *Hyperfine Interactions*, **44**:233 (1989)

[118] O. Schmidt, K. Knaak, R. Wynands and D. Meschede. *Applied Physics B*, **59**:167 (1994)

[119] S. Sellner, C. P. Welsch and M. Holzscheiter. *Radiation Measurements*, **46**:1770 (2011)

[120] A. Siegman, M. Sasnett and T. Johnston Jr. *IEEE Journal of Quantum Electronics*, **27**:1098 (1991)

[121] A. Speck. *Two Techniques to Produce Cold Antihydrogen*. PhD thesis, Harvard University (2005)

[122] A. Speck, C. Storry, E. Hessels and G. Gabrielse. *Physics Letters B*, **597**:257 (2004)

[123] A. F. Starace. *Journal of Physics B: Atomic and Molecular Physics*, **6**:585 (1973)

[124] D. A. Steck. *http://steck.us/alkalidata/* (2010)

[125] J. Stevefelt, J. Boulmer and J. F. Delpech. *Phys. Rev. A*, **12**:1246 (1975)

[126] C. H. Storry, A. Speck, D. L. Sage, N. Guise, G. Gabrielse, D. Grzonka, W. Oelert, G. Schepers, T. Sefzick, H. Pittner, M. Herrmann, J. Walz, T. W. Hänsch, D. Comeau and E. A. Hessels. *Phys. Rev. Lett.*, **93**:263401 (2004)

[127] S. Sturm, A. Wagner, B. Schabinger, J. Zatorski, Z. Harman, W. Quint, G. Werth, C. H. Keitel and K. Blaum. *Phys. Rev. Lett.*, **107**:023002 (2011)

[128] M. D. Tinkle, R. G. Greaves, C. M. Surko, R. L. Spencer and G. W. Mason. *Phys. Rev. Lett.*, **72**:352 (1994)

[129] T. Udem, J. Reichert, T. Hänsch and M. Kourogi. *Physical Review A*, **62** (2000)

[130] T. Udem, J. Reichert, R. Holzwarth and T. W. Hänsch. *Physical Review Letters*, **82**:3568 (1999)

[131] R. S. Van Dyck, P. B. Schwinberg and H. G. Dehmelt. *Phys. Rev. Lett.*, **59**:26 (1987)

[132] M. L. Wall, C. S. Norton and F. Robicheaux. *Phys. Rev. A*, **72**:052702 (2005)

[133] J. N. Walpole. *Optical and Quantum Electronics*, **28**:623 (1996)

[134] K.-H. Weber and C. J. Sansonetti. *Phys. Rev. A*, **35**:4650 (1987)

[135] E. Widmann, J. Eades, R. Hayano, T. Ishikawa, W. Pirkl, M. Hori, Y. Yamazaki, A. Mohri, T. Yamazaki, D. Horváth, B. Juhász and E. Takács. *Measurement of the Antihydrogen Hyperfine Structure*. Tech. Rep. CERN-SPSC 2005-002 P307, ASACUSA Collaboration (2003)

[136] J. Wrubel, G. Gabrielse, W. Kolthammer, P. Larochelle, R. McConnell, P. Richerme, D. Grzonka, W. Oelert, T. Sefzick, M. Zielinski, J. Borbely, M. George, E. Hessels, C. Storry, M. Weel, A. Müllers, J. Walz and A. Speck. *Nuclear Instruments and Methods in Physics Research A*, **640**:232 (2011)

[137] C. S. Wu, E. Ambler, R. W. Hayward, D. D. Hoppes and R. P. Hudson. *Phys. Rev.*, **105**:1413 (1957)

[138] C. Ye. *Tunable External Cavity Diode Lasers*. World Scientific (2004)

[139] E. Zanger, R. Mueller, B. Liu and W. Gries. In *SPIE conference proceedings*, vol. 3862 (edited by F. Gan, H. Weber, Z. Li and Q. Chen), 255–261. SPIE (1999)

[140] M. L. Zimmerman, J. C. Castro and D. Kleppner. *Phys. Rev. Lett.*, **40**:1083 (1978)

Assertion

I hereby declare that I wrote the dissertation submitted without any unauthorized external assistance and used only sources acknowledged in the work. All textual passages which are appropriated verbatim or paraphrased from published and unpublished texts as well as all information obtained from oral sources are duly indicated and listed in accordance with bibliographical rules. In carrying out this research, I complied with the rules of standard scientific practice as formulated in the statutes of Johannes Gutenberg-University Mainz to insure standard scientific practice.

Mainz, October 28, 2012

_____

Andreas Müllers